Agenzia Nazionale per le Nuove Tecnologie,
l'Energia e lo Sviluppo Economico Sostenibile

Ministero dello Sviluppo Economico

RICERCA DI SISTEMA ELETTRICO

Implementazione strumentazione sezione di prova per qualifica dello scambiatore prototipico DHR per sistemi LFR

M. Tarantino

Report RdS/2011/45

IMPLEMENTAZIONE STRUMENTAZIONE SEZIONE DI PROVA PER QUALIFICA DELLO SCAMBIATORE PROTOTIPICO DHR PER SISTEMI LFR

M. Tarantino (ENEA)

Settembre 2011

Report Ricerca di Sistema Elettrico
Accordo di Programma Ministero dello Sviluppo Economico – ENEA
Area: Governo, Gestione e sviluppo del sistema elettrico nazionale
Progetto: Nuovo nucleare da fissione: collaborazioni internazionali e sviluppo competenze in materia nucleare

Responsabile Progetto: Paride Meloni, ENEA

ENEA Ricerca Sistema Elettrico	Sigla di identificazione	Distrib.	Pag.	di
	NNFISS – LP3 - 026	L	1	114

Titolo

Implementazione strumentazione sezione di prova per qualifica dello scambiatore prototipico DHR per sistemi LFR

Descrittori

Tipologia del documento: Rapporto Tecnico

Collocazione contrattuale: Accordo di programma ENEA-MSE: tema di ricerca "Nuovo nucleare da fissione"

Argomenti trattati: Tecnologia dei metalli liquidi
Termo-fluidodinamica
Reattori nucleari veloci
Generation IV reactors

Sommario

The present document reports the design of the CIRCE experiment to be performed with the goal to weel-chracterize the thermal-hydraulic behavioour of a prototipival DHR-HX installed on the CIRCE facilty.

The experiment is moreover devoted to the assessment of the mixed convection and stratification phenomena in a heavy liquid metal pool during the transition from the forced (nominal) flow conditions to the natural circulation.

The experiment has to be implemented on the CIRCE facility, by an appropriate upgrade of the ICE test section.

Note

Copia n. **In carico a:**

REV.	DESCRIZIONE	DATA		REDAZIONE	CONVALIDA	APPROVAZIONE
2			NOME			
			FIRMA			
1			NOME			
			FIRMA			
0	EMISSIONE		NOME	M. Tarantino	P. Agostini	P. Meloni
			FIRMA			

INDEX

1. SCOPE OF THE EXPERIMENT

The objective of CIRCE experiment is to characterize the phenomena of mixed convection and stratification in a heavy liquid metal pool in the safety relevant situation, that is during the transition from nominal flow conditions to the natural circulation typical of Decay Heat Removal (DHR) conditions.

To achieve this goal the CIRCE large scale facility already representative of a HLM pool-type reactor will be fitted with a DHR system and a suitable instrumentations.

Indeed, in order to provide experimental data for the validation of CFD models, the on-set and stabilization of the DHR flow path, uncoupled from the primary flow path, will be monitored by means of a proper instrumentation, as well as a detailed measurement of temperatures in the pool, that will allow to monitor the manifestation of the thermal stratification.

The defined experiment will be performed on the CIRCE large scale facility [1] by the ENEA Brasimone Research Centre, where an appropriate test section already exist.

The test section available refers to the “Integral Circulation Experiment”, ICE, and it was designed, built up and operated in the frame of the past expriemntal campaign.

Later on, the CIRCE facility, as well as the ICE test section and the upgrade proposed to achieve the goal above mentioned are described.

2. GENERAL DESCRIPTION OF THE EXPERIMENTAL TEST SECTION

2.1 CIRCE FACILITY

CIRCE basically consists of a cylindrical vessel (Main Vessel S100) filled with about 70 tons of molten Lead-Bismuth Eutectic (LBE) with argon cover gas and recirculation system, LBE heating and cooling systems, several test sections welded to and hung from bolted vessel heads for separate-effect and integral testing, and auxiliary equipment for eutectic circulation [2],[3].

The facility is complete of a LBE storage tank (S200), of a small LBE transfer tank (S300) and of the data acquisition system.

In figure 1, an isometric view of the facility is shown. The facility can be considered made up of two parts, the first being dedicated to the LBE containment and management, and the other consisting of the auxiliary systems.

Concerning the first part, the main components are the above mentioned vessels: the test vessel S100, the storage tank S200 and the intermediate vessel S300, this later one being used during the handling of the LBE between the two other vessels.

During the loading operations, the LBE is gradually transferred from the storage tank to the S300 vessel. Then, by pressurization of the S300 cover gas, the liquid metal is moved to the test vessel. In this way, step by step, the test vessel is gradually filled from the bottom.

The main vessel S100 consists of a vertical vessel 8500 mm height, connected by gates to the other systems, from both the LBE and gas sides. It is equipped with electrical heating cables, installed on its bottom and lateral surface. This heating system allows to operate in a temperature range of 200 ÷ 400°C.

The main vessel is also equipped by a skimming line and a passive pressure safety system, in order to guarantee the LBE top level and to prevent accidental overpressures. The main parameters relevant to the test vessel are listed in table 1 .

S100 is designed to house the ICE test section necessary to perform the tests on the plant, as in the following.

Parameters	Value
Outside Diameter	1200 mm
Wall Thickness	15 mm
Material	AISI 316L
Max LBE Inventory	90000 kg
Electrical Heating	47 kW
Cooling Air Flow Rate	3 Nm^3/s
Temperature Range	200 to 550 °C
Operating Pressure	15 kPa (gauge)
Design Pressure	450 kPa (gauge)
Argon Flow Rate	15 Nl/s
Argon Injection Pressure	600 kPa (gauge)

Table.1 – Circe main vessel parameters

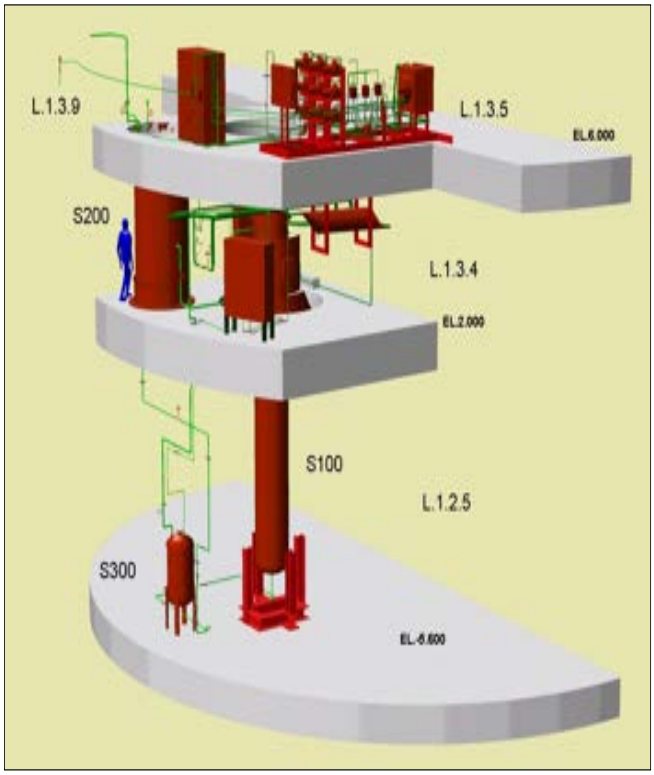

Figure 1 . CIRCE isometric view.

2.2 ICE Test Section

The ICE test section has been designed to reproduce, as practicable as possible, the thermal-hydraulic behaviour of the XT-ADS and EFIT primary system [4-8] .

The main experimental parameters which characterize the ICE activity are reported in table 2.

	XT-ADS	**EFIT**	**ICE**
Coolant	LBE	Pure Lead	LBE
Primary Loop Circulation	Mechanical Pump	Mechanical Pump	Gas Lift Technique
Fuel Assembly Lattice	Hexagonal	Hexagonal	Hexagonal
Fuel Assembly Type	Wrapper	Wrapper	Wrapper
Fuel Assembly Spacer	Grid	Grid	Grid
Fuel Pin Diameter (D) [mm]	6.55	8.72	8.2
Pitch to Diameter Ratio (P/D)	1.41	1.56	1.8
Fuel Heat Flux q'' [W/cm^2]	85-115	100-140	100
Fuel Power Density q''' [W/cm^3]	500-700	450-650	488
Average Velocity Fuel Pin Region [m/s]	1	1	1
Fuel Pin Active Length [mm]	600	900	1000
T_{in}/T_{out} core [°C] *	300/400	400/480	300/400
T_{HS}/L_{act} [°C/m]	167	88	100
Fuel Pin Cladding Material	T91	T91	AISI 316L
Secondary Coolant	Low Pressure Boiling Water	Water with superheated steam	Pressurized Water

*This value refers to the thermal difference between the inlet and outlet section of the ICE Heat Section (made by a single bundle); for EFIT and XT-ADS it refers to the thermal difference between the upper and lower plenum of the core.

Table 2 . Overview of the experimental parameters adopted for the ICE activity, compared with the foreseen XT-ADS and EFIT concepts ones.

As can be noted, the main ICE experimental parameters are in good agreement with the parameters foreseen for the XT-ADS and EFIT concepts (q''', $\bar{w}_{HS}$, $\Delta T_{HS} / L_{act}$).

The main difference between ICE and the XT-ADS/EFIT concepts is the P/D ratio value.

For the ICE test section a P/D ratio value of 1.8 has been adopted to reduce the overall pressure drop along the primary flow path, preserving the main characteristics

of the heat source and allowing to perform the tests by means of the available pumping system (gas-lift technique).

The ICE test section, to be placed in the CIRCE main vessel (S100), consists of the following main components, as depicted in figures 2 ,3 ,4 :

1. *Downcomer* : it is the volume between the test section and the main vessel which allows the hydrodynamic connection between the outlet section of the Heat Exchanger (HX) with the inlet section of the feeding conduit.
2. *Feeding Conduit:* it is the inlet pipe of the test section which allows the hydrodynamic development of the upward primary flow rate towards the flow meter.
3. *Flow Meter*: it is a Venturi-Boccaglio flow meter. Bubble tubes [10] are adopted to measure the pressure gradient along the throat of the Venturi pipe. The flow meter is directly connected to the HS, without bypass, allowing to measure directly the primary flow rate through the pin bundle.
4. *Fuel Pin Simulator* (FPS): it is a mechanical structure needed to take on the Heat Source (HS). It is connected in the lower section to the flow meter, and in the upper section to the insulation volume by the coupling flange. The coupling flange assures the sealing, avoiding the insulation volume flooding by LBE. In the upper section, the FPS is hydraulically linked to the fitting volume, ensuring the continuity of the main flow path.
5. *Fitting Volume*: it is placed in the middle part of the test section, allowing the hydraulic connection between the HS and the riser.
6. *Riser*: it is a pipe connecting the fitting volume with the separator. In the lower section, a nozzle is installed to allow the argon injection.
7. *Separator*: it is a volume needed to connect the riser with the HX. It allows the separation of the LBE flowing downward into the HX from the Argon flowing in the test section cover gas through the free surface. Moreover, the separator assures that the overall LBE flow rate flows directly into the HX (shell – side) before falling down in the downcomer.
8. *Heat Exchanger:* it corresponds to the heat sink of the system. In order to promote the natural circulation along the primary flow path, it is installed in the upper part of the test section.

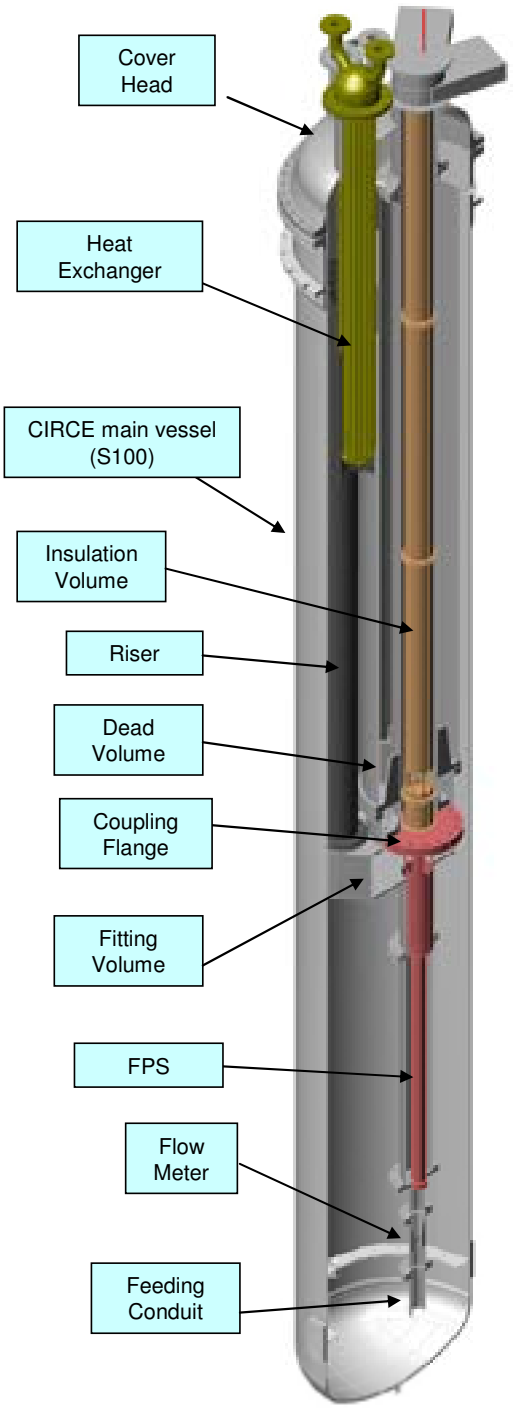

Figure 2 . ICE Test Section Overview

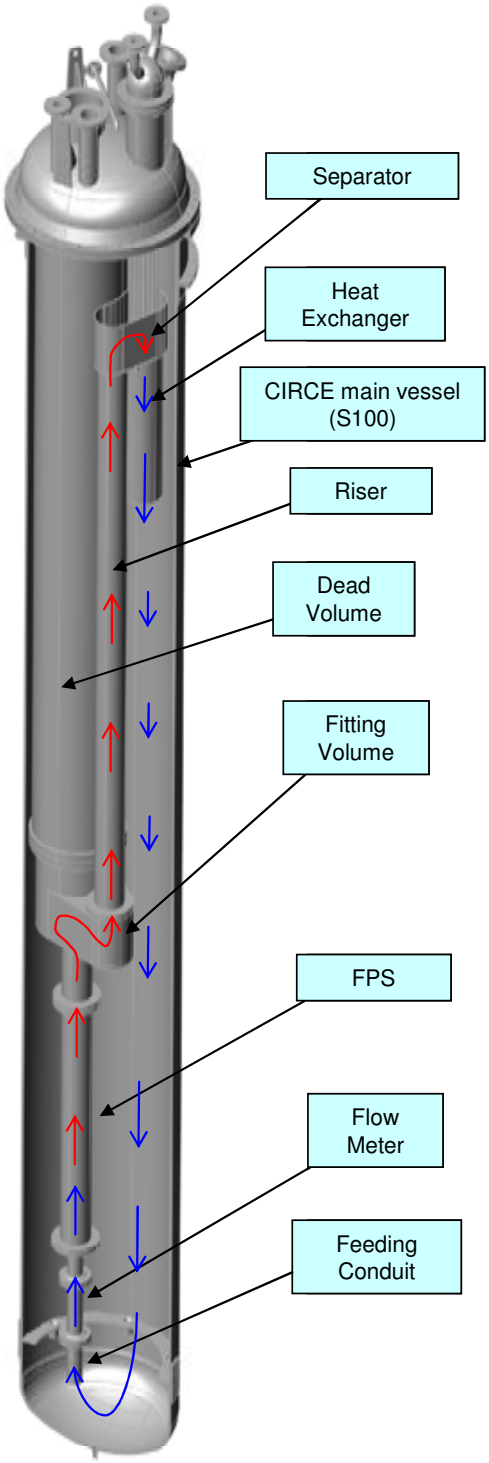

Figure 3 ICE Test Section Overview (with primary flow path)

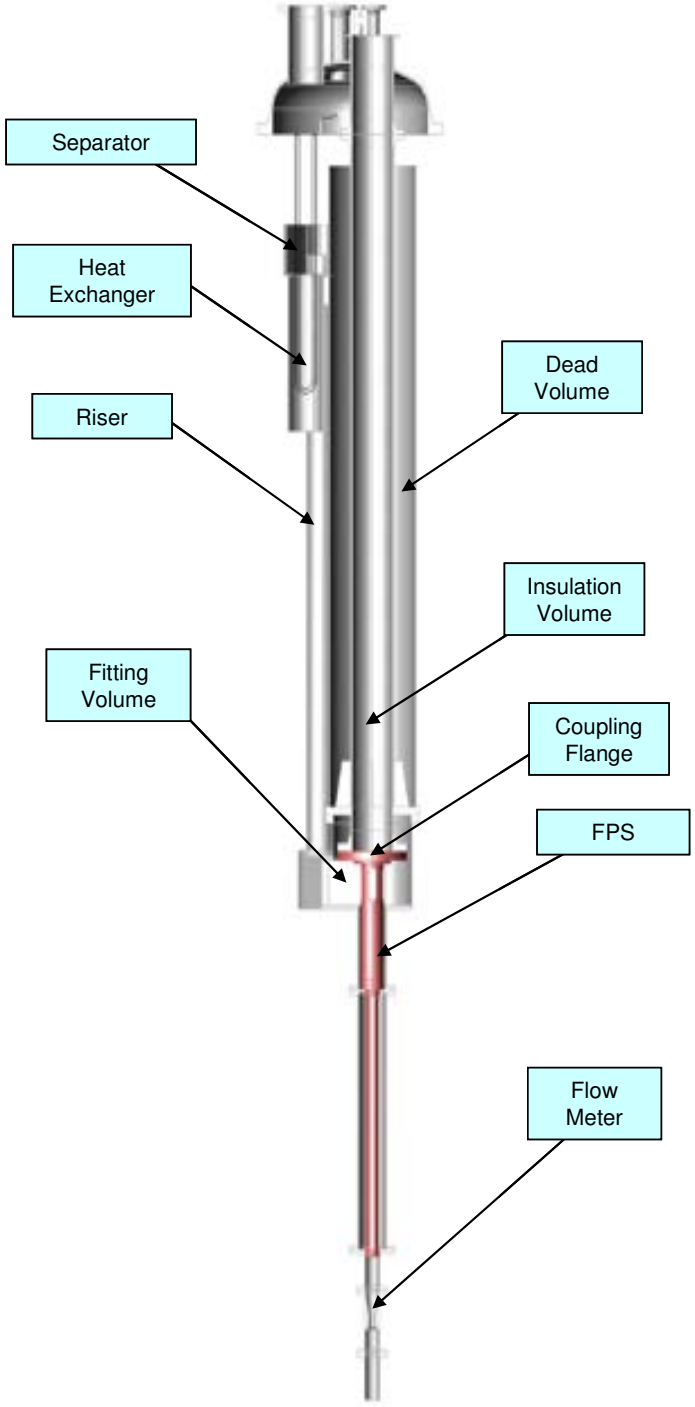

Figure 4 ICE Test Section Overview (details of the dead volume)

9. *Dead Volume*: it is a component made of two concentric pipes. The inner pipe is connected, by bolted junctions, to the FPS (by the coupling flange) and to the cover head. The volume inside the inner pipe is called Insulation Volume. The outer pipe is welded to the inner pipe in the lower end by a flange which allows a bolted connection between the dead volume and the fitting volume. It extends itself up to the cover gas, above the free level. The annulus between the inner and outer pipes, kept melt-free by design, is linked to the cover gas and filled by a thermal insulator in order to reduce the radial heat flux towards the insulation volume.

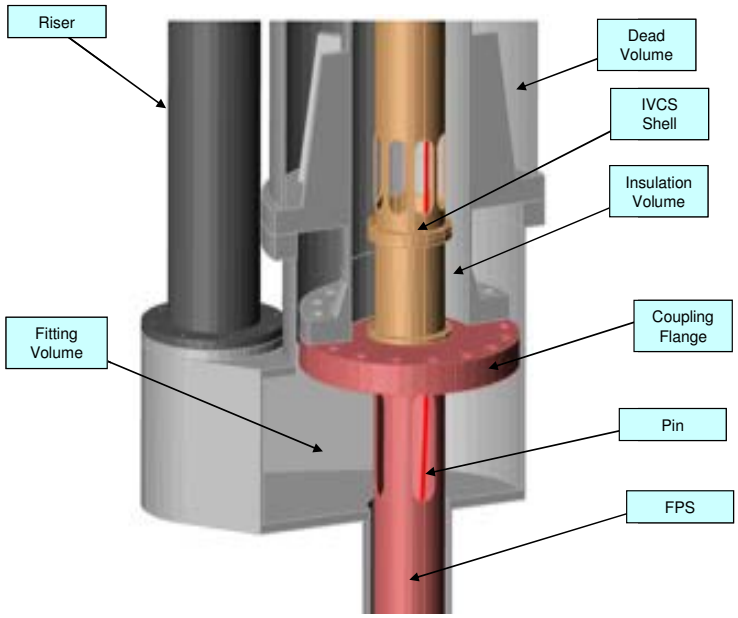

Figure 5 ICE Test Section (details of the coupling flange)

10. *Insulation Volume*: it encloses the power supply rods to feed the Heat Source (HS). As will be discussed in the following, the power supply rods will consist of wrapped copper rods or soft electrical cables depending on the kind of pins adopted to realize the HS. Moreover, in the case of soft electrical cables, the insulation volume will enclose also the electrical connection to the pins. Due to the self heating of the power supply rods, an insulation volume cooling system (IVCS) has been foreseen. To realize it, a thin shell (see figure 5) is inserted into the insulation volume to surround the power supply rods. It extends from the

coupling flange up to the cover head. The shell is hydraulically linked to the insulation volume at the bottom. Air is injected from the top in the annulus between the inner pipe and the shell. It flows downward and comes inside the shell at the bottom. Then, flowing upward it cools the power supply rods (see figure 6). The IVCS is designed to assure a maximum room temperature below 200°C.

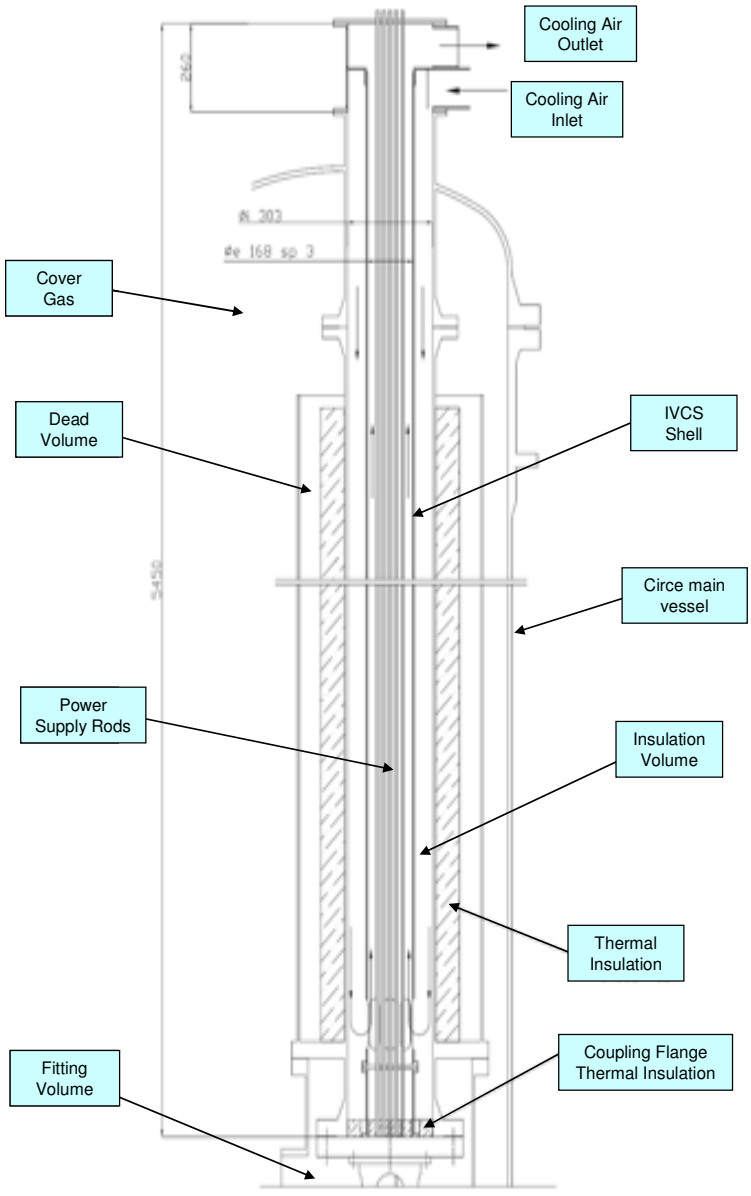

Figure 6 Details of the IVCS

2.3 Fuel Pin Simulator

The Heat Source is coupled with the test section by an appropriate mechanical structure. The HS and the mechanical structure surrounding it make up the so called Fuel Pin Simulator, FPS.

2.3.1 Heat Source

The main parameters fixed to characterize the ICE heat source in order to accomplish the integral test at best are:

1. the mean HLM temperature gradient along the HS active length ($\Delta T_{HS} / L_{act}$);
2. the average HLM velocity along the HS ($\bar{w}_{HS}$);
3. the fuel power density (q''').

The ICE heat source consists of a pin bundle made by electrical heaters with a nominal thermal power of 800 kW; it has been designed to achieve a $\Delta T_{HS} / L_{act}$ value of 100 °C/m, a pin power density of 500 W/cm^3 and an average liquid metal velocity of 1 m/s, in accordance with the reference values adopted for the ETD concepts (see table 2).

The ICE heat source consists of 37 pins placed in a wrapped hexagonal lattice with a pitch to diameter ratio of 1.8 (see figure 7).

Each pin has an outer diameter of 8.2 mm, a power about 25 kW and a wall heat flux of 1 MW/m^2, as indicated in table 2. The foreseen active length is 1000 mm and the adopted cladding material is AISI 316L.

To get an average LBE velocity of 1 m/s, a flow rate of 55.2 kg/s is needed through the HS.

As already mentioned, the main difference between the ICE Heat Source and ETD fuel assembly concepts is the P/D ratio value.

In fact, a so high P/D value has been adopted in order to reduce the overall pressure drop along the primary flow path, preserving the high thermal performance of the heat source .

Due to the available pumping system in the CIRCE facility, the gas lift pumping system, and in order to perform the ICE activity, it has been necessary to decrease as much as possible the pressure drop along the heat source, which is about 70% of the overall pressure drop.

The gas lift technique [9] was successfully tested and qualified during the previous experimental campaigns performed in CIRCE [10,11], and a pressure head of 40 kPa is available to promote the LBE circulation along the flow path.

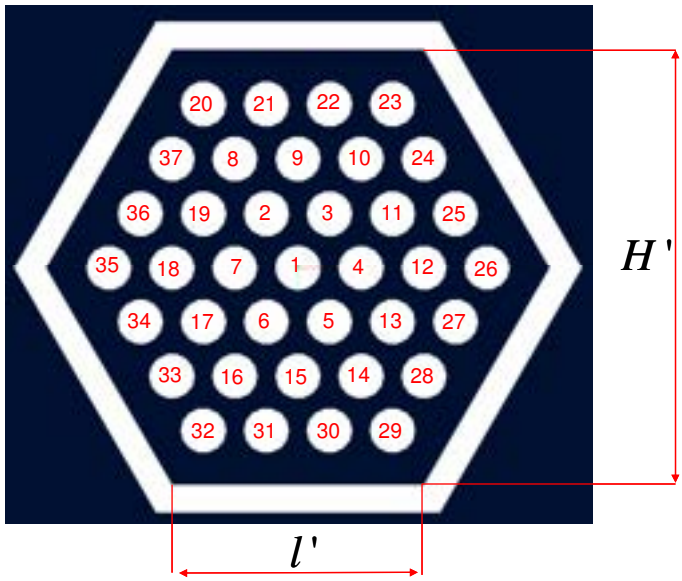

Figure 7 .Cross Section of the ICE Heat Source. (l'=55.4mm, H'=96mm)

2.3.2 Fuel Pin Technology

The fuel rods inside the heat source will be simulated by electrical pins. The electrical pin adopts a double wire solution geometry for the pin manufacturing, as reported in figure 8. For this solution, the foreseen input voltage is 200 V while the current is 125 A.

Due to the internal geometry adopted for the Bifilar-type pins, the thermal flux around the pins is not uniform.

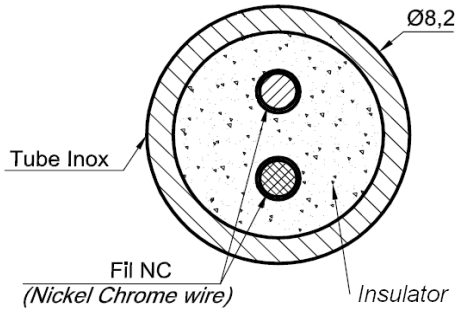

Figure 8: Cross Section of the pin Bifilar-type (active zone)

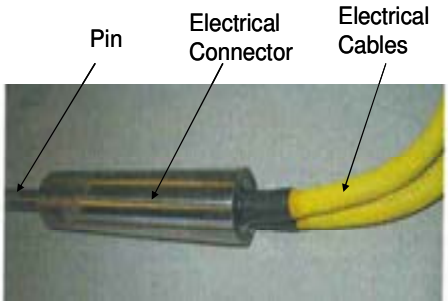

Figure 9. *Bifilar-type electrical connections (placed outside the Insulation Volume)*

For the Bifilar-type technology, the maximum length available for the cold part is more than 6 m, allowing to place the electrical connections outside the test section, simplifying the design of the IVCS. In this case the maximum room temperature to assure inside the insulation volume is 350°C.

2.3.3 FPS Mechanical Structure

Inside the Heat Source, the relative position between the pin bundle and the wrapper is assured by three appropriate grid assemblies (see figure 10) placed along the axis of the component and fixed to the wrapper.

The grid assemblies, made in AISI 316L, are designed to allow the axial and transverse thermal dilatations of the pins, avoiding thermal stress during the

operations, and to let the coolant flow through the bundle minimizing the pressure drops.

The hexagonal wrapper has a length of 1700 mm, to arrange two mixing zones (350 mm length) for the coolant, upward and downward of the heater.

The upper and lower spacer grids are placed at the interface between the active and non-active length of the pins to enclose the mixing zones.

The middle spacer grid is placed in the middle section of the bundle active length.

From the hydraulic point of view, the FPS assures that the overall LBE flow rate runs along the HS, without any by-pass. Moreover, the FPS allows to couple the HS with the test section.

The FPS consists of the following main components

- *Coupling Flange.* It allows to couple the FPS with the test section. It is connected by a sealed bolted junction with the insulation volume (see figures 2 ,4, 5) and by a welded joint with the release pipe (see figure 10). By means of appropriate connectors (Swagelok – type) placed on the coupling flange, the heating pins extends inside the insulation volume, where the junctions with the power supply rods are made. Moreover, the connectors allow to support the pins, thus ensuring the sealing. The Swagelok connectors realize the only axial constrain foreseen on the pins.
- *Release Pipe*. It contains the pins not-active upper length. In this zone, the pins are bended, allowing to get the pitch foreseen for the HS. Moreover, it performs the hydraulic connection between the outlet section of the HS with the fitting volume, allowing to reduce the velocity of the LBE flowing out from the HS.
- *Upper Grid Assembly*. It allows to place the heating pins in the foreseen hexagonal lattice adopted for the HS. The holes made on the component drives the pins along the HS, allowing thermal dilatation. On the Upper Grid Assembly no penetrations are placed for the LBE flow rate crossing. In fact, the HLM flows inside the release pipe through appropriate slotted holes located on the hexagonal wrapper. (see figure 10)
- *FPS Upper Alignment*. It permits to link the hexagonal wrapper with the release pipe.

- *Hexagonal Wrapper*. It surrounds the pins active length along the heating section, and the not-active length along the mixing zones placed upward and downward the HS (see figure 10). By means of the hexagonal wrapper, a fuel assembly element similar to the ones foreseen for the ETD concepts [4-8] (XT-ADS, EFIT) is simulated. In the upper part, appropriate slotted holes are placed on the faces of the wrapper to hydraulically connect the pin bundle with the release pipe.

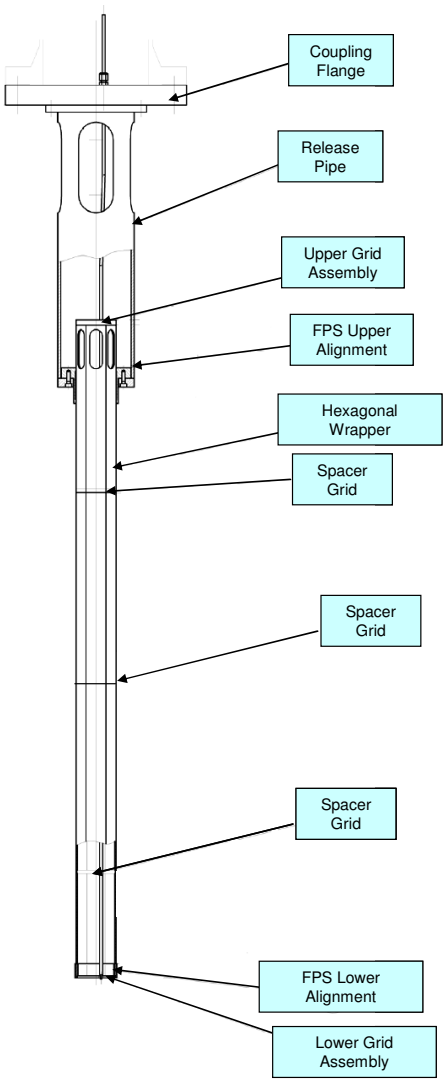

Figure 10. FPS Mechanical Drawing

- *Spacer Grids*. The spacer grid assuring the relative position of the pins

inside the bundle, improves the mixing of the coolant and guarantees a uniform and unvarying sub-channel cross section during the tests. They are made of AISI 316L and fixed to the wrapper, allowing the thermal dilatation during the tests.

- *FPS Lower Alignment*. it allows to link the hexagonal wrapper with the lower grid assembly.
- *Lower Grid Assembly.* It keeps in the right position the pins placed on the hexagonal lattice, by use of appropriate circular holes. These penetrations realize a radial constrain for the pins, allowing the axial dilatations. On the Lower Grid Assembly appropriate additional slotted holes are placed to allow the LBE flow rate crossing, linking directly the flow meter with the FPS.

2.3.4 Heat Source Thermal – Hydraulic Design

The choice of a pin bundle to simulate the HS for an integral test has been made to improve the cooling of the HS, thus avoiding the overheating of the cladding material [1] .

For the preliminary evaluations on the thermal performance of the HS, an infinite lattice will be considered. The main parameters which characterize the sub-channel are:

- pin diameter: $D = 8.2\ mm$
- pitch to diameter ratio: $P/D = 1.8$
- active length: $L_{act} = 1000\ mm$
- fuel heat flux: $q'' = 1\ \mathrm{MW/m^2}$

Moreover, the following assumptions will be made:

- LBE inlet sub-channel temperature: $T_{LBE,in,sc} = 300°C$
- LBE sub-channel average velocity: $\overline{w}_{sc} = 1\ \mathrm{m/s}$

From the data listed above, it is possible to get (see figure 11):

$$P = 1.8D = 14.8\ mm \tag{1}$$

$$H = P\frac{\sqrt{3}}{2} = 12.8\ mm \tag{2}$$

$$A_{sc} = P^2\frac{\sqrt{3}}{4} - \frac{\pi D^2}{8} = 67.9\ mm^2 \tag{3}$$

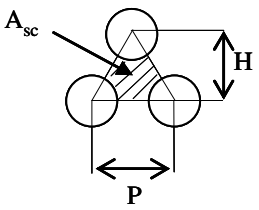

Figure 11 View of the infinite lattice sub-channel

where A_{sc} indicates the sub-channel flow area. The sub-channel wetted perimeter $P_{w,sc}$ can be calculated as follows:

$$P_{w,sc} = \frac{\pi D}{2} = 12.9\ mm \tag{4}$$

so the sub-channel hydraulic diameter $D_{h,sc}$ is:

$$D_{h,sc} = \frac{4A_{sc}}{P_{w,sc}} = D\left[\frac{2\sqrt{3}}{\pi}\left(\frac{P}{D}\right)^2 - 1\right] = 21.1\ mm \tag{5}$$

The primary flow rate along the sub-channel results to be:

$$\dot{m}_{sc} = \bar{\rho}_{LBE,sc}\bar{w}_{sc}A_{sc} = 0.7\ \frac{\mathrm{kg}}{\mathrm{s}} \tag{6}$$

where $\bar{\rho}_{LBE,sc}$ is the LBE average density along the sub-channel evaluated at the LBE average temperature along the sub-channel.

As a first approximation, an average temperature of 350°C ($\bar{T}_{LBE,sc}$) has been assumed. It is the same average temperature as the one foreseen for the integral experiment

$$\bar{\rho}_{LBE,sc} = 10271.2\ \frac{\mathrm{kg}}{\mathrm{m}^3}$$

as reported in reference [17].

Adopting the same criteria, the following values will be adopted for the LBE thermo physical properties:

$$\bar{\mu}_{LBE,sc} = 1.7 \cdot 10^{-3} \text{ Pa s}$$

$$\bar{C}p_{LBE,sc} = 144.7 \ \frac{\text{J}}{\text{kg K}}$$

$$\bar{\kappa}_{LBE,sc} = 13.1 \ \frac{\text{W}}{\text{m K}}$$

Considering the axial coordinate z along the sub-channel, the energy transport equation can be written as follows:

$$\dot{m}_{sc} \bar{C}p_{LBE,sc} dT_{LBE,b,sc}(z) = \frac{\pi D}{2} q''(z) dz \tag{7}$$

where $T_{LBE,b,sc}(z)$ indicates the LBE bulk temperature along the channel. Because q'' is uniform along the pins, the integration of the equation (7) allows to get:

$$\dot{m}_{sc} \bar{C}p_{LBE,sc} \left(T(z)_{LBE,b,sc} - T_{LBE,in,sc} \right) = \frac{\pi D}{2} q'' z \tag{8}$$

Then, as it is possible to note, the LBE bulk temperature linearly increases along the sub-channel.

$$T(z)_{LBE,b,sc} = \frac{\pi D q''}{2 \dot{m}_{sc} \bar{C}p_{LBE,sc}} z + T_{LBE,in,sc} \tag{9}$$

For $z = L_{act}$, the thermal difference between the inlet and outlet section $\Delta T_{LBE,sc}$ of the sub-channel is achieved

$$\dot{m}_{sc} \bar{C}p_{LBE,sc} \Delta T_{LBE,sc} = \frac{\pi D}{2} L_{act} q'' \tag{10}$$

so

$$\Delta T_{LBE,sc} = \frac{\pi D L_{act}}{2 \dot{m}_{sc} \bar{C}p_{LBE,sc}} q'' = 127 \ ^{\circ}\text{C} \tag{11}$$

From the results reported above, the $\bar{T}_{LBE,sc}$ along the sub-channel is 363.5 °C instead of 350 °C; due to this small difference on the LBE average temperature, no

variations on the calculated flow rate are expected. The assumption of a LBE average temperature of 350 °C is then confirmed.

The Reynolds number along the channel is:

$$\mathrm{Re}_{sc} = \left(\frac{\overline{\rho}_{LBE,sc} \overline{w}_{sc} D_{h,sc}}{\overline{\mu}_{LBE,sc}} \right) = 1.3 \cdot 10^5 \tag{12}$$

The Darcy-Weisbach friction factor can be estimated by the Blasius correlation as:

$$f_{sc} = 0.316\,\mathrm{Re}^{-\frac{1}{4}} \approx 0.0166 \tag{13}$$

and the resulting friction velocity is

$$w_\tau = \sqrt{\frac{f_{sc}}{8}}\,\overline{w}_{sc} \approx 0.0456\,\mathrm{m/s} \tag{14}$$

The resulting friction Reynolds number based on half diameter can be computed as:

$$\mathrm{Re}_{sc,\tau} = \left(\frac{\overline{\rho}_{LBE,sc} w_\tau D_{h,sc}/2}{\overline{\mu}_{LBE,sc}} \right) \approx 2960 \tag{15}$$

The hydrodynamic boundary layer thickness δ_{hy} can be computed on the basis of the wall unit as:

$$\delta_{hy} \approx 50\, y_1^+ = 50 \left(\frac{\overline{\mu}_{LBE,sc}}{\overline{\rho}_{LBE,sc} w_\tau} \right) \approx 0.18\,\mathrm{mm} \tag{16}$$

From these latter values, the reference pressure drop per unit length p_z of the sub-channel can be quantified as:

$$p_z = \frac{f_{sc}}{D_{h,sc}} \left(\frac{\overline{\rho}_{LBE,sc} \overline{w}_{sc}^2}{2} \right) \approx 4000\,\mathrm{Pa/m} \tag{17}$$

These latter values are referred to a hydrodynamic fully developed condition. This latter condition is actually realized only in the upper second half of the bundle. In fact, the hydrodynamic entry length L_{hy} can be roughly evaluated as [18]

$$\frac{L_{hy}}{D_{h,sc}} \gtrsim 30 \tag{18}$$

which implies:

$$L_{hy} \approx 650 \text{ mm} \tag{19}$$

so the LBE flow results to be hydrodynamically fully developed only in the upper part of the HS. Moreover, as it is well known [16,18], for Liquid Metals the Prandtl number, Pr, is quite lower than 1;

$$\mathrm{Pr} = \left(\frac{\bar{\mu}\bar{C}p}{\bar{\kappa}} \right)_{LBE,sc} = 0.018 \tag{20}$$

The effect is that the thermal boundary layer δ_{th} is larger than the hydrodynamic boundary layer δ_{hy}, and the thermal development length L_{th} is larger than L_{hy}. On this latter issue, for example the theoretical-experimental study [19] reports a thermal development in the turbulent range and low Prandtl number fluids, expressed by

$$L_{th} / D_{h,sc} \approx 0.2 \cdot \mathrm{Re}_{sc} \, \mathrm{Pr} / 4 = 0.2 \cdot \mathrm{Pe}_{sc} / 4 \tag{21}$$

where Pe_{sc} is the sub-channel Peclet number and governs the thermal behaviour in liquid metal flows.

From equation (21), for the present Peclet number of about 2400, it follows:

$$L_{th} / D_{h,sc} \approx 120 \;\Rightarrow\; L_{th} \approx 2500 \text{ mm} \tag{22}$$

which implies that, according to this correlation, the thermal boundary layer will never be fully developed within the bundle.

Nevertheless, for engineering purposes, to simplify the HS preliminary thermal analysis, a thermally and hydrodynamically fully developed flow will be assumed along the sub-channel.

Under the hypothesis introduced above, the Nusselt number Nu_{sc} has been evaluated adopting the Ushakov [20] correlation for lattices. Let:

$$X = \frac{P}{D} \tag{23}$$

then:

$$\mathrm{Nu}_{sc} = 7.55X - 20X^{-13} + 0.041X^{-2} \, \mathrm{Pe}_{sc}^{\,0.56+0.19X} \tag{24}$$

The Ushakov correlation is valid for turbulent flow in fuel bundles arranged in triangular lattice with $1.3 < X < 2.0$ and $150 < Pe < 4000$. For the ICE heat source:

$$X = 1.8$$

$$\mathrm{Pe}_{sc} = \mathrm{Re}_{sc}\,\mathrm{Pr} \approx 2402$$

so, from equation (24)

$$\mathrm{Nu}_{sc} = 27.75$$

The thermal boundary layer thickness is of the order:

$$\delta_{th} \approx 3\frac{D_{h,sc}}{\mathrm{Nu}_{sc}} \approx 0.9\,\mathrm{mm} \tag{25}$$

The average heat transfer coefficient along the sub-channel $\bar{h}_{sc}$ is evaluated by the following equation:

$$\bar{h}_{sc} = \frac{\mathrm{Nu}_{sc}\bar{\kappa}_{LBE,sc}}{D_{h,sc}} = 17300\ \frac{\mathrm{W}}{\mathrm{m}^2 K} \tag{26}$$

Using the Newton equation of convection [18], it is possible to write the pin heat flux as function of the temperature difference between the LBE bulk and the pin wall:

$$q''(z) = \bar{h}_{sc}(z)\left(T_w(z) - T_{LBE,b}(z)\right) \tag{27}$$

Neglecting the axial conduction along the pin, and considering, coherently with the fully developed flow hypothesis, the heat transfer coefficient constant along the sub-channel, the temperature drop between fluid bulk and wall is independent of *z* and of the order:

$$\Delta T_{w,b} = \left(T_w(z) - T_{LBE,b}(z)\right) = q''/\bar{h}_{sc} \approx 57.8\,°C \tag{28}$$

Substituting equation (9) in equation (28), it follows:

$$q'' = \bar{h}_{sc}\left(T_{w,sc}(z) - \frac{\pi D q''}{2\dot{m}_{sc}\bar{C}p_{LBE,sc}}z - T_{LBE,in,sc}\right) \tag{29}$$

$$T_{w,sc}(z) = \left[\frac{1}{\bar{h}_{sc}} + \frac{\pi D}{2\dot{m}_{sc}\bar{C}p_{LBE,sc}}z\right]q'' + T_{LBE,in,sc} \tag{30}$$

As the LBE bulk temperature, the pin wall temperature increases linearly, so that the maximum value is achieved at the outlet section of the sub-channel:

$$T_{w,\max} = \left[\frac{1}{\bar{h}_{sc}} + \frac{\pi D L_{act}}{2\dot{m}_{sc} \bar{C}p_{LBE,sc}} \right] q'' + T_{LBE,in,sc} \tag{31}$$

The maximum cladding temperature estimated for the infinite lattice sub-channel under investigation results to be:

$$T_{w,\max} = 482\,°C$$

Considering the finite pin bundle, made of 37 active pins, it is possible to evaluate the actual hydraulic diameter, $D_{h,HS}$.

The wrapper internal area (see fig. 7) is evaluated as:

$$A_W = 6\frac{1}{2}\left(\frac{H'}{2} l' \right) = 7981.3\ mm^2 \tag{32}$$

so the HS actual flow area is:

$$A_{HS} = A_W - N_r \pi \frac{D^2}{4} = 6027.3\ mm^2 \tag{33}$$

where N_r is the number of pins placed inside the wrapper.

The HS wetted perimeter is:

$$P_{w,HS} = 6l' + N_r \pi D = 1269.1\ mm \tag{34}$$

Finally the HS actual hydraulic diameter is:

$$D_{h,HS} = \frac{4A_{HS}}{P_{w,HS}} = 19\ mm \tag{35}$$

and, due to an average temperature ($\bar{T}_{LBE,HS}$) of 350°C and to an average velocity ($\bar{w}_{HS}$) of 1 m/s, the Reynolds Number along the HS results to be:

$$\mathrm{Re}_{HS} = \left(\frac{\bar{\rho}_{LBE,HS} \bar{w}_{HS} D_{h,HS}}{\bar{\mu}_{LBE,HS}} \right) = 1.3 \cdot 10^5 \tag{36}$$

From equation (18), the hydraulic development length results to be 570 mm, so a hydrodynamically fully developed flow is assumed also for the HS.

The flow rate through the HS is evaluated as:

$$\dot{M} = \bar{\rho}_{LBE,HS} \bar{w}_{HS} A_{HS} = 66.2 \text{ kg/s} \tag{37}$$

and applying the energy transport equation, the temperature difference between the inlet and outlet section of the HS is calculated:

$$\Delta T_{LBE,HS} = \frac{Q_{th,HS}}{\dot{M} \ \bar{C}p_{LBE,HS}} = 99.4°C \tag{38}$$

where $Q_{th,HS}$ is the HS thermal power (maximum):

$$Q_{th,HS} = N_r \pi D L_{act} q'' = 953.2 \text{ kW} \tag{39}$$

From equation (38), it is possible to note as the foreseen HS outlet temperature is 400°C, in agreement with the design parameters, and the LBE average temperature is 350°C, as assumed during the calculations.

2.3.5 CFD Pin Bundle Calculation

A CFD analysis has been performed on the pin bundle to confirm numerically the preliminary thermal analysis of the previous section and to perform an a-priori estimate of the error in the heat transfer measurements.

For a reference study, the fully developed flow in the generic sub-channel have been modelled and simulated. The reference domain with the computational mesh is shown in figure 12 as the hexagonal area surrounding the generic pin; periodic conditions have been applied to the couples of parallel sides of the hexagon.

With such boundary conditions, the domain is representative of an infinite triangular lattice, and it is an equivalent representation of the sub-channel sketched in figure 11.

In the vertical z-direction, i.e. in the streamwise direction along the axis of the pin, periodic conditions have been imposed for all variables, with a pressure-driving forcing term p_z in the momentum equation to simulate a fully developed flow. A value of $p_z = 4000 \, \text{Pa/m}$ has been imposed coherently to the pressure loss estimated in the

previous section; this is equivalent to impose a friction Reynolds number $\mathrm{Re}_{sc,\tau} \approx 2960$.

At the pin wall, a constant heat flux $q'' = 1\,\mathrm{MW/m^2}$ has been imposed; this would lead to a global temperature gradient in the z-direction. This gradient is balanced by a power sink term in the fluid, weighted by the local vertical velocity. This numerical trick allows to impose periodic conditions also for the temperature in the *z*-direction, to keep constant the bulk temperature, and to recover the exact temperature asymptotic distribution in fully developed conditions for the generic section, i.e. the temperature differences in the section will be exact as well as the heat transfer coefficients.

A conventional bulk temperature $T_{LBE,b} = 350\,°\mathrm{C}=623.16\,\mathrm{K}$ has been fixed for all the computations.

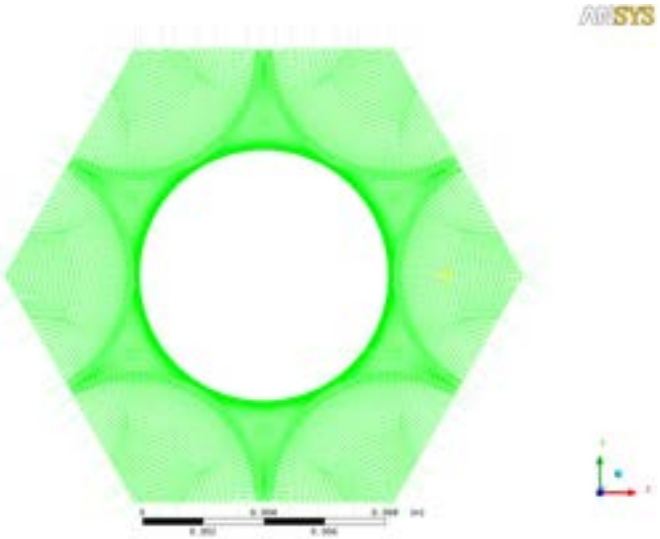

Figure 12 View of the infinite lattice sub-channel

The simulations have been performed by using ANSYS-CFX 11 with the Shear Stress Transport (SST) *k-ω* turbulence model and a second-order scheme for convective terms. The turbulent Prandtl number has been set to 0.9, as suggested by several studies on heat transfer in heavy liquid metals at high Peclet number [14].

The mesh (shown in figure 12) is multi-block structured and it has y^+=1 at the first grid point close to the wall with several points within the viscous sublayer and the direct solution of the turbulent equations within the boundary layer. A grid

independence study was carried out on three meshes named A, B and C from the coarsest to the finest one respectively. The main features of the three meshes with the main global quantities obtained from the computations are summarized in table 3. N_{2D}^{CELL} represents the number of cells in the section, $\mathrm{Re}_{sc,\tau}$ is the imposed friction Reynolds number, while Re_{sc} and Nu_{sc} are the resulting Reynolds and Nusselt numbers respectively; the Darcy-Weisbach friction factor can be computed as:

$$f_{sc} = 32\left(\frac{\mathrm{Re}_{sc,\tau}}{\mathrm{Re}_{sc}}\right)^2 \tag{40}$$

The grids have three to six grid points within the viscous sub-layer from the coarsest to the finer mesh, and the full numerical convergence has been reached on the equations residuals. Both the friction factor and the Nusselt number clearly reach asymptotic values increasing the number of nodes, from mesh A to mesh C; these values represent the model solution with negligible numerical errors. Although both grid A and B could be rather accurate for this preliminary calculation with turbulence models, the high-res grid C has been adopted as reference mesh for the computations. For a pressure loss $p_z = 4000\,\mathrm{Pa/m}$ $(\mathrm{Re}_{sc,\tau} \approx 2960)$ the resulting Reynolds number is $\mathrm{Re}_{sc} \approx 1.22 \cdot 10^5$, corresponding to an average velocity $\bar{w}_{sc} \approx 0.93\ \mathrm{m/s}$. The Nusselt number is around $\mathrm{Nu}_{sc} \approx 33$, with a corresponding heat transfer coefficient $\bar{h}_{sc} \approx 19382\ \mathrm{Wm^{-2}K^{-1}}$ on the specific geometry considered.

Grid features			Quantity Imposed	Results		
Grid name	y^+_1	N_{2D}^{CELL}	$\mathrm{Re}_{sc,\tau}$	Re_{sc}	f_{sc}	Nu_{sc}
A	1	5570	2960	$1.214 \cdot 10^5$	0.0190	32.8
B	1	8040	2960	$1.222 \cdot 10^5$	0.0188	32.9
C	1	15840	2960	$1.224 \cdot 10^5$	0.0187	32.9

Table.3. Grid independence study for the fully developed sub-channel flow with pressure loss $p_z = 4000\,\mathrm{Pa/m}$ and a wall pin heat flux $q'' = 1\,\mathrm{MW/m^2}$. The sub-channel is representative of a triangular lattice with pin diameter 8.2 mm and a pitch to

diameter ratio of 1.8. The working fluid is LBE at Pr=0.018. The model used is the SST k-ω.

Figure 13 shows the axial velocity contour map in the sub-channel section; as it was expected, the boundary layer is very thin and the velocity is around 0.9-1 m/s in most of the channel cross-section area, with the periodic cell hydrodynamically decoupled from the neighbouring cells of the lattice.

Figure 14 reports the temperature contour map, which shows, as expected for liquid metals, a much larger thermal boundary layer. It should be noticed that the quasi-circular shape of the isotherms in the vicinity of the edge of the hexagonal domain expresses an almost complete thermal decoupling between the cells of the infinite lattice. This implies that the heat transfer coefficient is almost constant azimuthally at the pin wall. Pitch to diameter ratios greater than the present value of 1.8 would exhibit qualitatively a similar thermo-fluid dynamic behaviour at the same Reynolds and Prandtl numbers. On the opposite, a different shape of the isotherms is expected for $P/D_{h,sc} < 1.8$, due to the stronger coupling between the hexagonal cells of the lattice in this latter case.

Figures 15 and 16 show axial velocity and temperature profiles into the subchannel; the x coordinate is measured from the centre of the pin. The hydrodynamic boundary layer is of the order of 0.2-0.3 mm, while the thermal boundary layer of the order of 1-1.5 mm, in good accordance with the preliminary rough estimations of the previous section.

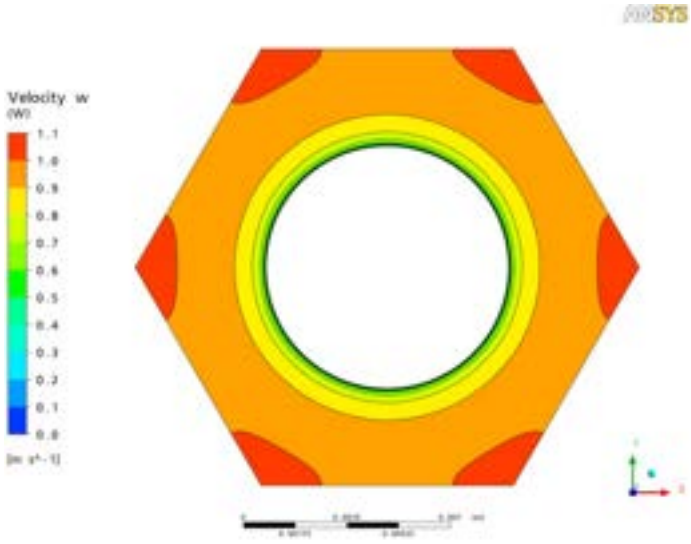

Figure 13 Contour map of the axial velocity in the sub-channel

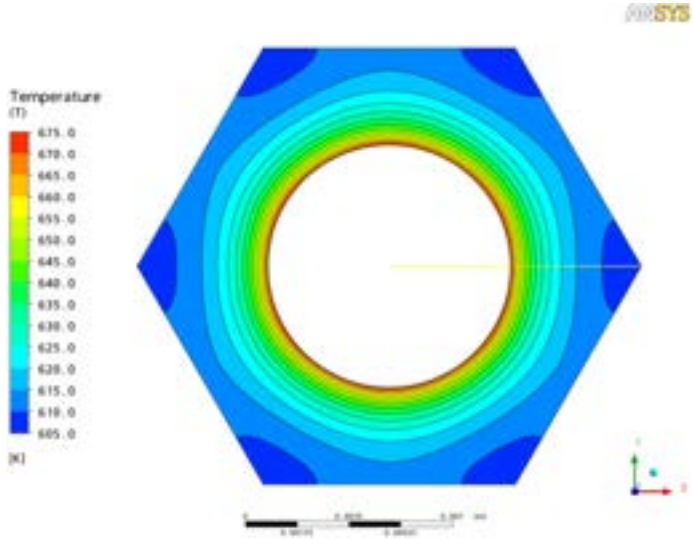

Figure 14 Contour map of the Temperature in the sub-channel

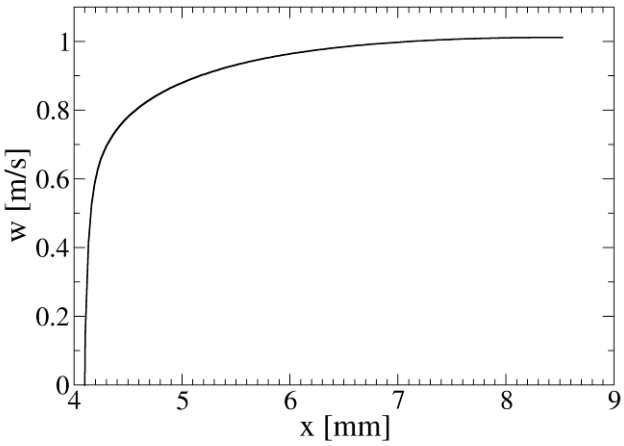

Figure 15 Axial velocity w against the distance from the centre of the pin.

A thermocouple of 0.5 mm thickness positioned at the wall, i.e. from 4.1 to 4.6 mm, would underestimate the wall temperature of about 15 K, i.e. $T_w - T_{w,TC} \approx 15\,\mathrm{K}$. On the other side, it must be reminded that the technical definition of heat transfer coefficient is based on the bulk temperature, i.e. on the velocity-weighted temperature average in the channel.

Although for unity Prandtl number fluids, where the temperature profile is practically flat, this temperature is almost equal to the one measured at the centre of

the channel, for a liquid metal with a very large boundary layer thickness, a thermocouple positioned at the centre of the channel would heavily under-estimate the bulk temperature. In the present case, for example, according to the computations, the bulk temperature is $T_{LBE,b} \approx 621\,\mathrm{K}$ while the centreline temperature is $T_{LBE,c} \approx 609\,\mathrm{K}$, with a difference of $T_{LBE,b} - T_{LBE,c} \approx 12\,\mathrm{K}$.

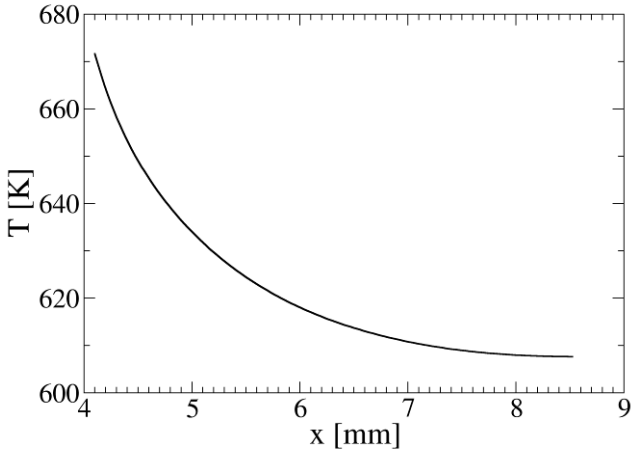

Figure 16 Temperature T against the distance from the centre of the pin.

Although these two source of error partially compensate each other, if the heat transfer coefficient is computed by using wall and centre thermocouples measurements as $\bar{h}_{sc,TC} \approx \overline{q''} / \left(T_{w,TC} - T_{LBE,c} \right)$, an over-estimation error is made with respect to the exact definition $\bar{h}_{sc} \approx \overline{q''} / \left(T_w - T_{LBE,b} \right)$. For example, in the present case this would lead to $\bar{h}_{sc,TC} \approx 21100\,\mathrm{Wm^{-2}K^{-1}}$, against $\bar{h}_{sc} \approx 19382\ \mathrm{Wm^{-2}K^{-1}}$, with an over-estimation of 10%.

If the constant wall heat flux cannot be guaranteed from an experimental point of view, like in the Bifilar-type thermocouples provided by Thermocoax for the ICE pin bundle, it is interesting to estimate the error associated with the measurement of the heat transfer coefficient. From Thermocoax technical documents, pin rods bifilar-type used in the ICE bundle exhibit an approximate azimuthal variation $\left(q''_{\max} - q''_{\min} \right) / \overline{q''} \approx 0.3$, i.e. 30%. Imposing numerically a sinusoidal heat flux varying

along the azimuthal angle θ , it is possible to obtain a picture of the temperature field by a CFD simulation.

Results are shown in figure 17, where the temperature field map in the cross section is shown. The temperature field reflects the heat flux behaviour with two maxima.

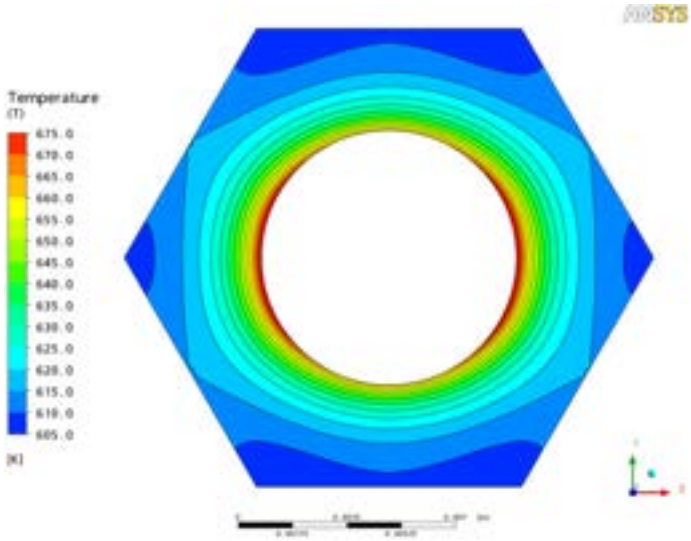

Figure 17 Contour map of the Temperature in the sub-channel in the case of azimuthal variation of the heat flux.

From an experimental point of view, in principle it is not known where the maxima are located, i.e. it is not known the pin orientation. Therefore, the temperatures measured by the wall-pinched thermocouples can be higher or lower than the average wall temperatures, and the resulting wall heat transfer evaluation will be affected by a systematic error. Evaluating numerically the local heat transfer coefficient by $h_{sc}(\theta) \approx \overline{q''} / \left[T_w(\theta) - T_{LBE,b} \right]$, it is possible to obtain a reasonable picture of the spread of the experimental measurements.

Figure 18 shows this latter azimuthal distribution on the basis of CFD computations; the azimuthal angle θ, in degrees, is measured from the yellow line of figure 14 anti-clockwise. There is an over/under-estimation maximum error of the order of 20%. It must be pointed out that this is the maximum potential error, and an actual measurement can be closer to the real value.

Moreover, this kind of error can be statistically dropped by multiple sub-channels measurements.

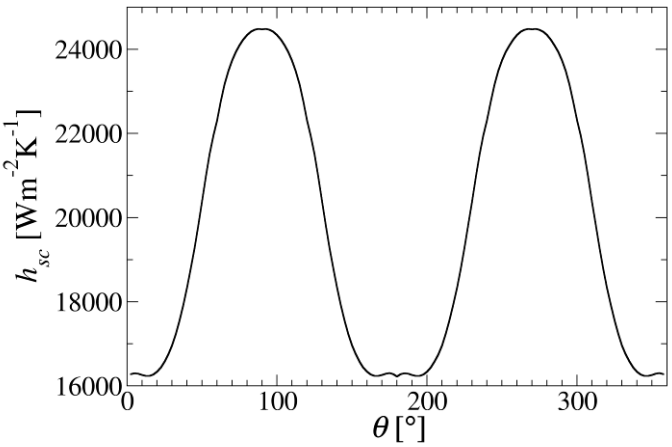

Figure 18 Heat transfer coefficient as a function of the azimuthal angle in the case of not uniform wall heat flux.

All the evaluations made by CFD analysis have been carried out under the hypothesis of fully developed flow and represent a reference. Nevertheless, doubts on the extension of the thermal entry region have been expressed in the previous sections. In particular, it is textbook knowledge that the thermal entry length can be longer than the velocity entry length for low Prandtl number fluids, but the quantification of this effect is not always known.

Therefore, an ad hoc CFD simulation has been performed to asses such an issue. The elementary periodic cell shown in figure 12 has been extruded 1 meter long, i.e. for the actual length of the active part of the ICE bundle, as shown in figure 19. 100 cells have been used to discretize the domain in the axial direction.

At the inlet section a uniform axial velocity of 1 m/s with 5% turbulence fluctuations and a temperature of 573 K have been imposed, while in the outlet section a pressure outlet condition has been fixed. These conditions allow the boundary layer to attach at the inlet and to grow through the sub-channel. In such a way, a complete 3D picture of the thermal and velocity field is available.

Figure 20 shows the behaviour of the azimuthally-averaged wall shear stress along the channel, i.e. against the axial coordinate *z*.

Figure 19 Sketch of the computational domain used to compute the entry region.

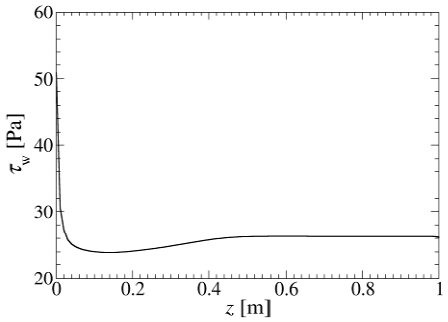

Figure 20 Wall Shear Stress τ_w against the axial coordinate z.

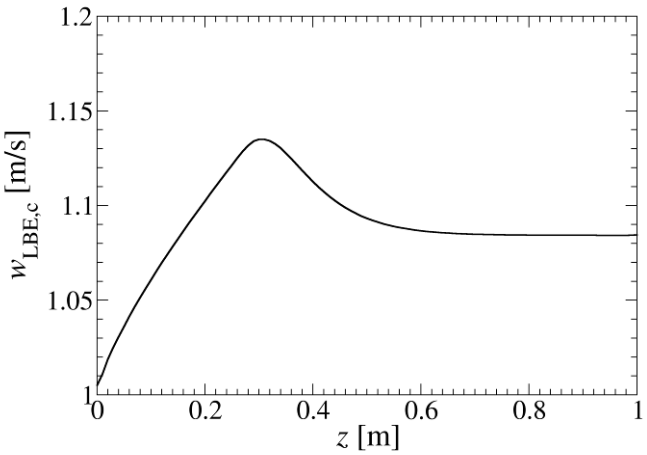

Figure 21 Axial velocity w against the axial coordinate z.

The figure shows very clearly that the velocity entry region is extended for half a channel, i.e. 0.4-0.5 m about; in the upper part of the channel the shear stress remains constant and the flow is fully developed.

Figure 21 shows the central-channel axial velocity against the axial coordinate *z*. It is remarkable the presence of a maximum in the velocity, tied to the minimum wall shear stress in figure 20.

Figure 22 shows wall and central-channel temperatures against the axial coordinate *z*. When the boundary layer attaches and grows in the lower part of the channel, the Nusselt number is higher than in the fully developed region, and it varies strongly along the channel similarly to the wall shear stress. As a consequence the wall temperature exhibit a non-linear behaviour in the entry region. The linear behaviour of the temperature profiles for *z*>0.5-0.6 [m] is symptomatic of a fully developed flow. From this CFD computation, it emerges that the thermal entry length is of the same order of the velocity entry length for heavy liquid metal flows at these Reynolds numbers around 10^5 and the estimation made in the previous sections on this issue was too pessimistic.

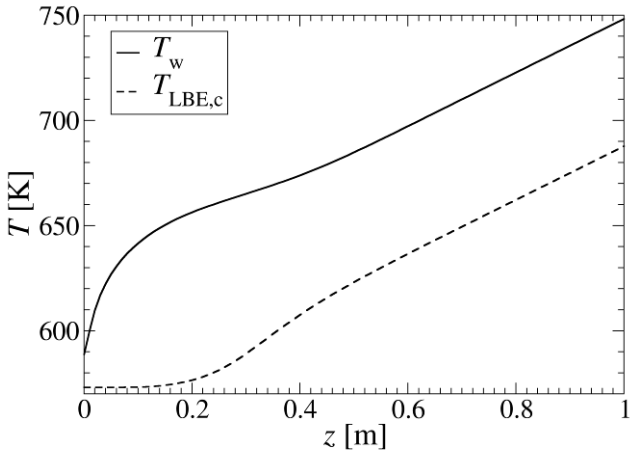

Figure 22 Wall and central-channel temperatures against the axial coordinate z.

2.4 Test Section Pressure Drop

The gas lift technique has been utilized to promote the LBE circulation along the ICE test section flow path. This technique was tested and qualified in previous experimental campaigns performed in the CIRCE facility [11]. The results carried out show that the gas lift is a reliable technique up to an average riser void fraction of 10%. Above this value, a saturation phenomena in the two phase flow was observed.

The maximum driving force available for the integral tests can be evaluated as follow:

$$\Delta p_{DF} = \Delta\rho g H_r \tag{41}$$

where H_r is the riser height, and:

$$\Delta\rho = \bar{\rho}_{LBE} - \rho_{r,TP} \tag{42}$$

The two phase flow mean density inside the riser, $\rho_{r,TP}$, can be evaluated from the void fraction α; let $\bar{\alpha}$ be the average void fraction along the riser:

$$\rho_{r,TP} = \bar{\alpha}\bar{\rho}_g + (1-\bar{\alpha})\bar{\rho}_{LBE} \tag{43}$$

and so:

$$\Delta\rho = \bar{\rho}_{LBE} - \bar{\alpha}\bar{\rho}_g - (1-\bar{\alpha})\bar{\rho}_{LBE} = \bar{\alpha}\left(\bar{\rho}_{LBE} - \bar{\rho}_g\right) \tag{44}$$

Because the average gas density along the riser $\bar{\rho}_g$ is much smaller than $\bar{\rho}_{LBE}$, the following approximation is made:

$$\Delta\rho = \bar{\alpha}\left(\bar{\rho}_{LBE} - \bar{\rho}_g\right) \approx \bar{\alpha}\bar{\rho}_{LBE} \tag{45}$$

and:

$$\Delta p_{DF} = \bar{\alpha}\bar{\rho}_{LBE} g H_r \tag{46}$$

Making use of the following values:

$$\bar{\alpha}_{\max} = 0.1$$
$$\bar{\rho}_{LBE} = 10271.2 \text{ kg/m}^3$$
$$H_r = 3.8 \ m$$

and applying equation (46), the maximum driving force available for the primary circulation result to be:

$$\Delta p_{DF}^{\max} = 38 \text{ kPa} \tag{47}$$

From the momentum transport equation [18], it is possible to write, for a closed loop in steady state condition, the following relationship:

$$\Delta p_{DF} = \Delta p_{fric} \tag{48}$$

where Δp_{fric} indicates the overall pressure drops along the primary flow path. For its evaluation, the following correlation will be adopted:

$$\Delta p_{fric} = \frac{1}{2} \frac{\dot{M}^2}{\rho_{eff} A_{eff}^2} K_{eff} \tag{49}$$

where:

- $\dot{M}$ is the primary flow rate,
- A_{eff} is the *effective* flow area,
- ρ_{eff} is the *effective* liquid metal density,
- K_{eff} is the *effective* pressure drop coefficient .

The *effective* flow area and density have been chosen matching to the Heat Source actual flow area A_{HS} and the LBE average density $\bar{\rho}_{LBE}$ along the stream respectively.

Considering the flow path divided in several branches, (heating section, heat exchanger, riser, fitting volume, downcomer, etc) for the *i-th* ones it is possible to define a local pressure drop coefficient, $K_{eff,i}$, referred to the *effective* parameters, A_{eff} and ρ_{eff}.

In fact, defining the following parameters for the *i-th* branch,

- A_i, actual flow area;
- $D_{h,i}$, actual hydraulic diameter;

- L_i hydraulic length;
- f_i, Darcy-Weisbach factor [18], evaluated taking in account the actual flow regime inside the branch under consideration;
- ρ_i liquid metal density calculated by the actual LBE temperature $T_{LBE,i}$;

the *i-th* local pressure drop coefficient can be written as :

$$K_{eff,i} = \left(f_i \frac{L_i}{D_{h,i}} + \sum_l k_{i,l} \right) \frac{\rho_{eff}}{\rho_i} \frac{A_{eff}^2}{A_i^2} \tag{50}$$

where $k_{i,l}$ is a coefficient to take in account the *l-th* singular pressure drop (entrance effect, change of direction, orifice, mass flow transducer, etc) placed along the flow path inside the *i-th* branch.

From equations (50), the *effective* pressure drop coefficient can be written as:

$$K_{eff} = \sum_i K_{eff,i} \tag{51}$$

In the following, the equation (50) will be applied to evaluate the local pressure drop coefficient for the main components which compose the test section. In particular, circulating along the test section, the LBE flows through the feeding conduit, the flow meter, the heat source, the fitting volume, the riser, the heat exchanger and finally through the downcomer (see figure 3).

The values of the *effective* parameters to consider are:

$\mathrm{A}_{eff} = 5376.1 \text{ mm}^2$ $\rho_{eff} = 10271.2 \text{ kg/m}^3$ $\dot{\mathrm{M}} = 55.2 \text{ kg/s}$

Inlet Feeding Conduit

The LBE primary flow rate, flowing downward in the downcomer (see figure 3), curves in the test section by the feeding conduit.

To estimate the entrance effect from the pressure drop point of view, the following correlation [21] has been adopted:

$$k_{IFC} = \frac{1}{2}\left(1 - \frac{A_d}{A_u}\right)^{3/4} \tag{52}$$

where A_d and A_u indicates the downstream and upstream flow area respectively. In particular, in this case A_d is the feeding conduit flow area A_{FC}, and A_u is the downcomer flow area; so:

$$A_d = A_{FC} = 8213 \text{ mm}^2 \qquad A_u = 1130973 \text{ mm}^2$$

and

$$k_{IFC} = 0.50$$

Because an entrance effect is evaluated, the first term of equation (50) can be ignored, obtaining the following value

$$K_{eff,IFC} = k_{IFC} \frac{\rho_{eff}}{\rho_{FC}} \frac{A_{eff}^2}{A_{FC}^2} = 0.27$$

having a ratio $\rho_{eff} / \rho_{LGA} \approx 1$, and a ratio $\frac{A_{eff}^2}{A_{FC}^2} = 0.54$.

Feeding Conduit

Applying equation (50), in the first term the Darcy-Weisbach factor f_{FC} has to be evaluated. For this aim, the Churchill Correlation [18] has been adopted. This correlation is valid for a wide range of the Reynolds number, containing the laminar, transition and turbulent region.

$$f = 8\left[\left(\frac{8}{\text{Re}}\right)^{12} + \frac{1}{(A+B)^{3/2}}\right]^{1/12} \tag{53}$$

$$A = \left[2.457 \ln\left(\frac{1}{(7/\text{Re})^{0.9} + 0.27(\varepsilon/D_h)}\right)\right]^{16} \qquad B = \left[\frac{37530}{\text{Re}}\right]^{16}$$

ε is the average roughness of the components, assumed to be 0.000032 m.

For the Feeding Conduit, the parameters are:

$$A_{FC} = 8213 \text{ mm}^2 \qquad D_{h,FC} = 102 \text{ mm} \qquad L_{FC} = 903 \text{ mm}$$

$$\overline{w}_{FC} = 0.65 \text{ m/s} \qquad \text{Re}_{FC} = 4.15E+05$$

Using the Churchill Correlation, we obtain:

$$A = 2.78E + 21 \qquad B = 2.0E - 17$$

and so:

$$f_{FC} = 0.017$$

Along the Feeding Conduit, no singular pressure drops are placed, and so the following assumption is made:

$$\sum_l k_{HS,l} = 0$$

Finally, it is possible to write:

$$\frac{\rho_{eff}}{\rho_{FC}} \approx 1 \qquad \frac{A_{eff}^2}{A_{FC}^2} = 0.54 \qquad f_{FC}\frac{L_{FC}}{D_{h,FC}} = 0.15$$

and:

$$K_{eff,FC} = \left(f_{FC}\frac{L_{FC}}{D_{h,FC}} \right)\frac{\rho_{eff}}{\rho_{FC}}\frac{A_{eff}^2}{A_{FC}^2} = 0.08$$

Venturi-Boccaglio Flow Meter

A Venturi-Boccaglio flow meter has been chosen to be installed in the ICE test section for the primary flow rate measurement. This component was successfully qualified and then utilized in the previous experimental activity carried out on the CIRCE facility [3] .

The supplier of the instrument confirmed that the pressure loss due to the flow meter is about 9 kPa for the foreseen nominal LBE flow rate.

From equation (49), it is possible to find:

$$K_{eff,FM} = 2\left(\frac{\Delta p_{FM}}{\dot{M}^2} \right)\rho_{eff} A_{eff}^2 = 1.75$$

Heat Source

For the Heat Source the parameters are:

$$A_{HS} = 6027 \text{ mm}^2 \qquad D_{h,HS} = 19.0 \text{ mm} \qquad L_{HS} = 1700 \text{ mm}$$

$$\overline{w}_{HS} = 0.9 \text{ m/s} \qquad \text{Re}_{HS} = 1.1E+05$$

Applying the Churchill Correlation to the Heat Source (see equation (53)) it is possible to obtain:

$$A = 1.34E+20 \qquad B = 7.05E-08$$

and so:

$$f_{HS} = 0.024$$

Along the Heat Source, no singular pressure drop will be considered for now. The spacer grids, the lower grid assembly and the entrance effects will be considered in a successive step. So, for the HS the following assumption will be made:

$$\sum_l k_{HS,l} = 0$$

Finally, because the LBE average temperature and flow path along the HS are the reference ones, it is possible to write:

$$\frac{\rho_{eff}}{\rho_{HS}} = 1 \qquad \frac{A_{eff}^2}{A_{HS}^2} = 1 \qquad f_{HS}\frac{L_{HS}}{D_{h,HS}} = 2.2$$

and:

$$K_{eff,HS} = \left(f_{HS}\frac{L_{HS}}{D_{h,HS}} \right)\frac{\rho_{eff}}{\rho_{HS}}\frac{A_{eff}^2}{A_{HS}^2} = 2.18$$

Inlet Hexagonal Wrapper

To estimate the entrance effect of the Hexagonal Wrapper, the equation (52) has been adopted:

$$k_{IHW} = \frac{1}{2}\left(1 - \frac{A_d}{A_u} \right)^{3/4}$$

In this case, A_d is the Heat Source flow area, and A_u is the feeding conduit flow area; so:

$$A_d = A_{HS} = 6027 \text{ mm}^2 \qquad A_u = A_{FC} = 8213 \text{ mm}^2$$

and

$$k_{IHW} = 0.19$$

Because an entrance effect is evaluated, the first term of the equation (50) can be ignored, obtaining the following value

$$K_{eff,IHW} = k_{IHW} \frac{\rho_{eff}}{\rho_{HS}} \frac{A_{eff}^2}{A_{HS}^2} = 0.19$$

having the ratio $\rho_{eff} / \rho_{HS} = 1$, and the ratio $\frac{A_{eff}^2}{A_{HS}^2} = 1$.

Lower Grid Assembly

The Lower Grid Assembly (see figure 23) has been designed to keep in the right position the pins inside the HS, avoiding thermal stresses and reducing as much as possible the pressure drop.

For this reason, several solutions have been analyzed, also by mean of numerical simulations performed by CRS4 [Moreau, *Spacer Grid and Lower Grid Assembly Pressure Drops*, 2007].

In order to obtain an analytical evaluation of the pressure drop through the Lower Grid Assembly (LGA), the following correlation [21] has been adopted:

$$k_{LGA} = \frac{C_1}{F^2} + C_2 C_3 \tag{54}$$

where

$$C_1 = \left[18.78 - \frac{7.768}{F} + \frac{6.337}{F^2} \right] \exp\left\{ \left(-0.942 - 7.246F - 3.878F^2 \right) \log \text{Re}_0 \right\}$$

$$C_2 = 0.0659 \ln \text{Re}_0 + 0.1631$$

$$C_3 = \left[0.707 \left(1 - F \right)^{0.375} + 1 - F \right]^2 \frac{1}{F^2}$$

$$F = \frac{A_0}{A_u} \qquad \mathrm{Re}_0 = \frac{w_0 d_h \rho_{LGA}}{\mu_{LGA}}$$

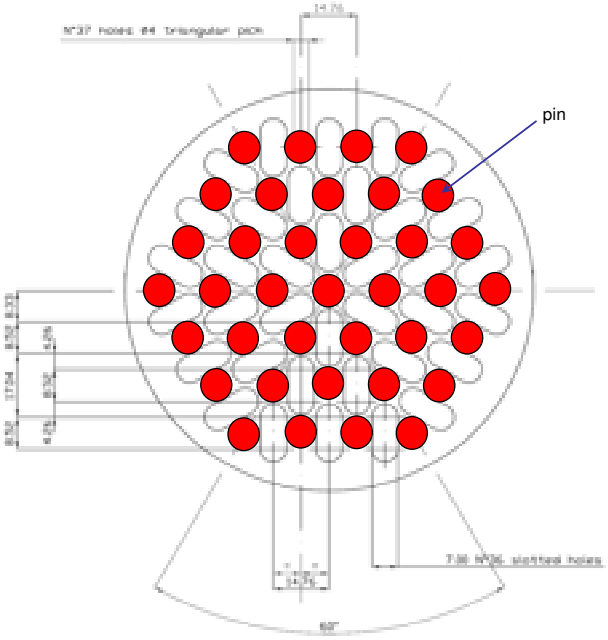

Figure 23. Sketch of the Lower Grid Assembly

A_0 and A_u indicates the clear area of the grid and the upstream flow area respectively; F is called free-area coefficient, while d_h and w_0 are the hydraulic diameter and stream velocity through the orifice.

For the Lower Grid Assembly designed for the ICE test section, the following values have been obtained considering a LBE temperature of 300°C ($T_{LBE,in}$):

$$d_h = 10.05 \text{ mm} \qquad A_0 = 3530 \text{ mm}^2 \qquad w_0 = \frac{\dot{M}}{A_0 \rho_{LGA}} = 1.52 \text{ m/s}$$

$$\mathrm{Re}_0 = 9.5E+04$$

Moreover, considering that the upstream flow area A_u is equal to the HS source flow area A_{HS} (see equation (33)), the free-area coefficient results to be

$$F = 0.59$$

and, as consequence,

$$C_1 = 0.0 \qquad C_2 = 0.92 \qquad C_3 = 2.48$$

$$k_{LGA} = 2.28$$

Because the grid is 6 mm thick, the first term of the equation (50) has been neglected, obtaining the following value

$$K_{eff,LGA} = k_{LGA} \frac{\rho_{eff}}{\rho_{HS}} \frac{A_{eff}^2}{A_{HS}^2} = 2.28$$

having a ratio $\rho_{eff} / \rho_{HS} = 1$.

Spacer Grids

The Spacer Grids (see figure 24) have to assure the correct geometry of the sub-channels inside the Heat Source. They serve to prevent the pins vibration arising as consequences of the stream turbulence along the main flow path, and to prevent the pins bending occurring due to the sub-channels thermal gradient.

To reduce the risk that a hot spot takes place in the contact zones between the pins and the spacer grids, and to decrease the thermal stresses and the pressure drop, several solutions have been analyzed. In particular, several numerical simulations have been performed by CRS4 [Moreau, *Spacer Grid and Lower Grid Assembly Pressure Drops, 2007*] to evaluate the behaviour of the designed spacer grids.

For the Spacer Grids pressure drop analytical evaluation, the equation (54) has been applied:

$$k_{SG} = \frac{C_1}{F^2} + C_2 C_3$$

Also in this case F is the free-area coefficient, that is the ratio between the spacer grid clear area and the upstream flow area.

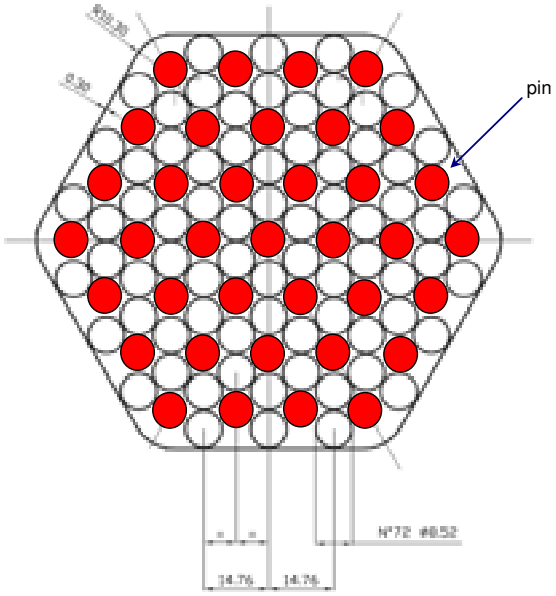

Figure 24 . Sketch of the Spacer Grid

For the Spacer Grids designed for the ICE test section, the following values have been obtained considering a LBE temperature of 300°C ($T_{LBE,in}$):

$$d_h = 7.92 \text{ mm} \quad A_0 = 4820 \text{ mm}^2 \qquad w_0 = \frac{\dot{M}}{A_0 \rho_{LGA}} = 1.12 \text{ m/s} \qquad \text{Re}_0 = 5.5E+04$$

Moreover, considering that the upstream flow area A_u is equal to the HS source flow area (see equation (33)), the free-area coefficient results to be

$$F = 0.80$$

and, as consequence,

$$C_1 = 0.0 \qquad C_2 = 0.88 \qquad C_3 = 0.20$$

$$k_{SG} = 0.48$$

Because the spacer is 10 mm thick, the first term of the equation (50) has been neglected, obtaining the following value

$$K_{eff,SG} = k_{SG} \frac{\rho_{eff}}{\rho_{HS}} \frac{A_{eff}^2}{A_{HS}^2} = 0.48$$

having a ratio $\rho_{eff} / \rho_{HS} = 1$.

As it can be possible to note, the same parameter estimated by the numerical simulations [Moreau, "*Spacer Grid Assembly and Lower Grid Assembly Pressure*

Drops", 2007], that is 0.24, is about the 33% larger, showing a good agreement between the analytical and numerical approach.

Fitting Volume

Due to the very low LBE velocity (less than 0.1 m/s) inside the fitting volume, the contribution of this component to the overall pressure drop has been neglected.

Riser

Due to the gas injected to promote the LBE circulation during the tests, a two phase flow develops along the riser. To evaluate the two phase pressure drop, equation (50) has to be rewritten as follows [18] (neglecting the singular pressure drop term):

$$K_{eff,r} = \left(\Phi_{lo}^2 f_{lo} \frac{H_r}{D_{h,r}} \right) \frac{\rho_{eff}}{\rho_{l,r}} \frac{A_{eff}^2}{A_r^2} \frac{\dot{M}_m^2}{\dot{M}^2} \tag{55}$$

$\dot{M}_m$ indicates the mixture flow rate along the riser. f_{lo} is the Darcy-Weisbach friction factor evaluated considering a "*liquid only*" single phase at the same flow rate of mixture; $\rho_{l,r}$ is the density of the liquid in the mixture. Φ_{lo}^2 is the two phase factor multiplier.

According to the Lockart-Martinelli approach [22], the two phase factor multiplier can be expressed as:

$$\Phi_{lo}^2 = \left[1 + \frac{C}{X} + \frac{1}{X^2} \right] (1-x)^{1.8} \tag{56}$$

where C is a constant equal to 20 when both phases are turbulent.

X^2 is the Lockart-Martinelli parameter defined as:

$$X^2 = \frac{\text{friction pressure gradient in the liquid phase}}{\text{friction pressure gradient in the gas phase}} = \frac{(dp/dz)_{frict,l}}{(dp/dz)_{frict,g}} \tag{57}$$

and it can be evaluated applying the next equation:

$$X^2 = \left(\frac{\bar{\rho}_g}{\rho_l}\right)\left(\frac{1-x}{x}\right)^{1.8}\left(\frac{\mu_l}{\mu_g}\right)^{0.2} \tag{58}$$

being x the flow quality:

$$x = \frac{\dot{M}_g}{\dot{M}_m} = \frac{\dot{M}_g}{\dot{M}_g + \dot{M}_l} \tag{59}$$

Because the Argon flow rate foreseen to be utilized during the tests is in the range of 1-10 Nl/s (about 0.002-0.02 kg/s), it is possible to assume that:

$$x = \frac{\dot{M}_g}{\dot{M}_m} \approx \frac{\dot{M}_g}{\dot{M}_l} = (3 \div 30)10^{-5}$$

$$\dot{M}_m \approx \dot{M}_l = \dot{M}$$

Moreover, because

$$\bar{\rho}_g = 2.5 \text{ kg/s} \qquad \rho_{l,r} = \rho_{eff} = 10271.2 \text{ kg/m}^3$$

$$\mu_g = 5.4E-5 \text{ Pa s} \qquad \mu_l = 1.7E-3 \text{ Pa s}$$

From equation (58), it is possible to get the value of X^2 and as consequence, from equation (56), the two phase factor multiplier is evaluated to:

$$\Phi_{lo}^2 = (1.1 \div 1.7) \tag{60}$$

respectively for a gas flow rate in the range of $(1.0 \div 10)\ Nl/s$.

To evaluate the "*liquid only*" friction factor f_{lo}, the Churchill correlation (see equation (53)) has been adopted. In that equation, Re is substituted with Re_{lo}, that is the Reynolds number obtained considering a single phase flow rate equal to the mixture one. So, considering that

$$D_{h,r} = 202 \text{ mm} \qquad A_r = 32047 \text{ mm}^2 \qquad H_r = 3800 \text{ mm}$$

it is possible to get:

$$\mathrm{Re}_{lo} = \frac{\dot{M}_m D_{h,r}}{\mu_l A_r} \approx \frac{\dot{M} D_{h,r}}{\mu_l A_r} = 2.1E+5$$

and

$$f_{lo} = 0.017$$

Finally, from equation (55) (considering the maximum estimated value of 1.7 for the two phase factor multiplier):

$$K_{eff,r} = 0.02$$

having the ratio $A_{eff}^2 / A_r^2 = 0.04$.

Separator

Due to the very low LBE velocity (less than 0.1 m/s) inside the separator, the contribution of this component to the overall pressure drop has been neglected.

Heat Exchanger

The flow area, hydraulic diameter and length foreseen for the HX primary side (shell-side), as reported in the next paragraph, are:

$$D_{shell} = 342.3 \text{ mm} \qquad A_{shell} = 92024.55 \text{ mm}^2 \qquad L_{shell} = 3.205 \text{ m}$$

$$N_{tube} = 91 \qquad D_{h,tube} = 25.4 \text{ mm}$$

$$\overline{w}_{LBE,shell} = 0.12 \text{ m/s} \qquad \text{Re}_{shell} = 1.6E+04$$

Applying the Churchill Correlation to the HX (see equation (53)), it is possible to obtain:

$$A = 5.45E+19 \qquad B = 7.34E+05$$

and so:

$$f_{HX} = 0.027$$

Along the Heat Exchanger, no singular pressure drop are placed; so, for the HX the following assumption will be made:

$$\sum_l k_{HX,l} = 0$$

Finally, because the LBE average temperature along the HX is the same as the reference one and $A_{HX} = 45914.1\ mm^2$, it is possible to write:

$$\frac{\rho_{eff}}{\rho_{LBE,HX}} = 1 \qquad \frac{A_{eff}^2}{A_{HX}^2} = 0.02 \qquad f_{HX}\frac{L_{HX}}{D_{h,HX}} = 4.0$$

and:

$$K_{eff,HS} = \left(f_{HX}\frac{L_{HX}}{D_{h,HX}} \right) \frac{\rho_{eff}}{\rho_{LBE,HX}} \frac{A_{eff}^2}{A_{HX}^2} = 0.07$$

At this point, it is possible to evaluate the *effective* pressure drop coefficient as sum of the former contributions:

$$K_{eff} = K_{eff,IFC} + K_{eff,FC} + K_{eff,FM} + K_{eff,HS} + K_{eff,IHW} + K_{eff,LGA} + 3K_{eff,SG} + K_{eff,r} + K_{eff,HX} = 8.38$$

and therefore, the overall pressure drop along the flow path can be estimated applying equations (49):

$$\Delta p_{fric} = \frac{1}{2}\frac{\dot{M}^2}{\rho_{eff} A_{eff}^2} K_{eff} = 34.2\ \text{kPa} \tag{61}$$

As it is possible to note, the HS contribution is about 70% of the overall pressure drop (considering also the spacer grids and the lower grid assembly).

So, as shown, a pitch to diameter ratio of 1.8 allows to have a overall pressure drop along the flow path of 34 kPa, and the integral tests can be performed adopting the gas lift pumping system, already available, without mechanical pump installation.

Moreover, the P/D ratio value selected for ICE activity not compromise the implementation of the integral test, allowing to accomplish the goals listed above.

2.5 Heat Exchanger

For the ICE activity the cold sink consist of a cooling water circuit, a LBE-low pressure boiling water shell heat exchanger, interconnecting piping, and steam vent piping to discharge steam into the atmosphere.

In particular, the HX is made of 91 bayonet tubes. The bayonet consists of three concentric tubes (see figure 25), the outer two of which have the bottom end sealed. The water flow downward in the inner pipes, and then upward in the annulus between the inner and intermediate pipes. In the annulus vaporization takes place.

The annulus between the middle and outer pipes is filled by pressurized helium (4.5 bar). All annuli are interconnected to form a common gas plenum, the pressure of which is continuously monitored. A leakage from either walls of any of the outer tubes is promptly detected because of depressurization of the common helium gas plenum. The two outer tubes are mechanically and thermically decoupled. This configuration allows to localize the most part of the thermal gradient, between lead and boiling water across the gas layer, avoiding both risk of lead freezing and excessive thermal stresses across the tube walls during steady state operation and transients.

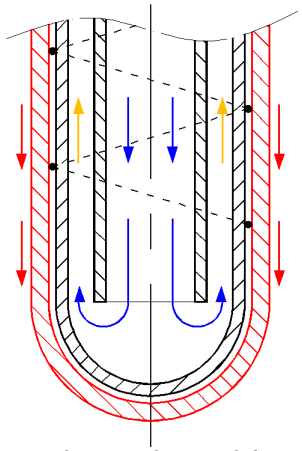

Figure 25: Sketch of the Bayonet tubes adopted for the ICE heat exchanger (in red LBE, blue water, yellow water-steam mixture)

In figure 26 is reported a picture of the HX when installed into the ICE test section. From the picture it is possible to see the shell and the lower grid where the bayonet tubes are constrained. In figure 27 the mechanical drawing of the het exchanger bayonet tubes is reported.

Figure 26: View of the ICE HX installed into the test section.

As already mentioned, the HX has been designed for a thermal duty of 800 kW. In the following the main parameters characterizing the heat exchanger are listed:

- Bayonet assembly: hexagonal lattice
- Number of bayonet tubes: 91
- Pitch of the bayonet tubes: 31 mm
- Shell I.D.: 342.3 mm
- Shell Length: 3205 mm
- Inner pipe O.D./thickness: 12.70 / 3.10 mm
- Middle pipe O.D./thickness: 19.05 / 2.11 mm
- Outer pipe O.D./thickness: 25.40 / 2.11 mm
- Bayonet active length: 3462 mm
- Helium gap thickness: 1.06 mm
- Helium pressure (20℃): 4.5 bar
- Working fluid shell side: LBE
- Secondary fluid (tube side): demineralised low-pressure water
- LBE inlet temperature: 400℃
- LBE outlet temperature: 300℃
- Water inlet temperature/pressure: 20℃ / 3.5 bar
- Steam outlet temperature /discharge pressure: 100℃ / 1 bar
- Water nominal flow rate: 0.6 kg/s
- Steam quality: 45%

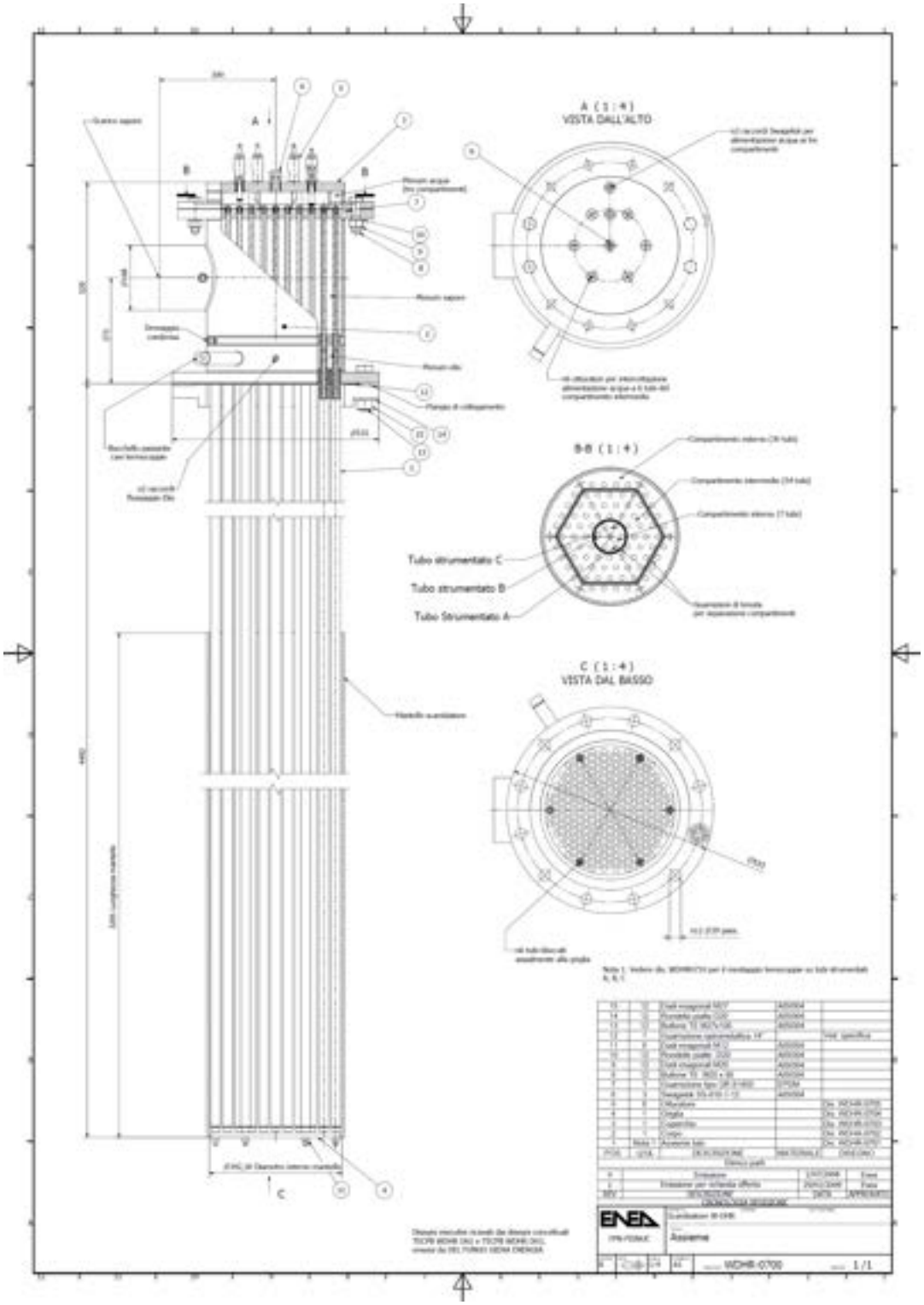

Figure 27: Mechanical drawing of the ICE's heat exchanger bayonet tubes.

2.6 Chemistry control and Monitoring System

For the operation of a HLM nuclear system, at least three requirements have to be taken into account for the design of a coolant chemistry control and monitoring system [17]:

1. Lead oxide (PbO) contamination has to be avoided during the service lifetime of the system. Its excess results in a blocking of the flow area and deposits formation on the structure, compromising the hydrodynamic stability of the flow path and reducing the overall heat transfer capacity.
2. Corrosion and dissolution have to be reduced as practicable as possible to ensure sufficient resistance for the structural materials. To this end, an active oxygen control is required to promote and maintain a protective film on the materials, although other method are under investigation.
3. Activation due to corrosion, spallation and fission products requires an appropriate chemistry control system to ensure safe management during the operation and maintenance phase.

The achievement of the above mentioned requirements makes chemistry control an essential element of nuclear system operation and maintenance.

From the experimental point of view, in particular in the field of HLM thermal-hydraulic, control of oxygen allows to achieve the control and monitoring of the lead oxide contamination and the corrosion rate during the lifetime of the facility.

In any case, for an experimental facility like CIRCE, as well as for a nuclear power plant, the main contribution of the contamination arises during the initial operations (first filling, start-up).

During the initial operations, it is critical to ensure that the LBE is kept clean and no solid oxides are formed. These deposits are composed of mainly PbO and LBE, with traces of iron, and are not affected by high temperature or by low oxygen concentration.

Such occurrence of two phase flow is not acceptable. So, the contamination must first be reduced to the minimum, and moreover, systems for regular purification have to be installed.

For the ICE activity, an oxygen control and monitoring system has been installed in the test section. The system has been designed in collaboration between ENEA and IPPE [24].

2.6.1 OXYGEN CONTROL SYSTEM

For the CIRCE facility (as well as for a nuclear plant) oxygen comes from the start-up operations, from the maintenance phases or from an incidental contamination. After any of these normal or accidental operations, an oxygen purification is required.

In consequence, the oxygen control system has to be designed defining:

- the upper limit for the oxygen concentration to avoid the contamination by coolant oxides;
- the lower limit for the oxygen concentration to enhance the corrosion protection by a self-healing oxide layer;

and it has to allow the:

- purification from oxygen during start-up or restart to prevent the formation of lead oxide;
- active oxygen control for corrosion protection during the normal operating mode, and, at the initial stage, to promote the formation of a protective oxide layer.

Therefore, normal operation of the systems with lead or lead alloys are possible if the oxygen content (activity) is maintained within a strictly specified range of values.

If this condition is fulfilled, the intensity of the mass transfer is minimal.

Upper limit for the oxygen for operational control

The coolant contamination by its oxides is defined by the solubility of oxygen in lead alloys, giving a maximum allowable oxygen chemical activity in the liquid metal. Adopting the following parameters:

- C_O dissolved oxygen concentration in the coolant [wt%];

- a_O oxygen thermodynamic activity [-].

The relation between these parameters is:

$$a_0 = \frac{C_O}{C_O^S} \tag{62}$$

where C_O^S is the saturated oxygen concentration of the coolant. The oxygen activity shall be equal to unity when saturation is reached.

For the saturated concentrations in the melt the following correlation can be adopted for LBE [24]:

$$\log C_O^S = 1.18 - \frac{3400}{T_{(K)}} \tag{63}$$

The operating specification to avoid any oxide precipitation in the coolant is then:

$$a_0 = \frac{C_O}{C_O^S} \leq 1 \tag{64}$$

and it must be ensured for all operating temperature in any point of the system, both in the liquid bulk as well as at the wall interface

Table 4 reports some values for the oxygen solubility in LBE at relevant temperatures for ICE operation.

	130°C	200°C	330°C	400°C	500°C	600°C	700°C
C_O^S in LBE	0.0006	0.01	0.35	1.34	6.0	19	48

Table 4. Oxygen solubility in lead alloys expressed in ppm (1 ppm = 10^{-4} wt%)

Considering that the minimum temperature of the surface of the ICE system is about 300°C, the upper oxygen limit for ICE operation is about 0.1 ppm.

Lower Limit for oxygen for operational control

Almost all of the elements of significance for structural material development have a lower equilibrium oxygen partial pressure than liquid lead and bismuth for their oxides. It is therefore possible to promote a protective oxide film by ensuring that the oxygen potential in the liquid metal is above the potential for film formation on the structural material.

This active oxygen control scheme for corrosion protection has been widely studied for steel structures an results in the formation of an iron-oxide film (magnetite Fe_3O_4) [17].

The reliance of an oxide film based on an alloying element of the structure requires that the oxygen potential is controlled within a narrow band, the upper oxygen potential being defined by the contamination by lead oxide, and the lower oxygen potential by the conditions of formation of the protective oxide.

Then, the lower oxygen limit is determined by the relative thermodynamic stability of the iron oxide when compared to the lead oxide

For the iron-based alloys and corrosion protection by self-healing oxide layer, the oxygen potential must ensure the conditions for the formation of iron oxide.

Because the magnetite is the less stable oxide of the layer, it defines the minimum allowable oxygen concentration.

The reaction of the steel oxidation in liquid lead alloys is assumed to be:

$$\frac{3}{4}Fe_{(dissolved)} + PbO_{(dissolved)} \rightarrow \frac{1}{4}Fe_3O_4 + Pb_{(liquid)} \tag{65}$$

where oxygen is supposed in solution in the form of dissolved lead oxide under its saturation limit.

Iron solubility (expressed in wt%) in LBE is expressed as [17] :

$$\log C_{Fe}^{S} = 2.01 - \frac{4380}{T_{(K)}} \tag{66}$$

Table 5 reports some values for the iron solubility in LBE at relevant temperatures for ICE operation.

	130°C	200°C	330°C	400°C	500°C	600°C	700°C
C_{Fe}^{S} in LBE	1E-5	0.0006	0.07	0.3	2.21	10	32

Table 5 . Iron solubility in LBE expressed in ppm (1 ppm = 10^{-4} wt%)

Iron activity in lead alloys is defined similarly to oxygen activity:

$$a_{Fe} = \frac{C_{Fe}}{C_{Fe}^{S}} \tag{67}$$

Lead activity in pure lead solution is equal to unity, while in LBE is defined as [17] :

$$\ln a_{Pb} = -\frac{135.21}{T_{(K)}} - 0.8598 \tag{68}$$

which is slightly lower than 0.45

Referring to the chemical activity of the dissolved oxygen with respect to the dissolved PbO activity (see eq. (65)), the minimum oxygen concentration required for the effective corrosion protection (measured in wt%) in LBE is expressed by the following relations [17]:

$$\log C_{O}^{\min} = -\frac{3}{4}\log C_{Fe} + 1.2375 - \frac{9757}{T_{(K)}} \tag{69}$$

From the previous equation, it is clear that the minimum oxygen concentration required depends on the iron concentration in the melt; during the transient, when the oxide layer is dissolving or growing, the only measurement of the oxygen content is not enough. The only way to detect if the oxide layer is changing its thickness is a direct measurement by an electrical resistance probe.

By the way, assuming that iron is present in saturated condition in the melt, the lower limit for the oxygen concentration is defined by the point where the magnetite will be dissolved first: the surface of the hottest point, due to the thermal gradient between wall and liquid bulk.

For the ICE activity, the maximum temperature foreseen on the pin wall is about 600°C (under natural circulation), and the lower oxygen limit to ensure the iron oxide formation would be about 0.0002 ppm.

Specification for active oxygen control

The oxygen concentration areas for operation to ensure both no contamination and corrosion protection by self-healing oxide layer are defined by:

$$C_O^{\min} \le C_O \le C_O^S \tag{70}$$

As illustrated in figure 28, for a non isothermal system operating between 300°C and 600°C (the minimum and maximum wall temperatures foreseen in the ICE activity) the intersection of the two ranges defined by the vertical lines plotted respectively for the cold and hot temperatures defines the oxygen range. As has been just established, the oxygen range allowable for ICE activity is 0.0002-0.1 ppm.

The assumption made above, that iron is present in saturated condition in the melt (see eq. (69)), is foreseeable in static condition, but unlikely in dynamic systems where mass transfer will play an important role. In fact, the iron will be released from the hot structural wall by corrosion, and transferred to locations with lower temperature, where it may precipitate; the effect of this dynamic equilibrium is the presence of not saturated regions in the system.

Decreasing the iron concentration reduces the oxidation area; because it is difficult to measure the iron concentration in the melt, and in any case impossible to monitor on-line, the oxygen specification should be set at the highest possible value that complies with the contamination requirement, which corresponds to the coldest interface temperature in the system.

For the ICE activity, the oxygen concentration specification chosen should be in the range 0.01÷0.1 ppm.

So, as already mentioned, the first requirement for the design of the ICE oxygen control system is to ensure that the contamination in any part of the plant, and for any operating condition, is avoided, especially during the initial operations.

Therefore, it is necessary to provide the following systems for the oxygen control:

- oxygen measurement systems for on-line monitoring for the cover gas and liquid metal;

- oxygen control system for purification, and possibly for active oxygen control;

For the oxygen measurement in cover gas, commercial devices are available, while for the measurement in LBE, an appropriate oxygen sensor will be installed in the ICE test section, developed in collaboration between ENEA and IPPE.

The oxygen control system implemented in CIRCE is based on the gas phase control.

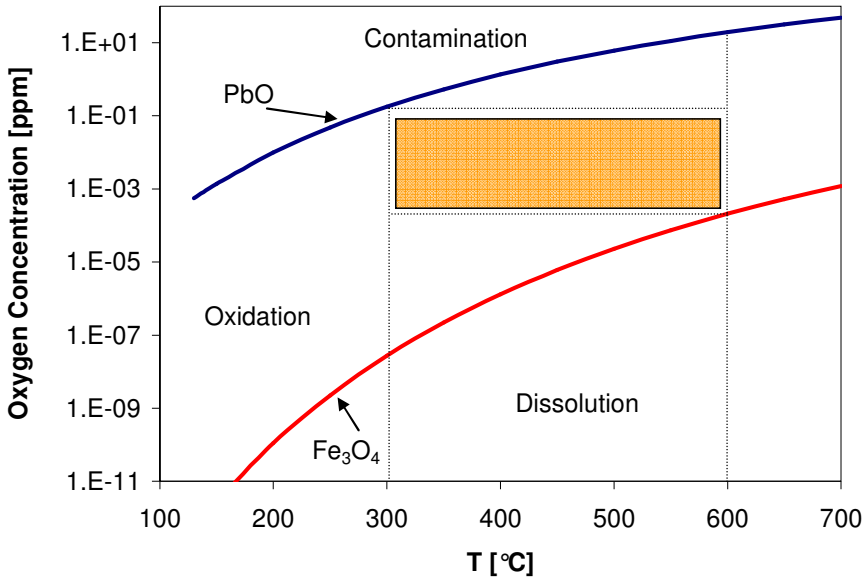

Figure 28 . Allowable oxygen operating range for the ICE activity

The gas phase control is based on gas/liquid equilibrium between the cover gas and the liquid bulk when the liquid is below saturation. Controlling the oxygen partial pressure in the gas phase, the dissolved oxygen content is set.

Practically, pure oxygen or hydrogen are flowed in the cover gas, in dilution with argon, in order to oxide or reduce the liquid lead alloys according to the following reaction:

$$Pb_{(liquid)} + O_{2(gas)} \Leftrightarrow PbO_{(dissolved)} \quad (71)$$

$$PbO_{(dissolved)} + H_{2(gas)} \Leftrightarrow Pb_{(liquid)} + H_2O \quad (72)$$

The reactions (71) and (72) take place through the interface between the cover gas and the liquid bulk.

The use of hydrogen allows to reduce the oxides accumulation in the system after a large contamination, restoring the thermal-hydraulic performance of the plant. Moreover, the reactions reported above present the advantage of producing only gaseous undesirable reaction products, which are easy to evacuate.

The reactions (71) and (72) are driven by the mass exchange at the gas-liquid interface. To increase the exchange area the bubbling technique is adopted, that is, the hydrogen- oxygen- argon mixture is injected below the free level, inside the melt.

Moreover, another important parameter that drives the reactions reported above is the temperature: higher is the temperature, better is the efficiency of the solid lead oxide reduction.

2.6.2 INSTRUMENTATIONS AND DEVICE

The sensors available for the measurement of the oxygen concentration in LBE are based on ionic conduction properties of some solid electrolyte.

In particular, with zirconia based ceramic (yttria-stabilized zirconia or magnesia-stabilized zirconia), it is possible to realize an electrochemical cell assembly that allows the measurement of dissolved oxygen in liquid metal; this is know as the galvanic cell method.

This technique has several advantages such as:

- specific to dissolved oxygen; the bounded oxygen (such as in oxide) is not measured;
- on-line measurement;
- wide concentration range covered by one single sensor;
- accuracy is not related with the size and contact area of the electrodes;
- no disturbance on the system.

The main disadvantages are the high operating temperature and the poor thermal shock resistance due to the mechanical properties of the solid electrolyte.

The adopted sensors are based on the potential measurement method at null current for a galvanic cell with a solid electrolyte: zirconia doped with magnesia or

yttria, which stabilizes the ceramic tetragonal form that is oxygen ions conducting for a certain temperature and oxygen concentration, is adopted as solid electrolyte.

The solid electrolyte divides the HLM phase where the oxygen has to be measured from the reference electrode, that is a constant oxygen potential reference system.

At the moment, the sensors assembly are made by a one-end closed tube, allowing to separate the reference electrode (inside) from the working electrode (outside), as reported in figure 29.

For this kind of sensors, the choice of the reference electrode is a critical issue.

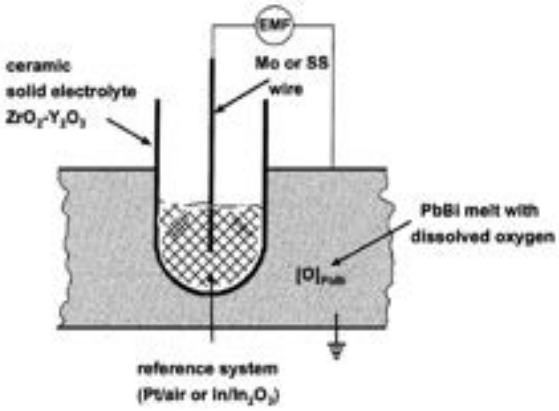

Figure 29. Schematic view of the electrochemical oxygen meter [25]

For the sensors mounted in CIRCE, the reference systems adopt low melting point liquid metal electrodes, such as Bi/Bi_2O_3 (Bi mp 271°C); the liquid metal reference systems provide a better contact with the solid electrolyte, and then a lower cell resistance, allowing to work at lower temperature. Mo is adopted as electrical wire due to its compatibility with In and Bi.

Therefore, a typical electrochemical galvanic cell, referred as EC sensor, can be indicated as follow:

$$Mo,\ Bi\,/\,Bi_2O_3(\text{reference})\ //\ ZrO_2+Y_2O_3\ //\ Pb\,/\,PbO,\ steel \tag{73}$$

As already mentioned, the yttria stabilized zirconia (YSZ) ceramic divided two media with different oxygen activity. Because YSZ conducts specifically oxygen ions, an electromotive force arises across the ceramic.

If one of the two media is a reference media, so that it maintains constant the oxygen partial pressure to a well know defined value, then the electromotive force E is a function of the partial pressure (or the activity) in the other medium.

The theoretical response of a EC sensor (73) can be written as follow:

$$E_{(mV)} = 119.8 - 0.0539 \cdot T_{(K)} - 0.0431 \cdot T_{(K)} \cdot \ln a_O \tag{74}$$

for $E > E_{sat}$, while under saturation condition:

$$E_{sat} = 119.8 - 0.0539 \cdot T_{(K)} \tag{75}$$

Similarly, the response of $E(T, a_o)$ can be written directly in the form $E(T, C_O)$, as follow:

$$E_{(mV)} = -218 + 0.462 \cdot T_{(K)} - 0.0431 \cdot T_{(K)} \cdot \ln C_{O(ppm)} \tag{76}$$

These relations allow to plot the theoretical E vs. T (C_O as parameter) diagram as illustrated in figure 30.

The diagram reports the oxygen iso-concentration lines, as well as the lead oxide saturation line and the magnetite stability lines for a unit iron activity, the iron oxide being stable below the line. For a lower iron activity, meaning for a concentration lower than its solubility, the threshold line for the magnetite dissolution will be lower.

Figure 30 is very useful to read the sensor response during the HLM system operation. In fact, it allows to compare the relative position of the oxygen with the PbO saturation line, defining the lower potential value achievable to avoid the contamination of the system by lead oxide precipitation.

Moreover, in the figure 30 the working area for the ICE activity is reported. In fact, as already mentioned for a non isothermal system operating between 300°C and 600°C (minimum and maximum wall temperature foreseen in the ICE activity), the intersection of the two ranges delimited by the vertical lines plotted respectively for the cold and hot temperatures defines the oxygen range.

The relations (74), (75) and (76) are theoretical equations describing the thermodynamic behaviour of the oxygen sensor.

Apart from the data used for the theoretical assessment, which are not well know, there are other reasons that involve a non theoretical behaviour of the sensors, such as [17] :

- electrolyte conduction properties (impurities dissolved in the ceramic);
- influence of the reaction at the electrode/electrolyte interface (liquid metal – zirconia interaction);
- cell irreversibility (equilibrium not reached due to an oxygen transfer limitation at very low oxygen partial pressure)
- instrumental and sensor assembling uncertainty.

For these reasons, a calibration of the sensors is mandatory. After calibration, the accuracy is about 5% of the voltage reading.

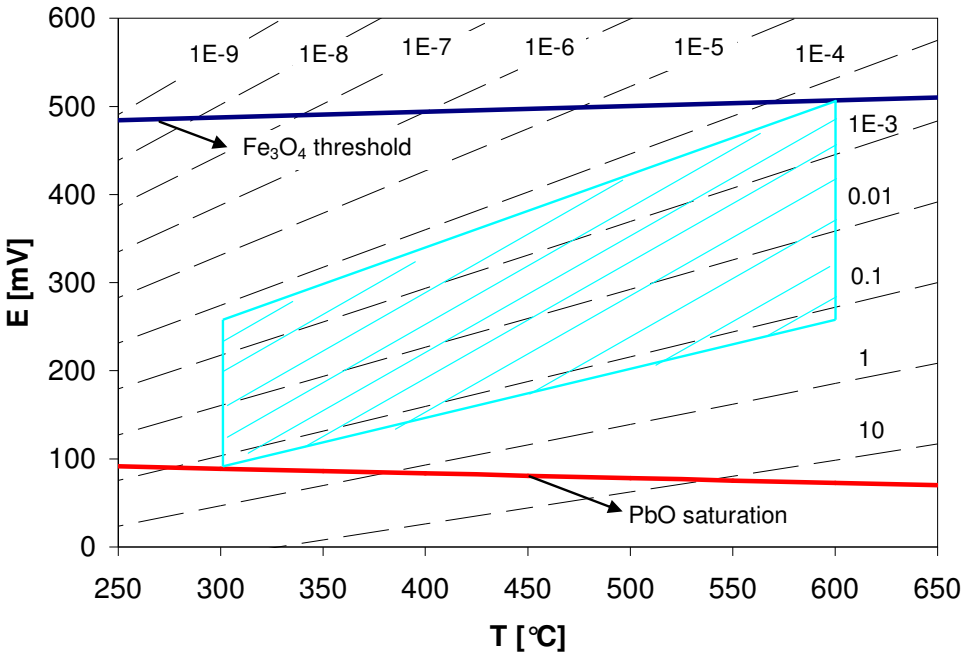

Figure 30. Diagram E vs. T for oxygen sensors reading in LBE

The ICE oxygen sensors [24], supplied by IPPE, are presented in figure 31.

The sensors have been calibrated by IPPE, and the following correlation has been carried out to express the electromotive force as function of the oxygen activity in the LBE:

$$E_{(mV)} = 0.088 - 1.78 \cdot 10^{-5} T_{(K)} - 9.907 \cdot 10^{-5} T_{(K)} \log a_0 \quad (77)$$

The performance of the sensors are reported in the table 6 .

Oxygen Activity Range, a_0, [-]	$1 \cdot 10^{-6}$ -1
Maximum Working Pressure [MPa]	0.5
Maximum HLM Flow Velocity [m/s]	1.0
Maximum Temperature Variation Rate [°C/s]	10
HLM working temperature [°C]	350-650
Relative Deviation from Nominal Static Characteristic (NSC), %	±10
Time required to achieve the operating conditions, [h]	10

Table 6 Technical Performance for the ICE Oxygen Sensor [24]

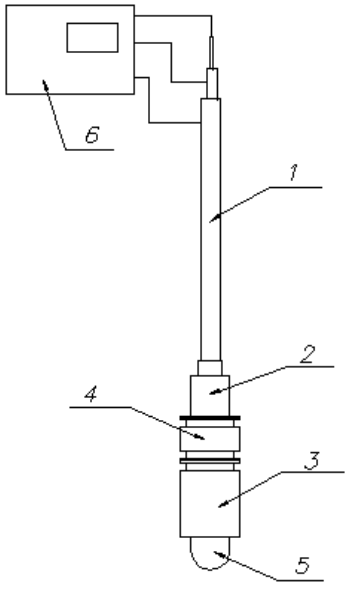

1 – two-shell potential terminal lead; 2 – sealed lead-in; 3 – metallic casing of ceramic sensitive element; 4 –adapter (transition part); 5 – ceramic sensitive element; 6 – measuring system

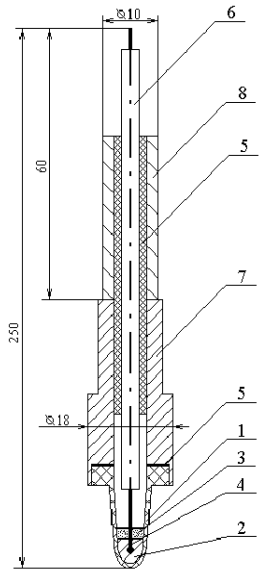

1 – Capsule Sensitive Element; 2- bismuth; 3 – bismuth oxide; 4 – electrode; 5 – glass ceramics; 6 – potential terminal; 7- casing; 8 – sealed lead-in.

Figure 31 View of the ICE oxygen sensors

It is finally mandatory to highlight that sensors give only the local oxygen content, so for oxygen control it is necessary to use at least three oxygen sensors. Sensors should be placed in zones with T_{max}, T_{min}, and T_{av}.

Presently, it is impossible to have an analytical relationship for the dissolved oxygen distribution in coolant for non-isothermal system. Therefore, the control of mass transfer and prediction of the thermodynamic situation in the system are impossible adopting a single oxygen sensor.

For this reason three oxygen sensors have been installed in the ICE test section, named S1, S2, S3.

S1 has been placed into the downcomer (see figures 2 ,3) , 2500 mm below the free level (average temperature), S2 has been placed into the Separator, 120 mm below the free level (highest temperature) and S3 placed again into the downcomer, 6000 mm below the free level (lowest temperature).

For the DEMETRA experimental campaign (see the next paragraph), has been pointed out that the oxygen sensors installed starts to work up to 350°C.

Anyway, the response of the sensors during the experimental run showed as the ICE working point falls inside the working area depicted in the figure 30, underlined that the contamination of the coolant by oxidation was avoid and the corrosion protection of the structural materials by self-healing oxide layer was enhanced.

3. DEMETRA EXPERIMENTAL CAMPAIGN

The experimental campaign carried out in CIRCE facility was planned for studying the behaviour of an HLM nuclear system primary system (XT-ADS and EFIT as reference) through integral testing. The experimental results demonstrate the availability of a multi-purpose test rig, i.e. CIRCE, which is suitable for supporting the design of HLM reactor components (e.g. pin and bundle configuration, main coolant pump, primary to secondary heat exchanger), for studying the thermal-hydraulics and safety issues of different reactor configurations. The experimental campaign is the starting point for developing an experimental database and for supporting the development of advanced computer codes.

Four tests were executed in CIRCE facility with installed ICE test section:

1. Test A (*characterization test*), which is aimed at characterizing the performances of the gas flow injection system for inducing the flow along the loop.
2. Test B (*characterization test*), which is devoted to evaluate the thermal-hydraulic performances of the circulation loop in nominal steady state conditions.
3. Test C (*transient test*) simulates the behaviour of the system during the unprotected loss of heat sink.
4. Test D (*transient test*) assesses the dynamic of the system during a loss of flow scenario focussed on the transition between the forced to natural circulation.

3.1 Test A: Isothermal Steady State Enhanced Circulation

The facility is filled with LBE at 300°C. The electrical heaters of the HS are switched off. The HX is not operated, i.e. no feed water flows through the secondary side of ICE test section. These conditions imply that the temperature of the LBE fluid remains uniform in the circuit and nearly constant during the overall transient (Figure 32).

The Test A is a “quasi” steady sate experiment, consisting in a stepwise increase of gas flow injection from about 1 to 9 Nl/s (see Figure 33).

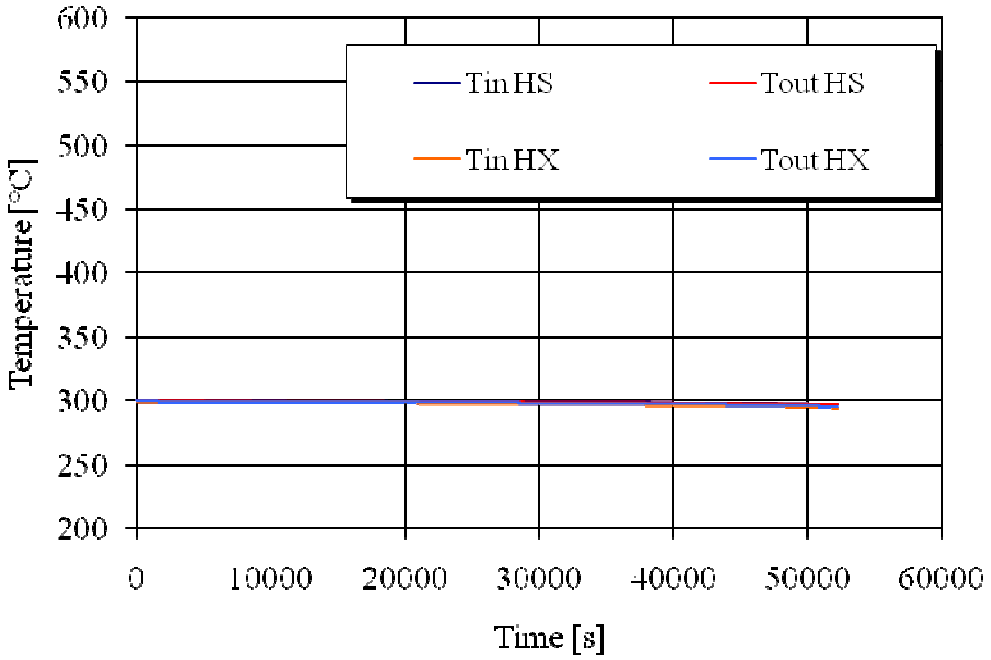

Figure 32. Test A: trend of the average inlet and outlet temperature along the HS and inlet and outlet temperature through the HX (LBE side).

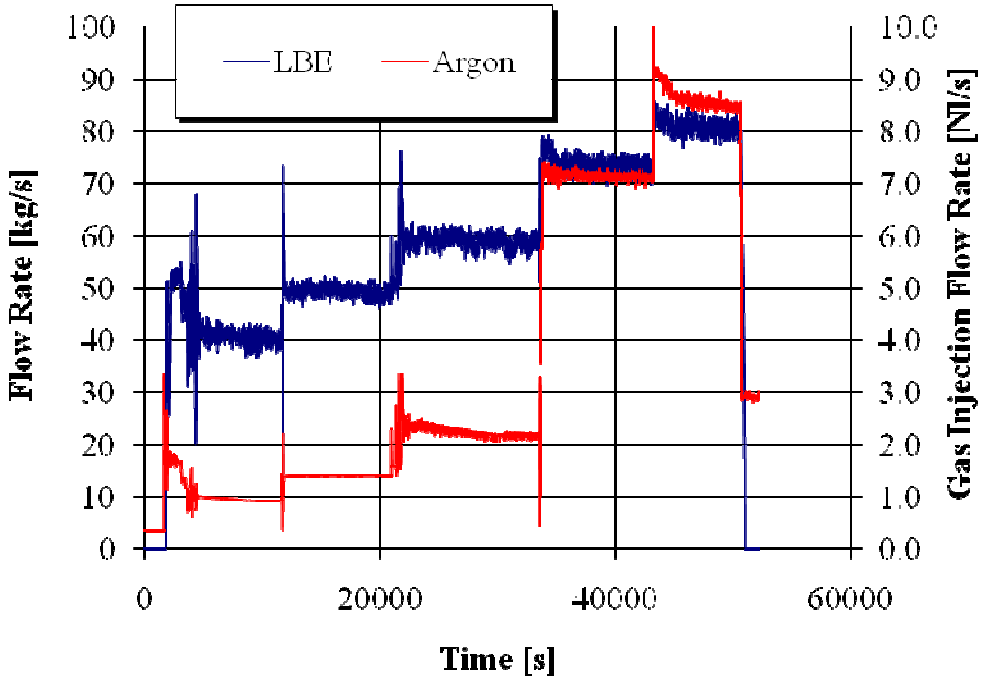

Figure 33. Test A: trend of the gas injection flow rate and the related LBE flow rate along the ICE test section.

The Argon injected in the riser provides the driving force for LBE flow circulation in primary loop. Five values of gas flow rate are tested in order to characterize the system and to verify its capability in achieving the design operating conditions planned in the ICE experimental campaign.

By means of the pressure difference measured in the riser, it is indirectly derived the values void fraction (see Figure 34). Indeed, as discussed in detail in [11], the estimation derives by assuming the friction and the acceleration terms of the measured pressure difference across the riser negligible when compared with the gravimetric term.

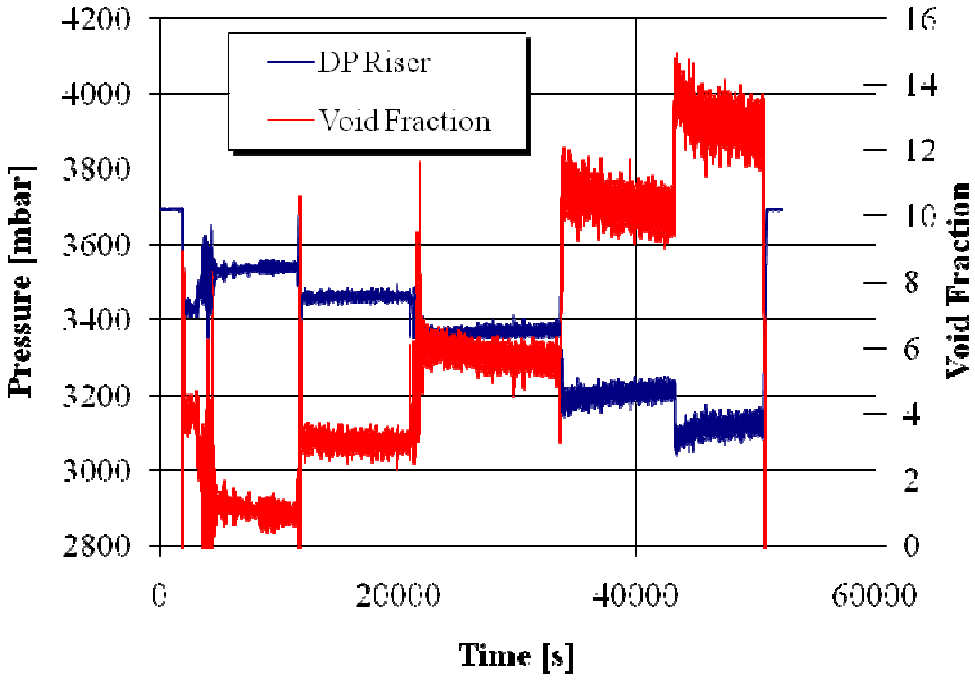

Figure 34. Test A: pressure difference measured along the riser and estimated average void fraction into the riser.

The driving force (in Figure 35) is evaluated as the pressure difference in the riser when the LBE fluid at rest minus the pressure difference measured during the transient.

Figure 36 reports the pressure drop across the spacer grids. This measure may be useful for setting up the energy loss coefficients of thermal-hydraulic system code modelling as well as for assessing CFD capabilities.

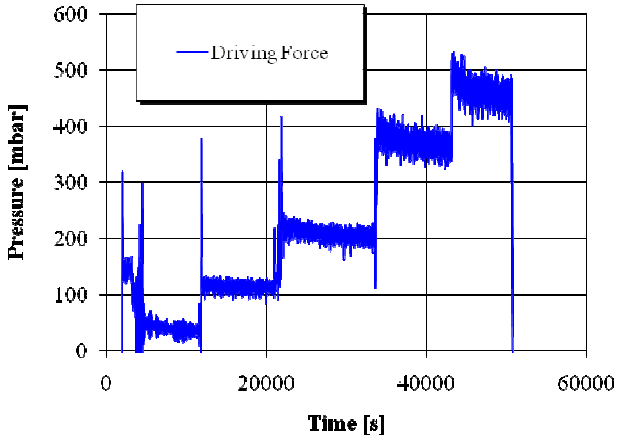

Figure 35. Test A: driving force available for the LBE circulation along the ICE flow path.

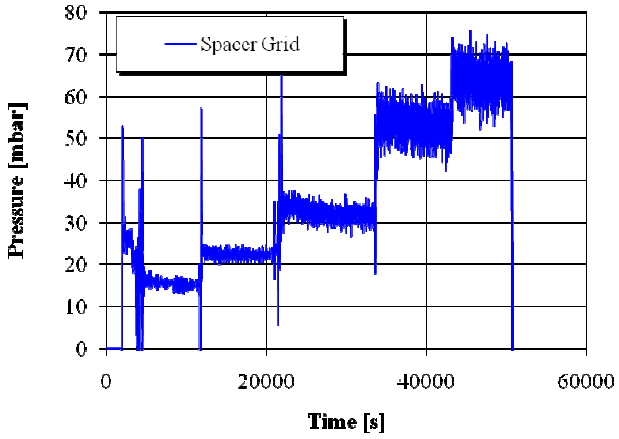

Figure 36. Test A: pressure difference measured across the spacer grids.

Finally, the LBE fluid velocities across the HS and the HX are depicted in Figure 37. The results of the test demonstrates the gas flow injection system is capable to accomplish the target value of average velocity equal to 1 m/s in the HS. This is the velocity considered representative for the XT-ADS and EFIT concepts. For sake of completeness the figure reports also the Re numbers calculated in the HS and HX: in the former case it results highly turbulent (i.e. larger than 1E+5).

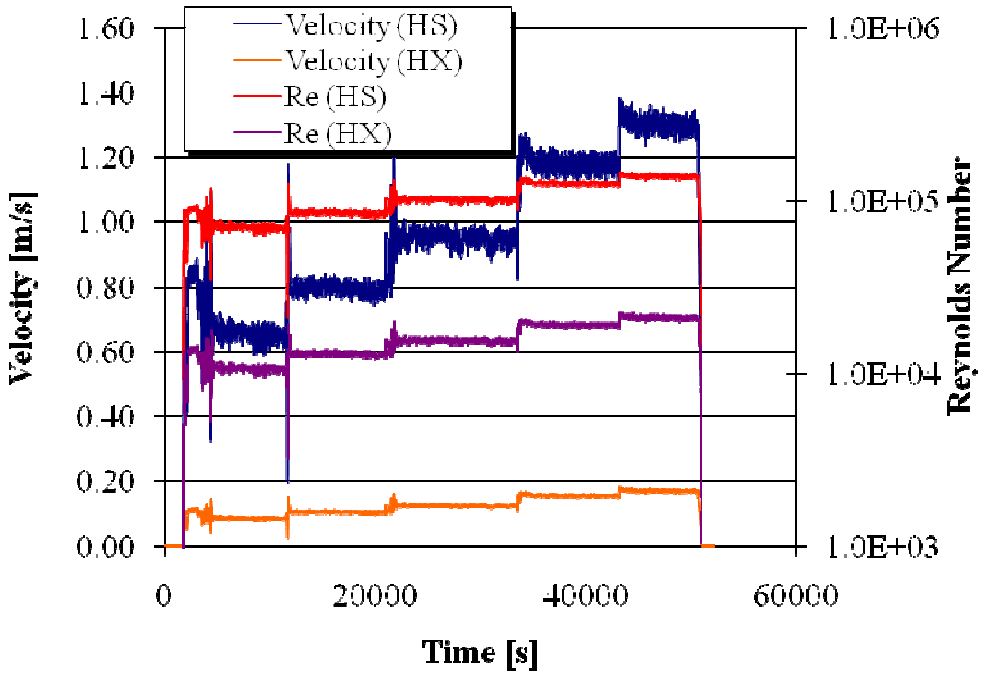

Figure 37. Test A: average LBE velocity through the rods bundle and bayonet tubes of the HX. Reynolds number inside the HS and HX (log. scale).

Table 7 provides the boundary conditions of Test A and characterization of the gas lift system.

#	Time span[s]	Argon flow rate* [Nl/s]	LBE flow rate* [kg/s]	Riser void fraction* [-]	LBE temperature* [°C]
0	0 – 1680	0.0	0	0.0	300
1	1680 – 11600	0.9	40	0.01	300
2	11600 – 20950	1.4	49	0.03	300
3	20950 – 33550	2.1 – 2.2	59	0.05	300
4	33550 – 43140	7.1 – 7.2	73 - 74	0.10	300
5	43140 – 50650	8.4 – 8.5	80 – 81	0.12	300

* The value is at the end of the time span when the system has achieved "quasi" steady state conditions.

Table 7. Test A: summary of the main parameters characterizing the transient.

3.2 Test B: Full Power Steady State Enhanced Circulation

The test B is a steady state full power gas enhanced circulation test.

The test started by the gas injection through the nozzle installed into the bottom of the riser, with an average flow rate of 1.7 Nl/s. After that a steady state flow rate has been obtained along the primary flow path, the power into the heat source is linearly increased up to 800 kW in 300 s. When the full power is reached, the heat exchanger is started supplying the cooling water into the manifold.

In figure 38 the trend of the argon flow rate injected into the riser, as well as the promoted primary flow rate through the heat source, is reported. As it can be noted, after about 100 sec from the onset of the gas injection, a liquid metal steady state flow rate of 60 kg/s is obtained, as foreseen in the test specifications.

In the figure 39 the trend of the supplied electrical power to the heat source is reported. As it can be noted, the supplied power is compared with the thermal power extracted by the heat source and the heat exchanger, showing a good agreement among them. Both the HS and HX removed power are calculated by a thermal balance on the LBE stream lines through the inlet and outlet section of the correspondingly components.

During the test, because argon is injected in the riser, the main driving force for fluid circulation in the pool results from void buoyancy in the riser. The driving force available during the test can be estimated measuring the pressure difference through the inlet and outlet section of the riser. In fact, under the static conditions, the pressure difference along the riser is due to the gravimetric head. During the test, when the circulation is promoted, the pressure difference along the riser is due to three contributes: gravimetric (calculated taking in account the average density of the argon-LBE mixture), acceleration and friction.

Because it has been evaluated that the acceleration and friction contributes are neglected if compared with the gravimetric one [11], the measurement of the pressure difference through the riser when the circulation is promoted, allow to make an estimation of the average density into the riser and so an estimation of the

average void fraction into the riser. This method is usually defined as manometric method.

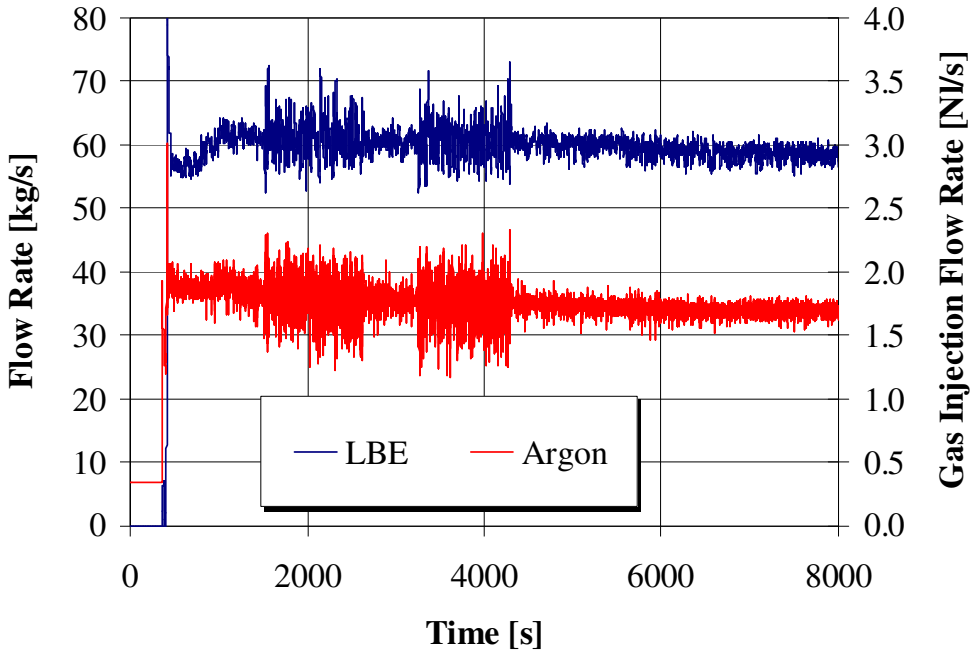

Figure 38. Test B: trend of the gas injection flow rate and the related LBE flow rate along the ICE test section

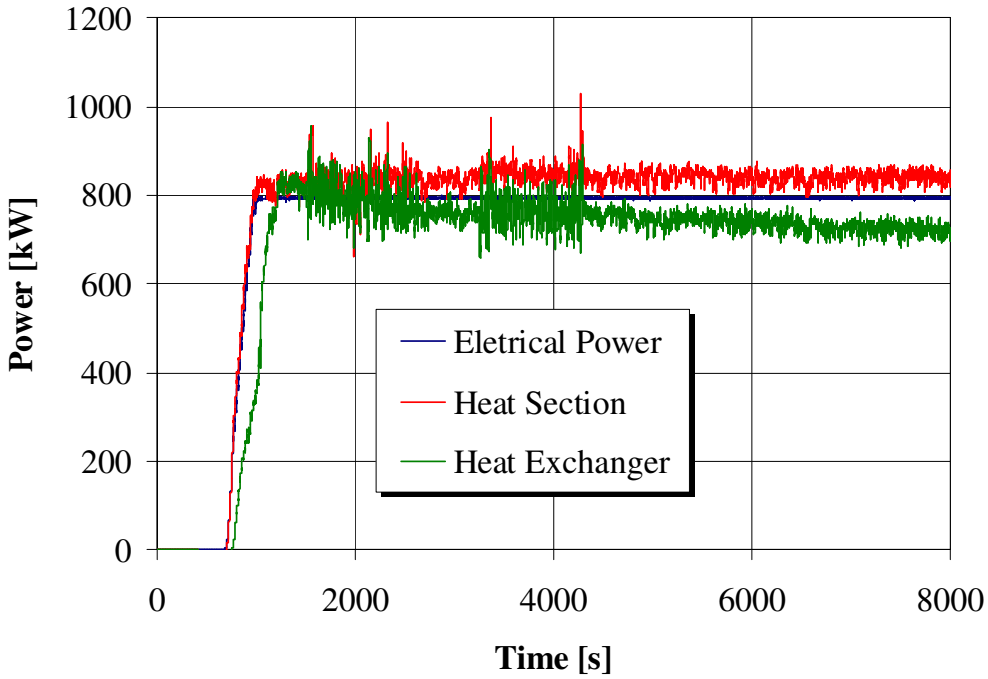

Figure 39. Test B: trend of supplied electrical power and the removed thermal power calculated along the heat source and heat exchanger

In figure 40 the trend of the pressure difference along the riser is depicted. As shown, by the gas injection the gravimetric head into the riser is reduced from 3700 mbar (static head) to 3400 mbar (dynamic head). Applying the manometric method above described, the average void fraction into the riser during the test is estimated to be about the 4%.

As consequence, it is possible to estimate the driving force available for the LBE circulation [11].

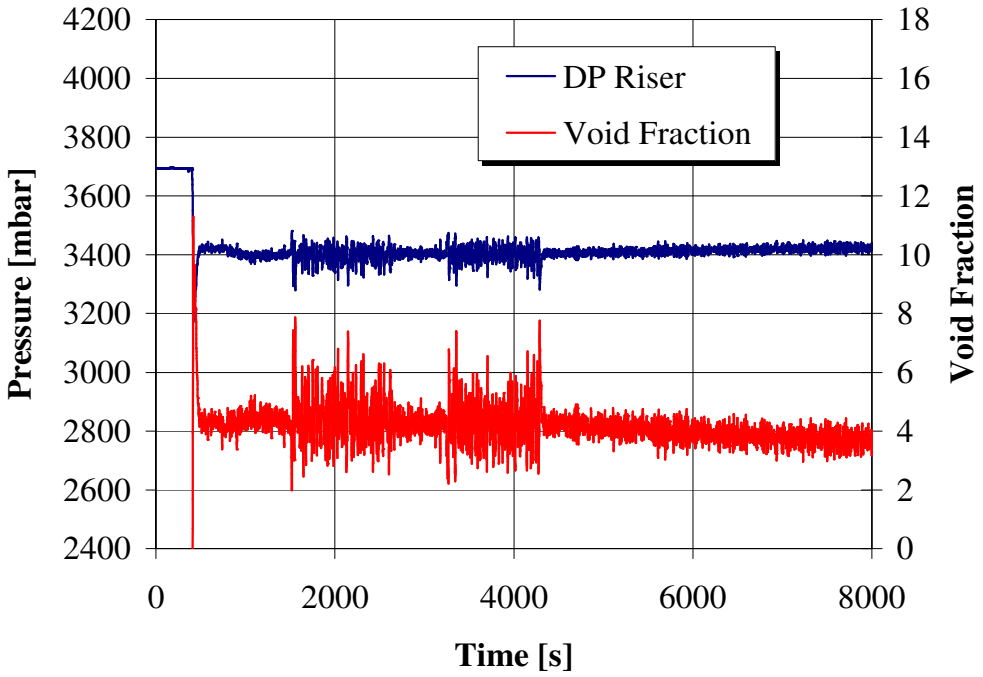

Figure 40. Test B: pressure difference measured along the riser during the test and estimated average void fraction into the riser

The results carried out are depicted in the figure 41, where the pressure head available for the LBE circulation is shown. The estimation takes in account not only the void buoyancy into the riser but also the thermal buoyancy into the heat section evaluated by the Boussinesq approximation [11].

As it can be noted, the driving force available is about 150 mbar. This value does not match well with the analytical estimation (around 342 mbar, equation (61)).

This discrepancy is probably due to the analytical approach adopted to estimate the pressure losses through the spacer grids as well as through the lower grid.

A well refined CFD calculations should be performed coupled with the experimental results here depicted, to better estimate the singular pressure drop coefficient related to these critical components.

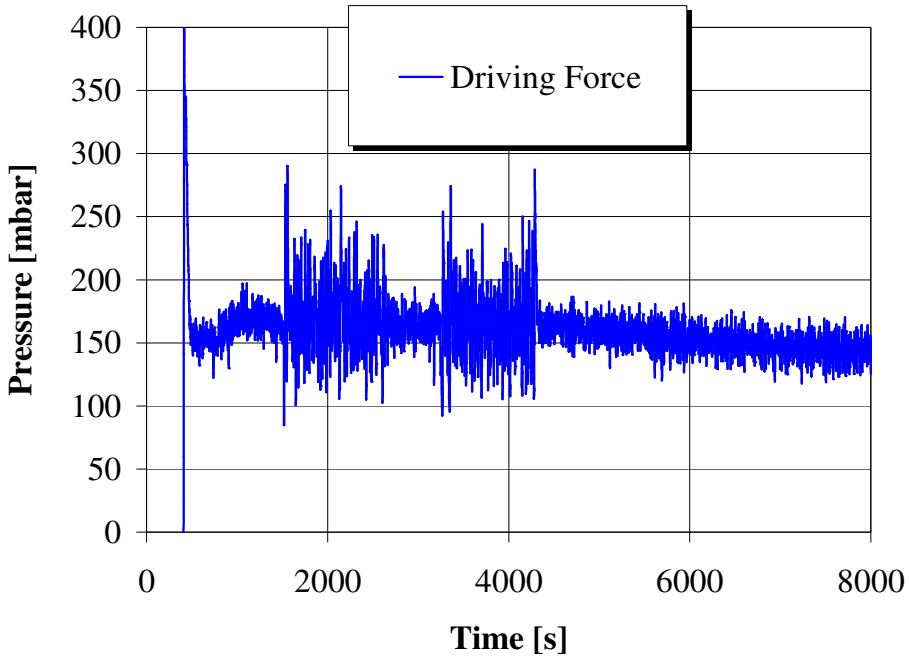

Figure 41. Test B: driving force available for the LBE circulation along the ICE flow path.

In the figure 42, the measured thermal difference through the heat section and heat exchanger (LBE side) is reported. As shown the difference falls around 100°C as foreseen by design.

At the inlet of the HS three thermocouples have been installed (TE001, TE002, TE003), placed at different depth into the rod bundle. As depicted in the figure 43 the temperature profile in the inlet section is really uniform.

The same it has been made at the outlet of the HS, installing three thermocouples (TE004, TE005, TE006) at different depth into the bundle. As shown in figure 43 at the outlet section the temperature fields is not so uniform, highlighting that a certain thermal gradient exist among the involved subchannels of the pin bundle.

Finally figure 43 underlines as the average temperature of the LBE during the full power test falls around 350°C, as required.

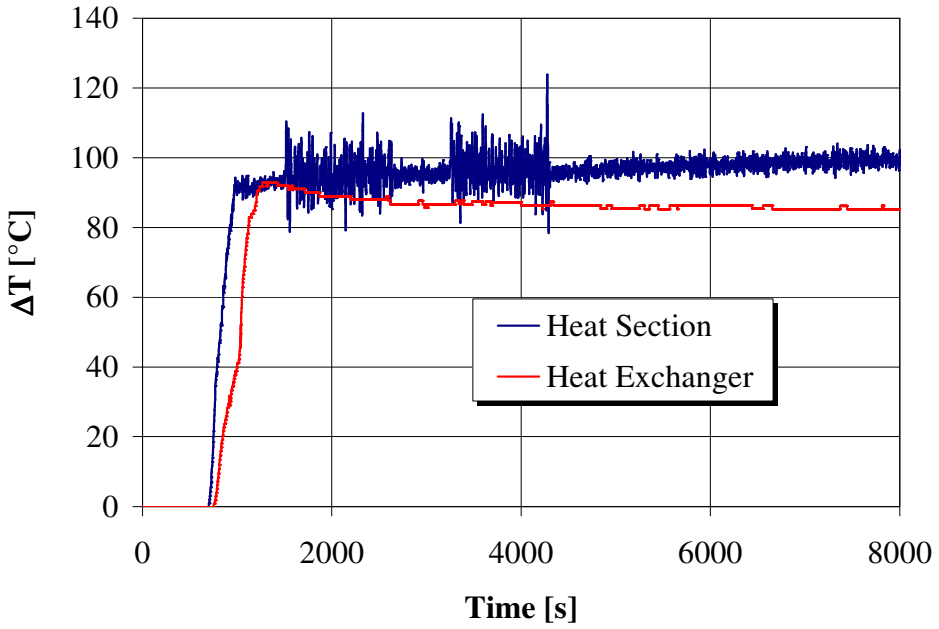

Figure 42. Test B: thermal Difference through the inlet and outlet section of the Heat Section and Heat Exchanger (LBE side).

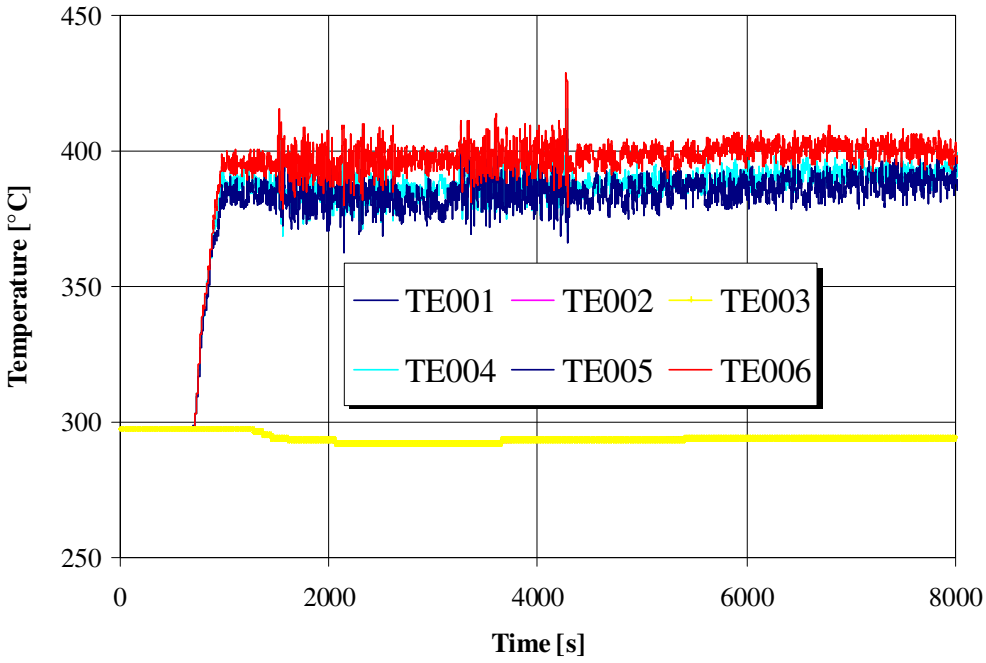

Figure 43. Test B: trend of the temperatures at the inlet (TE001, TE002, TE003) and outlet (TE004, TE005, TE006) of HS. The thermocouples have been installed, both in the inlet than in the outlet, at different depth into the pins bundle, to verify the uniformity of the temperature in the sections.

The average inlet and outlet temperature trends along the heating section, as well as the inlet and outlet temperature trends through the heat exchanger are shown in the figure 44.

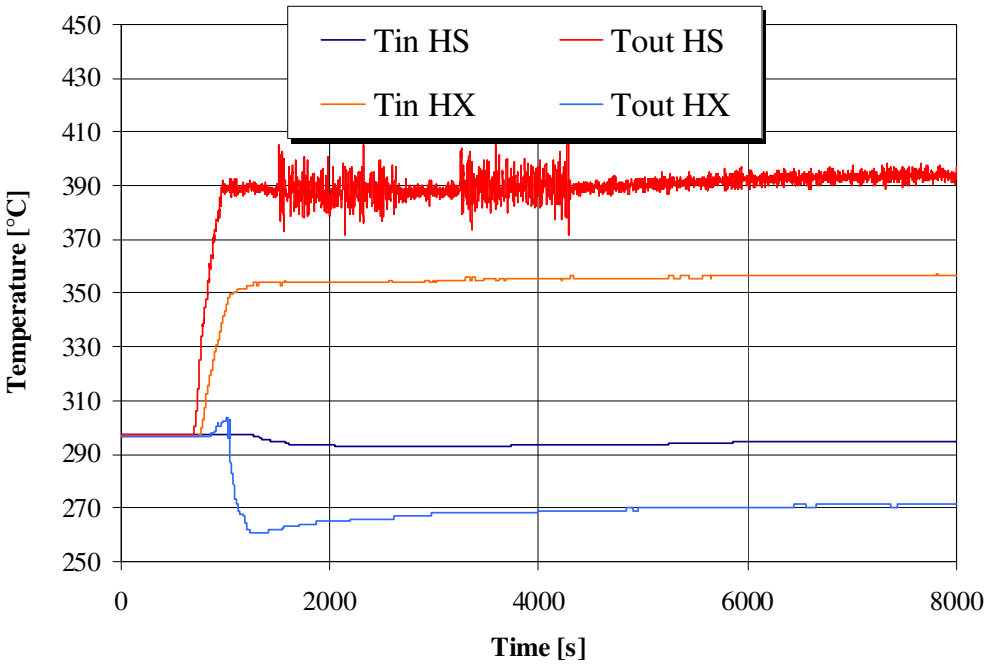

Figure 44. Test B: trend of the average inlet and outlet temperature along the HS and inlet and outlet temperature through the HX (LBE side).

For what concern the liquid metal velocity, one of the main specifications of the experiment was to have an average velocity through the HS of about 1 m/s, as foreseen for the XT-ADS and EFIT concepts.

The results carried out shown as also this commitment has been accomplished during the test, as depicted in figure 45. In the same figure the Reynolds number of the LBE stream line inside the rods bundle is reported, equal to 1.1E+5, underlines as the flow is highly turbulent, fully developed.

Again, in the same figure the LBE average velocity though the bayonets tubes of the Heat Exchanger is reported. As it can be noted, there the LBE velocity 80% lower than in the rods bundle (0.12 m/s). As consequence also the LBE stream line turbulence is lower, even if the flow remain turbulent being Reynolds equal to 1.8 E+4.

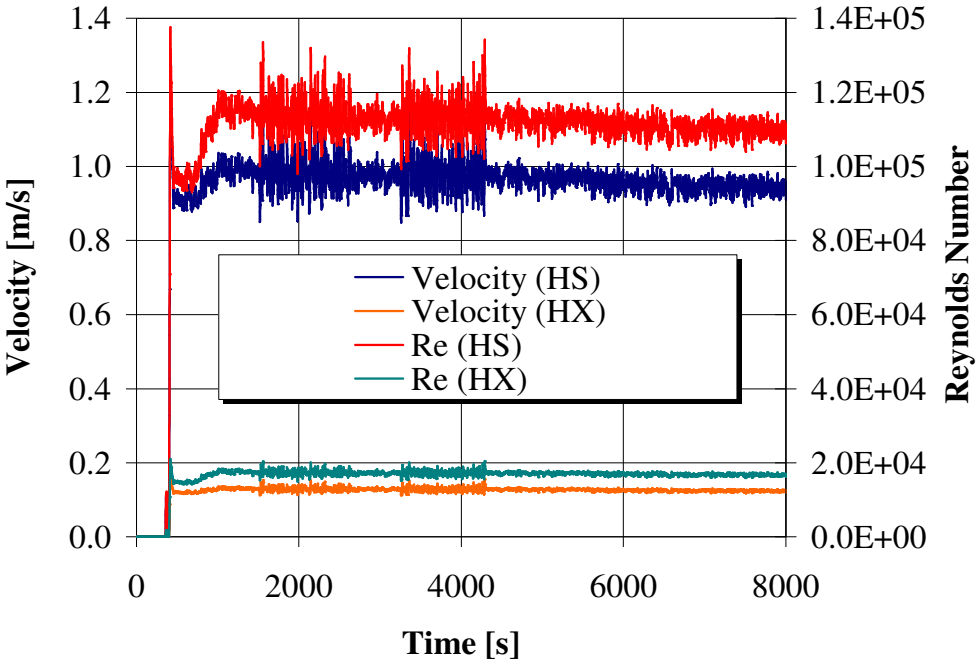

Figure 45. Test B: average LBE velocity through the rods bundle and bayonet tubes of the HX. Reynolds number for the liquid metal stream line inside the HS and HX. Full power test.

As can be noted between the Tout HS and Tin HX a certain difference exists (around 30℃), highlighting a thermal coupling between the fitting volume, riser and the downcomer.

The LBE flowing into the fitting volume and then in the riser losses thermal power towards the upper part of the downcomer where the HX is placed.

The same happens for what concern the Tout HX and Tin HS, underlines that the LBE flowing down from the HX is heated into the downcomer before to flow inside the heating section. A thermal coupling exists between the lower part of the downcomer and the test section.

For what concern the water side of the prototypical heat exchanger, as can be noted from the figure 46, for the run of the full power test a water flow rate of 0.57 kg/s has been supplied.

The measured pressure loss through the heat exchanger was 1.5 bar. In the figure 46 also an estimation of the steam quality is reported. The estimation has been made starting from the thermal power removed by the heat exchanger calculated on the liquid metal side.

As reported, an average steam quality of 45% is calculated, underlines that the discharged vapour in the atmosphere is not superheated.

The same can be observed also in the figure 47, where the inlet water temperature and outlet steam temperature is reported.

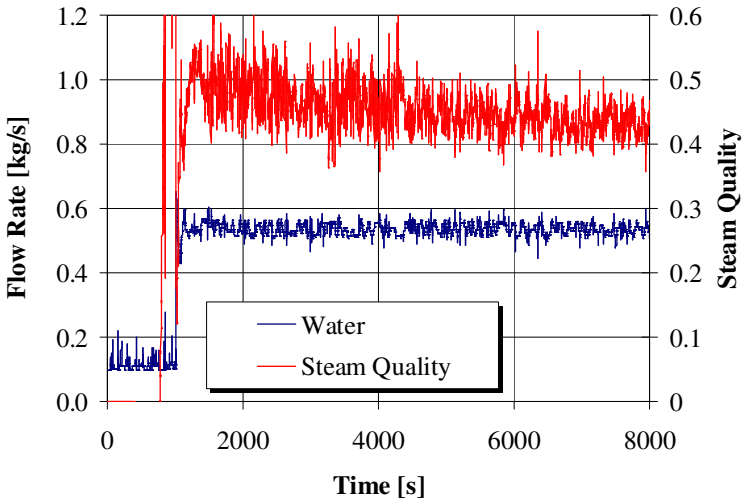

Figure 46. Test B: trend of the water flow rate supplied to the HX (test B).The steam quality trend is evaluated starting from the thermal power removed by the heat exchanger calculated on the LBE side.

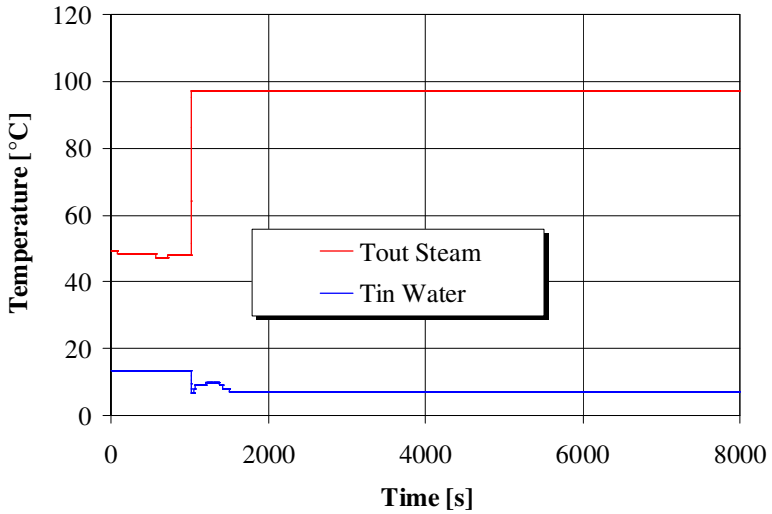

Figure 47. Test B: inlet and outlet water temperature trend inside the Heat Exchanger.

As reported above, the test B was successfully completed, as well as the test A.

After the preliminary analysis of the results carried out, also the transients foreseen for the test C and D will be run, allowing to achieve the goals indicated for the ICE activity.

3.3 Test C: Unprotected Loss of Cold Sink

Test C is a transient investigating the system behaviour following a postulated unprotected loss of heat sink. Three main phases are identified:

- from 0 s up to 11420 s: conditioning phase for achieving the reference initial conditions;
- from 11420 s up to 13560 s: occurrence of initiating event and investigation of the consequences, postulated accident phase;
- from 13560 s up to 34650 s: mitigation phase for bringing the test facility in safe conditions.

The test starts with the system in hot conditions at zero power . The primary coolant is stagnant and the temperature is uniform in the circuit.

The gas flow injection system is switched on at 575 s, with an average flow rate of 1.7 Nl/s. The resulting buoyancy force induces a flow circulation in the ICE loop corresponding roughly to 60 kg/s (Figure 48), according with the specifications.

The electrical power is supplied to the fuel bundle (Figure 49), thus the heated section provides the coolant with about 800 kW. At 960 s the valves upstream the HX are opened, in order to establish the energy balance in the system. Once the thermal balance between HS and HX is achieved the facility is operated in stationary conditions until 11420 when the initiating event occurs.

In these conditions, the void fraction is about 4% (indirect derivation) in the HS and the pressure difference across the riser is 3400 mbar (dynamic head), Figure 50.

The driving force, depicted in Figure 51, is slightly above 150 mbar. The LBE flow velocity is about 1 m/s (Figure 55), thus resulting turbulent both in the pin bundle (HS) and in through the bayonets tubes (HX), as well. The temperature difference between the inlet and outlet of the HS and HX is 100 °C (Figure 52).

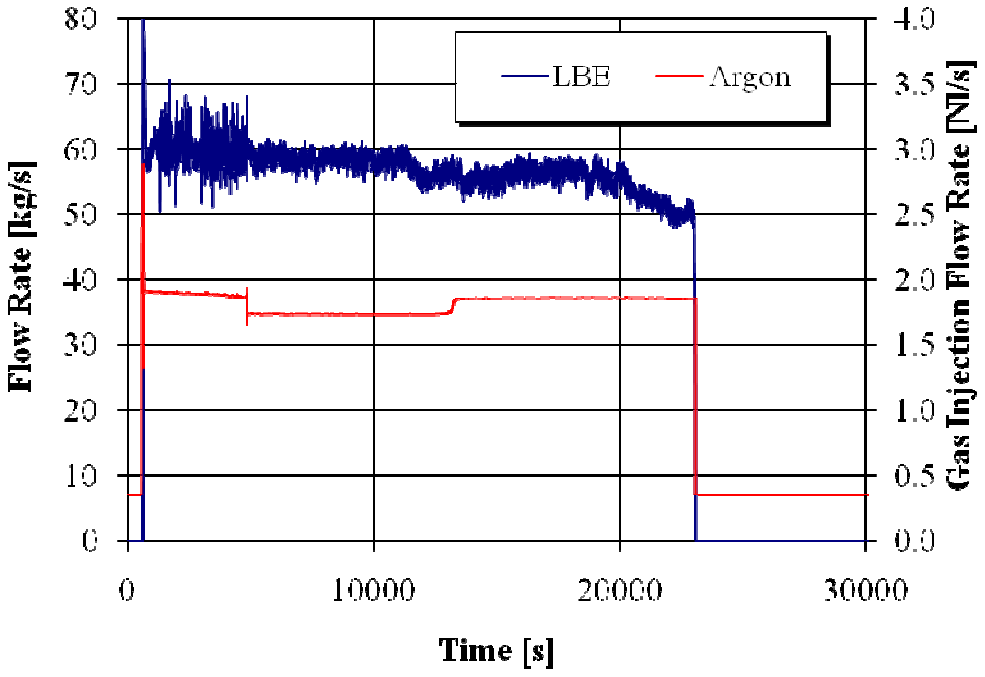

Figure 48. Test C: trend of the gas injection flow rate and the related LBE flow rate along the ICE test section.

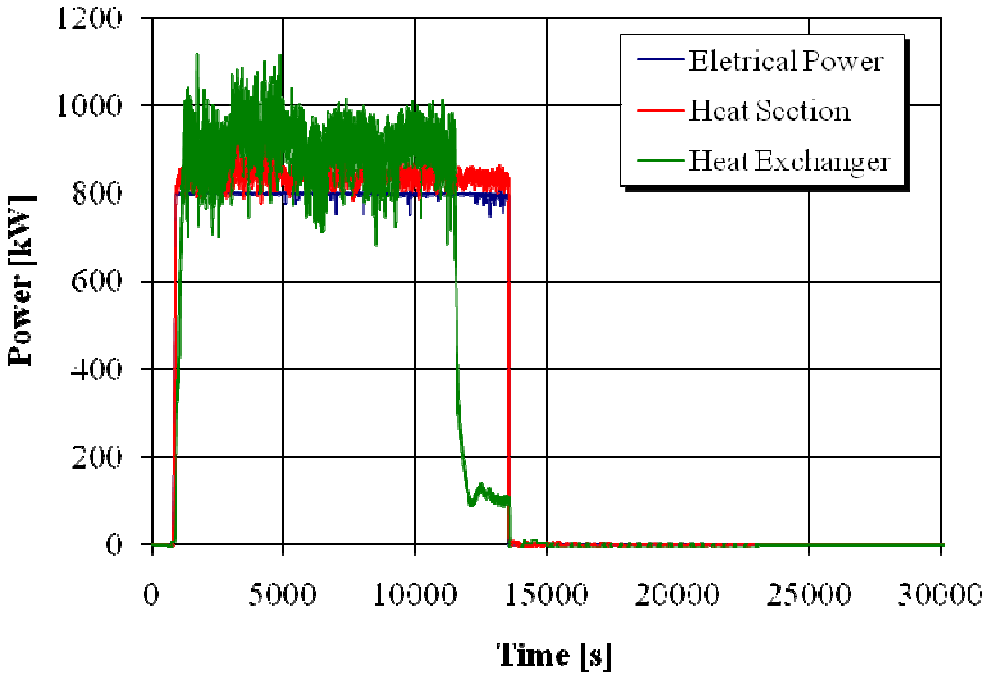

Figure 49. Test C: Trend of supplied electrical power and the removed thermal power calculated along the heat source and heat exchanger

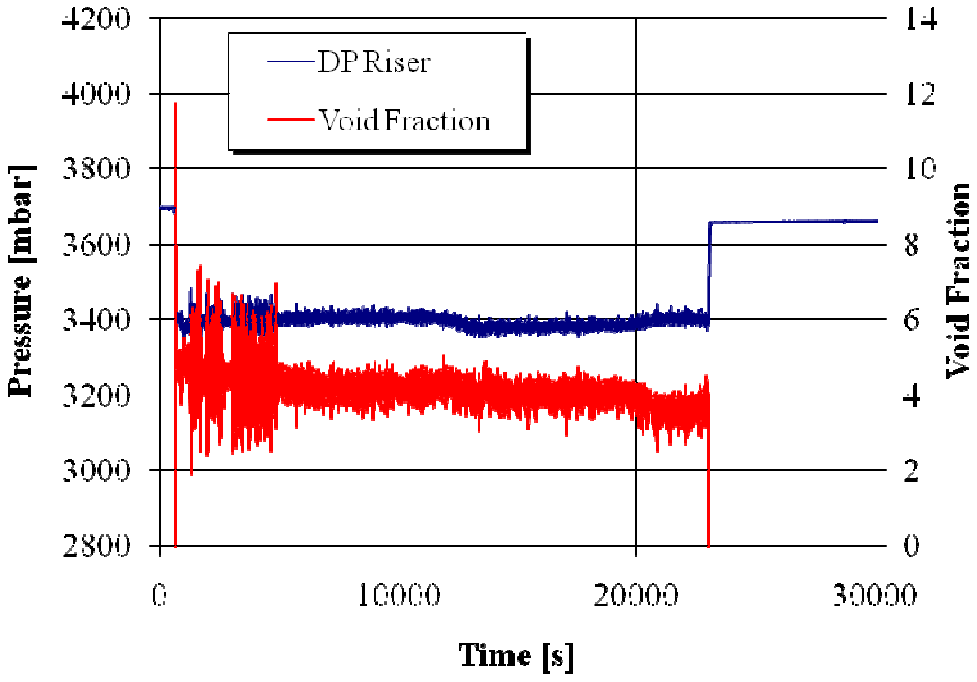

Figure 50. Test C: pressure difference measured along the riser during the test and estimated average void fraction into the riser

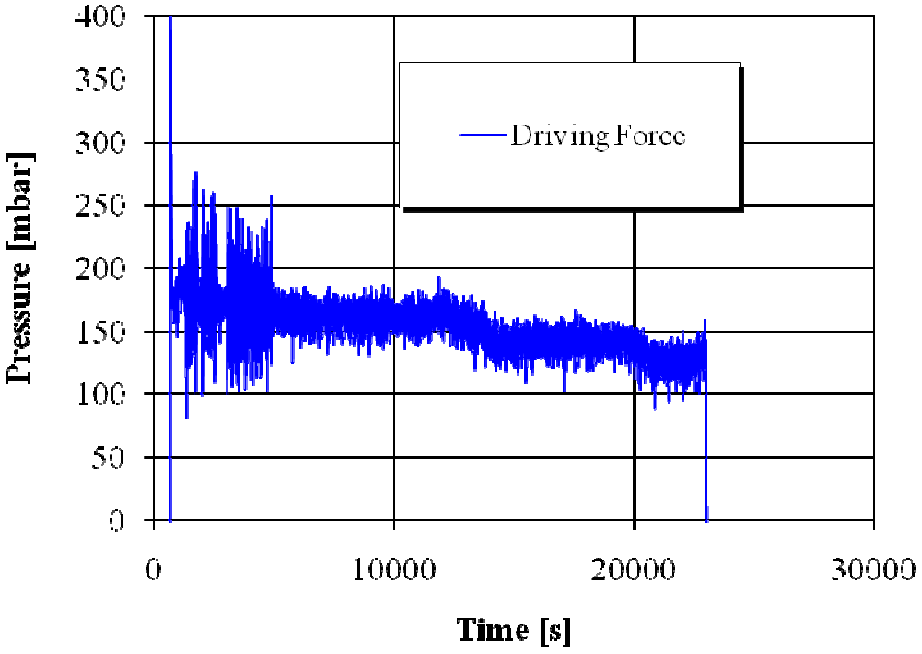

Figure 51. Test C: driving force available for LBE circulation along the ICE flow path.

The LBE temperature is nearly uniform at HS inlet section. On the contrary, temperature differences are observed at the outlet section due to a non-uniform behaviour among the different subchannels of the fuel bundle (see Figure 53).

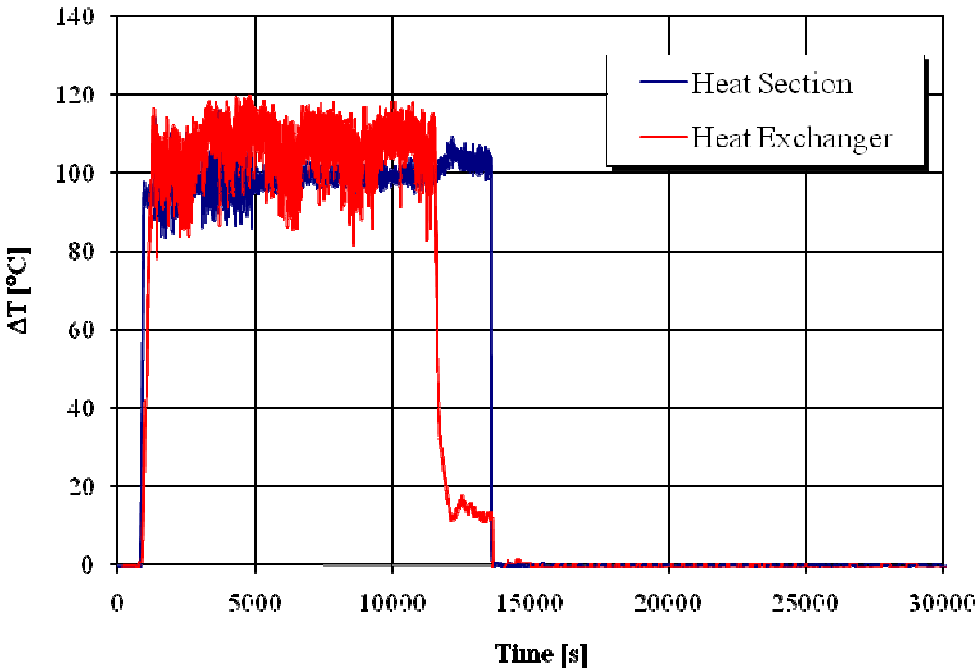

Figure 52. Test C: thermal difference through the inlet and outlet section of the Heat Section and Heat Exchanger (LBE side).

Figure 54 evidences a temperature difference between the coolant at HS outlet and at HX inlet in the order of 50 °C. This difference is associated to the heat exchange between the riser and the downcomer in CIRCE facility.

These steady state conditions are consistent with those resulting from the Test B, thus demonstrating the reliability of the design and execution of the experiment [29] .

The initiating event occurs at 11420 s, when the valve of the secondary side feed water are closed, thus resulting in decrease of heat removal from secondary side transient.

The power removed by the HX (Figure 49) drops reaching 200 kW in less than 400 s and then, smoothly, zero. The steam quality at the HX rapidly increases from 0.55 up to 1 until the secondary system is completely emptied (Figure 56).

The temperature difference across the HX is reduced consistently with the power (Figure 52).

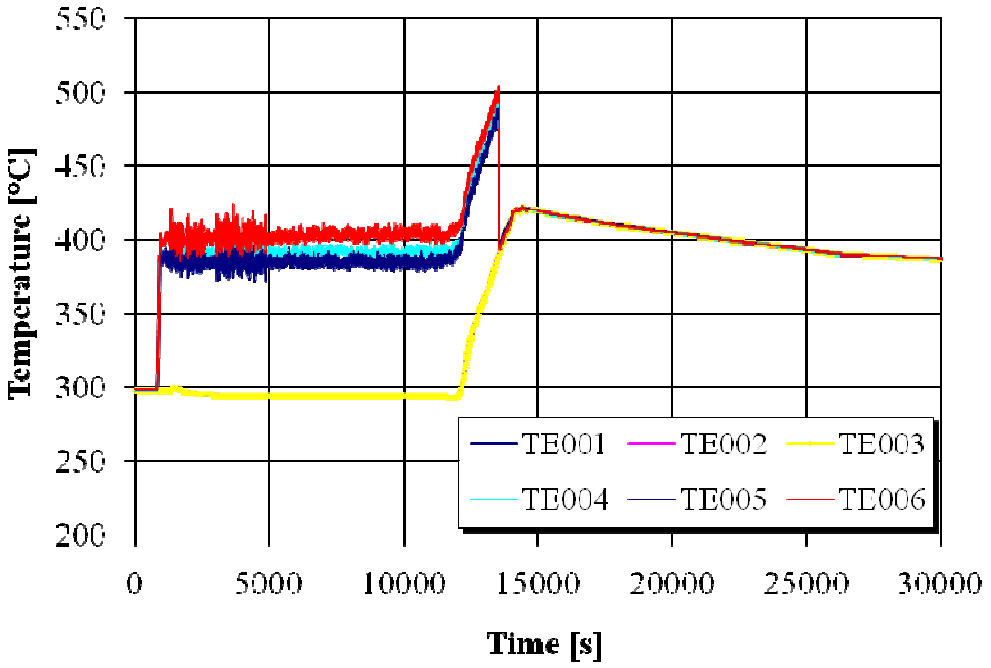

Figure 53. Test C: trend of the temperatures at the inlet (TE001, TE002, TE003) and outlet (TE004, TE005, TE006) of HS. The thermocouples have been installed, both in the inlet than in the outlet, at different depth into the pins bundle, to verify the uniformity of the temperature in the sections.

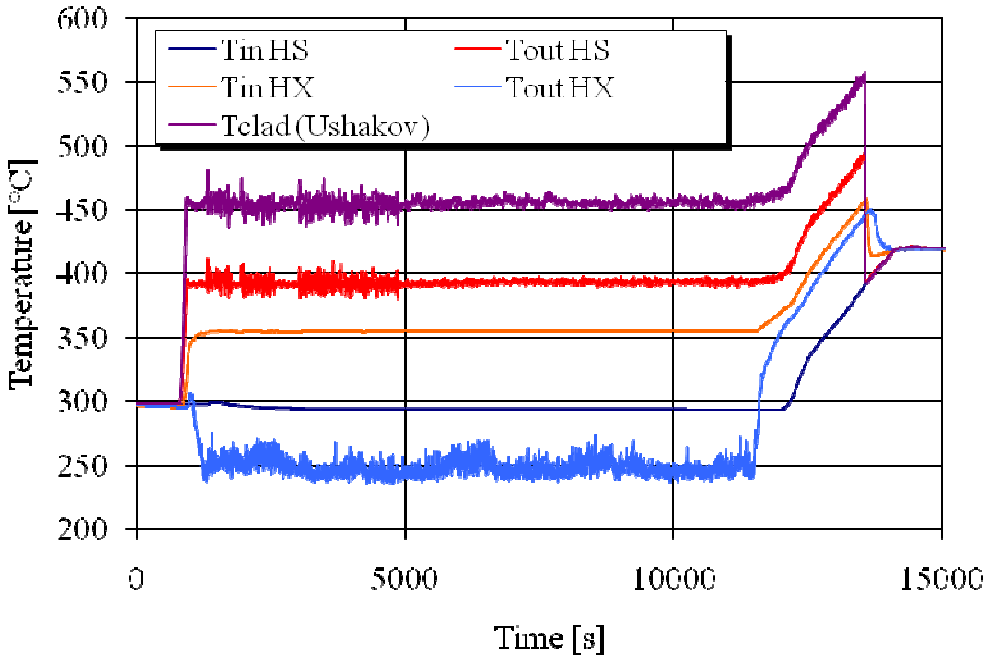

Figure 54. Test C: trend of the average inlet and outlet temperature along the HS and inlet and outlet temperature through the HX (LBE side).

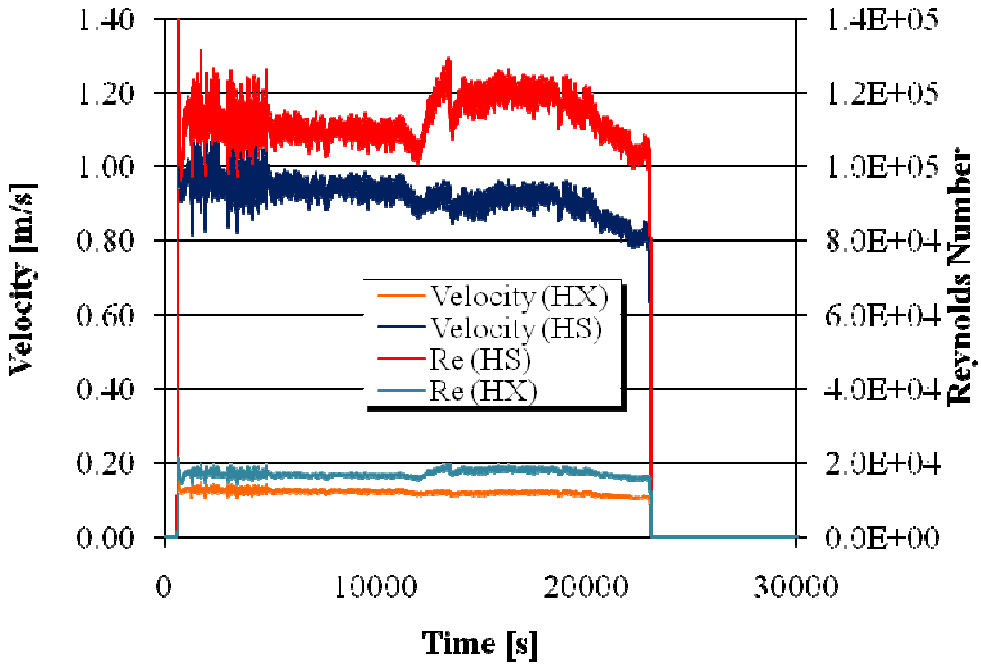

Figure 55. Test C: average LBE velocity through the rods bundle and bayonet tubes of the HX. Reynolds number for the liquid metal stream line inside the HS and HX. Full power test.

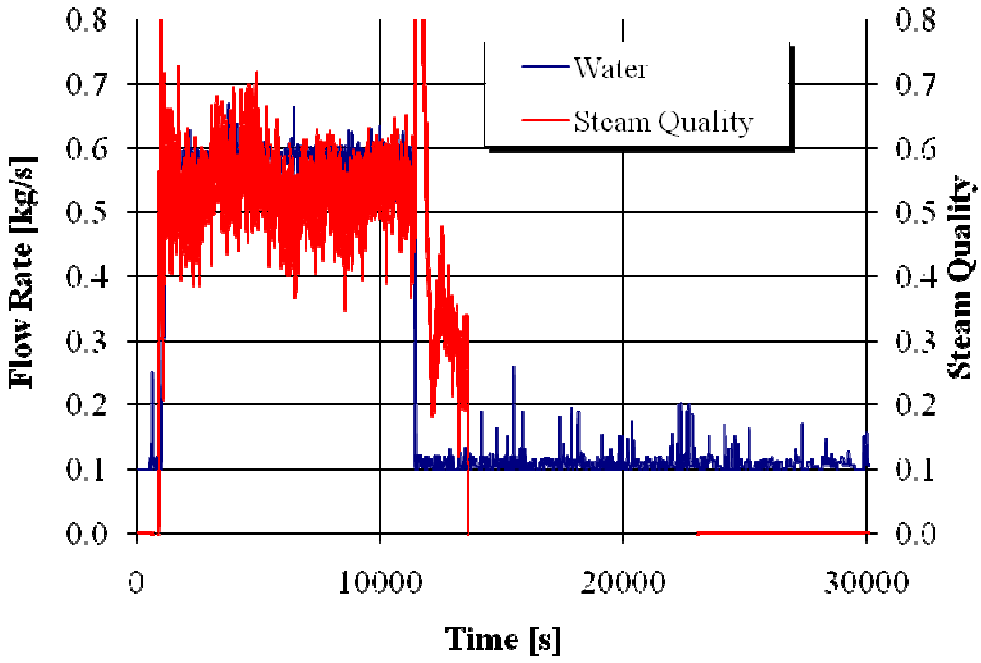

Figure 56. Test C: trend of the water flow rate supplied to the HX.The steam quality trend is evaluated starting from the thermal power removed by the heat exchanger calculated on the LBE side.

The effect of the loss of heat sink on the primary flow rate is negligible (roughly -2 kg/s) because the larger contribute is due to the gas lift system (i.e. void buoyancy) with respect to the density difference (i.e. density buoyancy). This is observed in Figure 48, and highlighted in Figure 51 where both contributions are taken into account.

Because of the unbalance of energy, the LBE temperature of the system rises with a rate of about 0.06 °C/s.

At 13570 s the coolant temperature at HS outlet is equal to 495°C and the electrical power is so switched off. In these conditions, the coolant temperature is rapidly equalized in the primary system at about 420 °C. As soon as the equilibrium is reached, the temperature is uniform in the circuit with a flow driven by the gas injection system.

The temperature decreases slowly for the effect of the heat losses through the vessel. At 23050 s, the gas flow injection system is stopped and the LBE became stagnant. The data acquisition system is switched off after 34650 s of operation.

Table 8 summarizes the resulting sequence of main events.

#	Time [s]	Event	Comments
1	0	Start recording data	
2	575	Gas flow injection system switched on	
3	650	Onset of LBE buoyancy driven flow	
4	820	FRSB switched on	
5	960	FW valves open (HX operated)	
6	11420	FW valves close	Initiating event: Unprotected loss of cold sink
7	13560	Fuel bundle power switched off	
8	13565	Maximum LBE temperature at HS outlet	
9	23050	Gas flow injection system switched off	
10	23050	LBE flow equal to zero	
11	34650	End recording data	

Table 8. resulting sequence of main events.

3.4 Test D: Unprotected Loss of Flow

Test D is an experiment investigating the system behaviour following loss of flow scenario. Three main phases are identified:

- from 0 s up to 10735 s: conditioning phase for achieving the reference initial conditions;
- from 10735 s up to 15025 s: occurrence of initiating event and simulation of the postulated transient;
- from 15025 s up to 24660 s: mitigation phase for bringing the test facility in safe conditions.

The test started with the system in hot conditions at zero power. The primary coolant is stagnant and the temperature is uniform in the circuit (at about 295 °C).

The gas flow injection system is switched on at time 0 s. The compressor reaches the stationary conditions after about 4650 s, injecting an average flow rate of 3.0 Nl/s. The resulting buoyancy force induces a flow circulation in the ICE loop corresponding roughly to 68 kg/s (Figure 57), according with the specifications.

The electrical power is turned on at about 900 s and it is set at the nominal value (750 kW) with a two steps procedure, which is completed after 3200 s (Figure 58).

About 300 s later, the FW system is activated, by means of the valves upstream the HX and the energy balance is re-established in the system. The gas lift system is then stabilized (see above) and the facility is operated in stationary conditions until 10735 s when the initiating event occurs.

In these conditions, the void fraction is slightly less than 8% (indirect derivation) and the pressure difference across the riser is 3300 mbar (dynamic head), as depicted in Figure 59. The driving force results almost 300 mbar, see Figure 60. The LBE flow velocity is larger than 1 m/s (Figure 64), thus resulting turbulent both in the pin bundle (HS) and in the bayonets tubes (HX), as well.

The temperature difference between the inlet and outlet of HS is 80 °C, whereas it results about 100 °C in the HX (Figure 61).

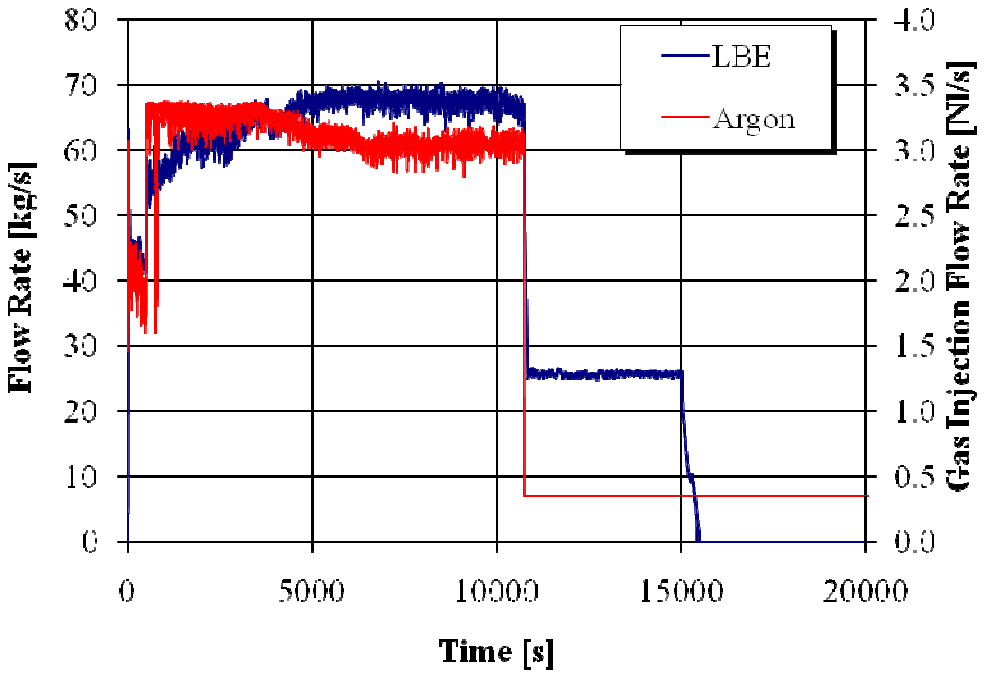

Figure 57. Test D: trend of the gas injection flow rate and the related LBE flow rate along the ICE test section.

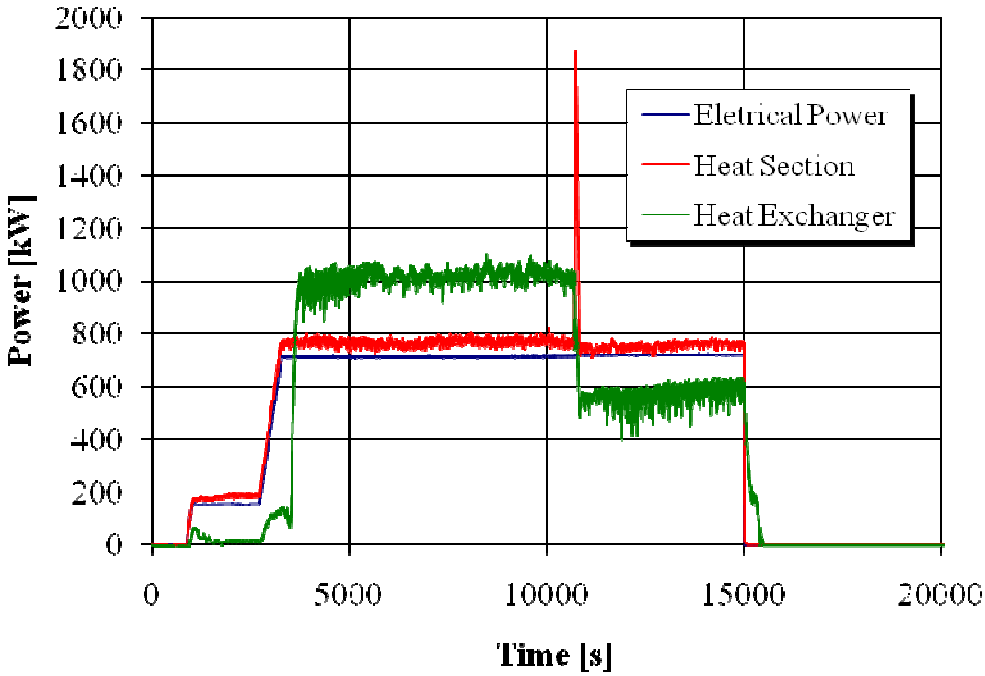

Figure 58. Test D: Trend of supplied electrical power and the removed thermal power calculated along the heat source and heat exchanger

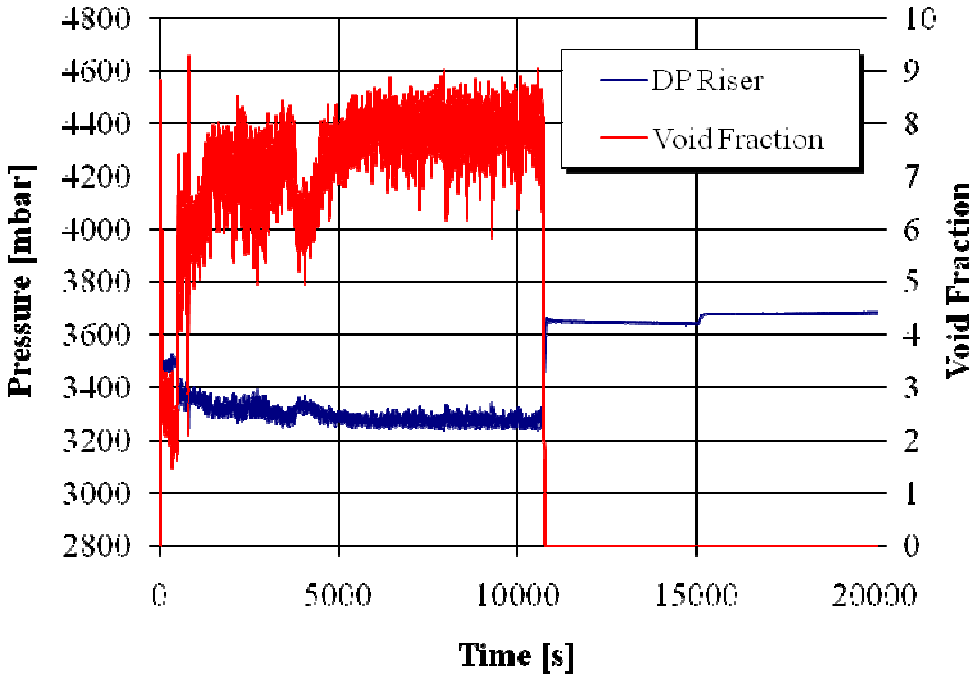

Figure 59. Test D: pressure difference measured along the riser during the test and estimated average void fraction into the riser

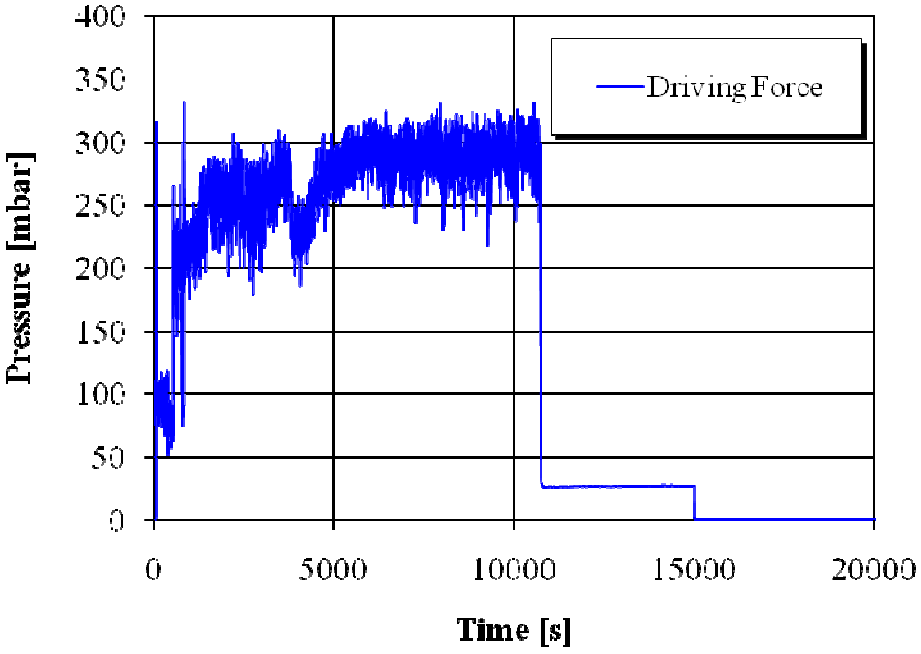

Figure 60. Test D: driving force available for LBE circulation along the ICE flow path.

This difference causes the difference between the power removed by the HX and the power provided by the fuel bundle, as reported in Figure 58, which is affected by a large uncertainty in the measures.

Indeed, this measure is indirectly derived and it is influenced by the mass flow rate flowing across the HX, which is assumed the same as in the core. On the contrary, when the gas lift system injects higher values of gas flow and therefore the void fraction results higher, the swelled level overpasses the barrier in the top of the test section designed for carrying the LBE from HS to the HX and part of the heated coolant overflows down in the downcomer.

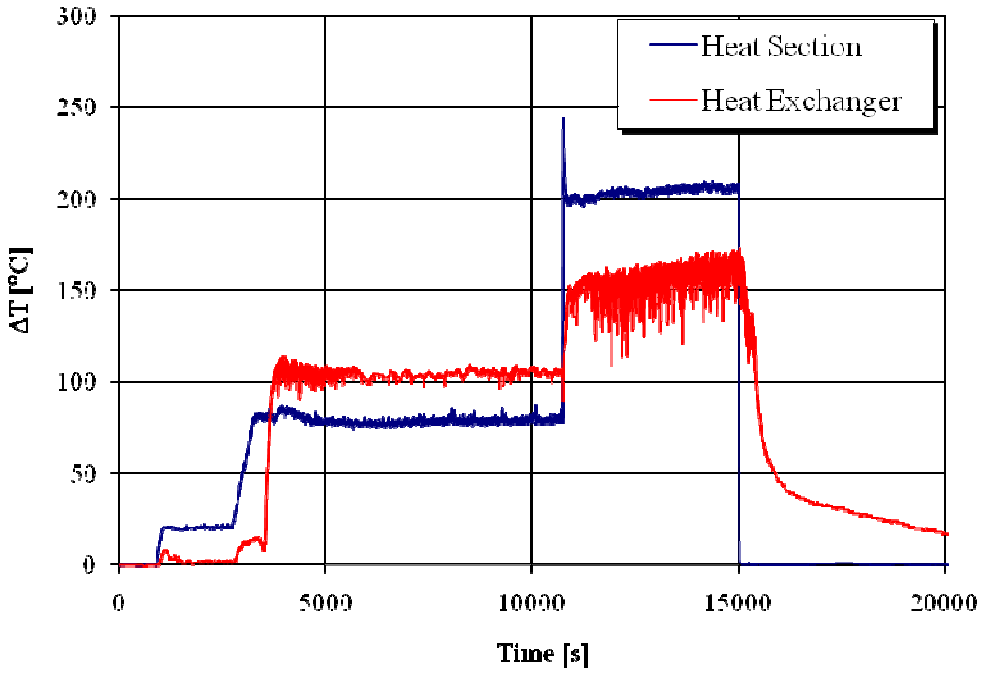

Figure 61. Test D: thermal difference through the inlet and outlet section of the Heat Section and Heat Exchanger (LBE side).

The LBE temperature is nearly uniform at HS inlet section. The measures at the outlet section show that the temperature differences are more narrow than in the Test C (see Figure 62).

This difference is connected with the larger void fraction in the riser, which contributes in increasing the main flow rate along the test section and so the velocity in the test section. Moreover, the higher velocity should be the reason why the

temperature difference between the coolant at HS outlet and at HX inlet in the order of 20 °C (Figure 63), instead of almost 50 °C as in test B and C.

The steady state conditions are successfully maintained for more than 5000 s, before the starting of transient.

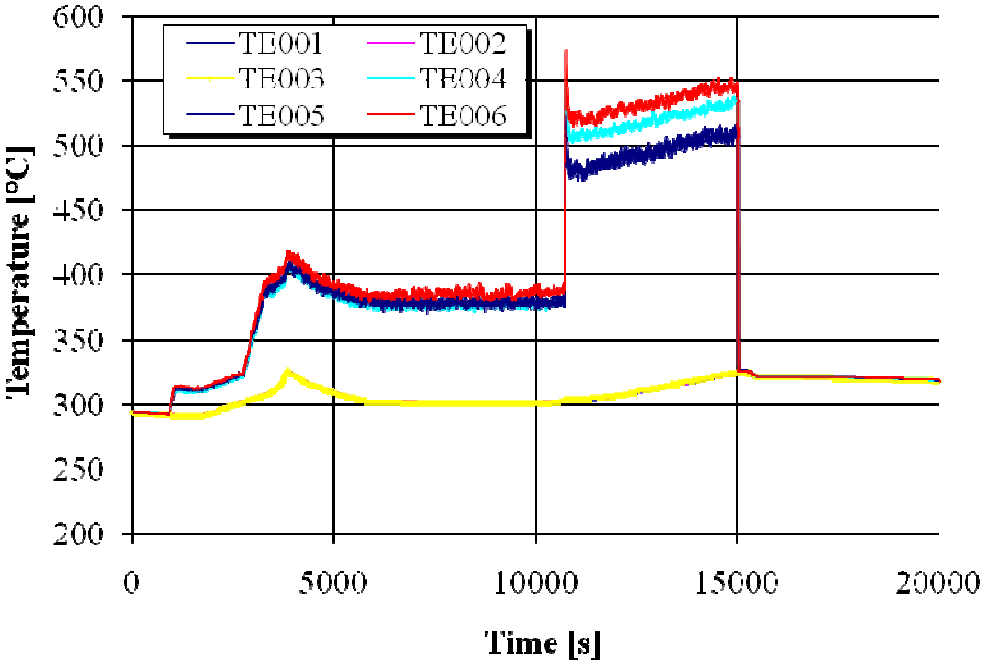

Figure 62. Test D: trend of the temperatures at the inlet (TE001, TE002, TE003) and outlet (TE004, TE005, TE006) of HS. The thermocouples have been installed, both in the inlet than in the outlet, at different depth into the pins bundle, to verify the uniformity of the temperature in the sections.

The initiating event occurs at 10735 s, when the gas lift system is shouted down, thus suddenly reducing the mass flow rate in the system. The LBE temperature at core outlet drastically increases, and a density driven flow is re-established in few tens of seconds.

In these conditions, the primary system mass flow is 25 kg/s, the temperature difference across the core is larger than 200 °C and the LBE core outlet temperature increases with a rate of 0.008 °C/s.

An energy unbalance is observed in the system because the power removed by the HX is almost 200kW lower than the power released by the HS (see Figure 58). This is caused by the heat released in the riser of the test section towards the downcomer. Indeed, the LBE temperature at HX inlet is 100 °C lower than it is at the

HS outlet. Notwithstanding this distortion, the test D successfully demonstrates the capability of the system to be operated in natural circulation in case of unprotected loss of flow.

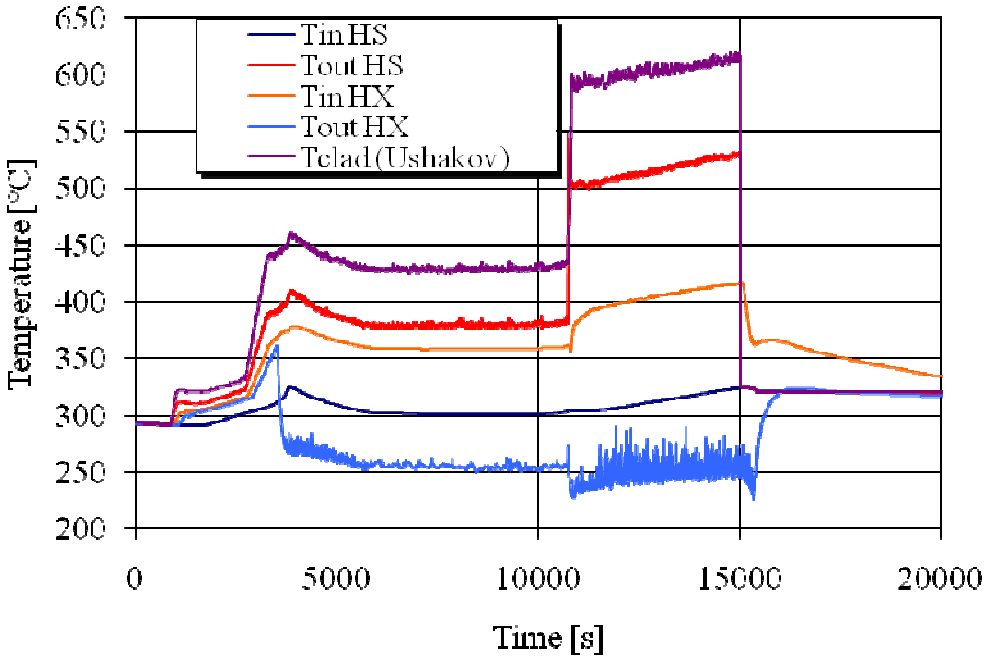

Figure 63. Test C: trend of the average inlet and outlet temperature along the HS and inlet and outlet temperature through the HX (LBE side).

As soon the LBE temperature at core outlet reached 530 °C, the power is switched off (15025 s). The coolant temperature tends to be equalized, nevertheless it results higher at HX inlet. In these conditions the energy is transmitted from the doencomer to the riser of the test section. Thus, in the downcomer exists a “quasi” stagnant zone which does not mix with the other coolant and therefore, it is at higher temperature (thermal stratification).

At 15295 s, the FW is closed (Figure 65) and about 10000 s later the data acquisition system is switched off after 24660 s of operation.

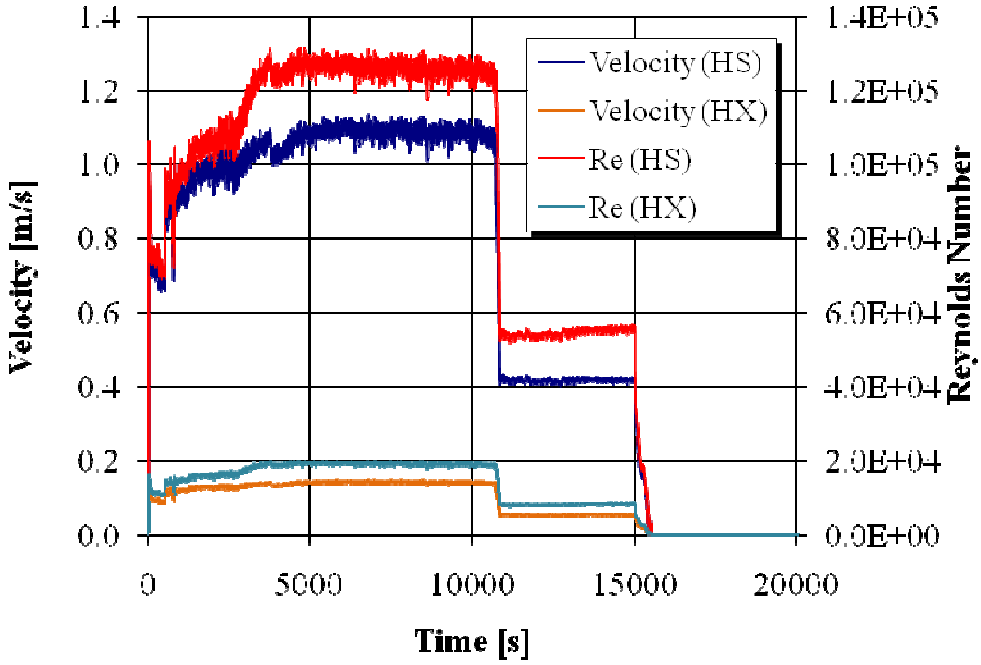

Figure 64. Test C: average LBE velocity through the rods bundle and bayonet tubes of the HX. Reynolds number for the liquid metal stream line inside the HS and HX. Full power test.

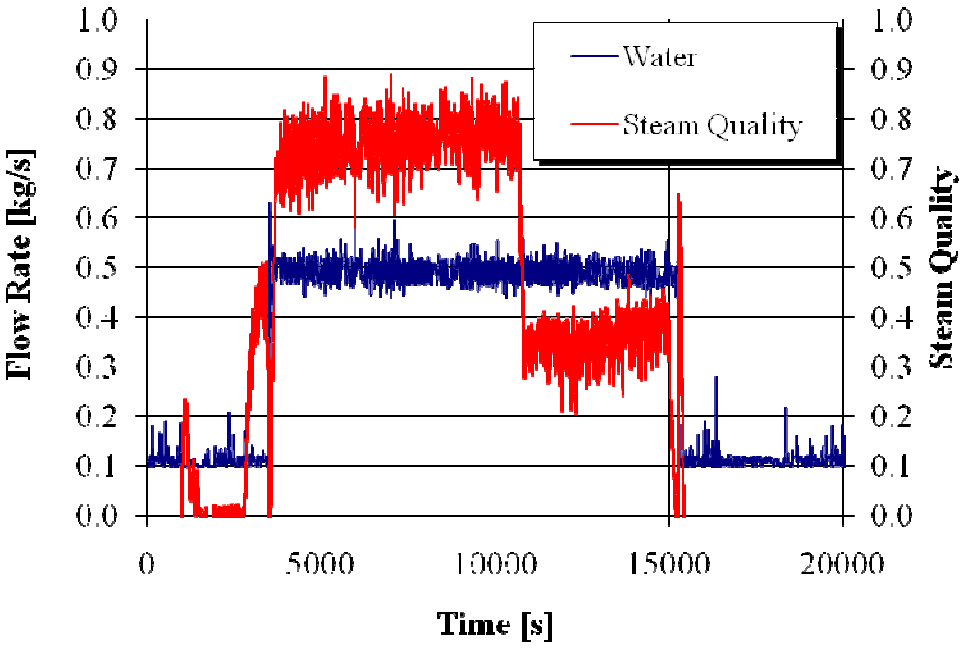

Figure 65. Test C: trend of the water flow rate supplied to the HX.The steam quality trend is evaluated starting from the thermal power removed by the heat exchanger calculated on the LBE side.

Tab. *9* summarizes the resulting sequence of main events.

#	Time [s]	Event	Comments
1	0	Start recording data	
2	0	Gas flow injection system switched on	
3	900	FRSB switched on	
4	3200	FRSB power set to 750 kW	
5	3505	FW valves open (HEX operated)	
6	4650	Gas flow injection system reaches the steady state conditions	
7	4650	LBE void buoyancy driven flow reaches the steady state conditions	
8	10735	Gas flow injection system switched off	Initiating event: Unprotected loss of flow
9	10735	LBE mass flow rate decrease	
10	10840	LBE mass flow rate stabilization in natural circulation (density buoyancy driven flow)	
11	15010	Maximum LBE temperature at HS outlet	
12	15025	FRSB power switched off	
13	15295	FW valves close	
14	15500	LBE flow equal to zero	
15	24660	End recording data	

Table 9. resulting sequence of main events.

4. TEST MATRIX

As already mentioned, the aim of the CIRCE experiment is to characterize the phenomena of mixed convection and stratification in a heavy liquid metal pool in the safety relevant situation, that is during the transition from nominal flow conditions to the natural circulation typical of Decay Heat Removal (DHR) conditions.

For this reason four different tests are foreseen.

TEST 1: Isothermal Circulation tests

The aim of the tests is to get a hydro dynamic characterization of the tests section. The tests will be run at zero power, isothermal condition, performing the gas enhanced circulation tests at different flow rate and measuring the associated liquid metal flow rate along the main flow path.

The following main parameter will be adopted:

1. isothermal pool temperature:250°C, 300°C, (350°C)
2. gas flow rate: 1, 1.5, 2, 2.5, 3, 4, 5, 6 Nl/s
3. duration of each test: 30 – 60 min
4. vessel heating system: active
5. HX, DHR not active

TEST 2: Full Power Circulation test

The test aiming to fully characterize the circulation along the primary flow path at full power, addressing the performance of the HX, and verifying the consistencies of the upgraded test section, as the coupling between HS and HX.

During the test all the instrumentation adopted will also make available reliable data for the preliminary qualification and validation of system code and CFD codes when employed in HLM pool systems, in particular for what concern the temperature measurement into the fuel bundle.

The following main parameter will be adopted:

1. thermal power in the HS:800 kW
2. HLM flow rate: 55 kg/s (by gas lift)

3. ΔT along the HS: 100°C
4. average velocity into the HS:1m/s
5. average temperature along the main flow path: 350°C
6. vessel heating system: active
7. HX flow rate: 0.5 kg/s
8. DHR: not active
9. duration of the test: 3-5 hour of steady state

TEST 3: Protected Loss Of Heat sink (PLOH) and Loss of Flow (LOF)

The test aiming to simulate the loss of the main heat exchanger (HX), the consequent scram of the core, and activation of the DHR system to remove the decay heat power (5% of the nominal value) in a HLM nuclear system. During the transition the main pump will be stopped to simulate the pure transition from the forced to the natural circulation under the decay heat removal regime.

The test will allow to characterize the transition from the “forced” to natural circulation in a HLM pool, addressing the mixing and thermal stratification phenomena into the pool after a PLOH+LOF transient, and the thermal -hydraulic coupling of the DHR’s secondary flow with the main flow path.

At the same time, during the transition will be possible to monitoring the temperature trend on the fuel cladding, which is one the main parameters to be considered for the safety assessment of HLM nuclear systems under the decay heat removal regime.

The test will be performed starting from the nominal conditions, as depicted in the test 2, and performing the PLOH+LOF transition.

The following main parameter will be adopted:

Nominal Steady State

1. thermal power in the HS:800 kW
2. HLM flow rate: 55 kg/s (by gas lift)
3. ΔT along the HS: 100°C
4. average velocity into the HS:1m/s
5. average temperature along the main flow path: 350°C
6. vessel heating system: active
7. HX flow rate: 0.5 kg/s
8. DHR: not active
9. duration of the test: 3-5 hour of steady state

PLOH+LOF transient

10. Isolation of the main HX (isolating the feed water)
11. Core “scram” at 40 kW (decay power)
12. start-up of the DHR-system (air flow rate of 0.3 kg/s)
13. “Main pump” turn-off (the gas injection is interrupted)
14. vessel heating system: active
15. duration of the test: 3-5 hour of steady state

TEST 4: Protected Loss Of Heat sink (PLOH)

The test aiming to simulate the loss of the main heat exchanger (HX), the consequent scram of the core, and activation of the DHR system to remove the decay heat power (5% of the nominal value) in a HLM nuclear system.

In this the test the primary pump (gas lift) will be active to investigate the behaviour of the system with an imposed flow rate along the primary flow path.

The test will allow to characterize the postulated transient in a HLM pool, addressing the mixing and thermal stratification phenomena into the pool after a PLOH transient, as well as the thermal -hydraulic coupling of the DHR’s secondary flow with the main flow path.

At the same time, during the transition will be possible to monitoring the temperature trend on the fuel cladding, which is one the main parameters to be considered for the safety assessment of HLM nuclear systems under the decay heat removal regime.

The test will be performed starting from the nominal conditions, as depicted in the test 2, and performing the PLOH transition.

The following main parameter will be adopted:

Nominal Steady State

1. thermal power in the HS:800 kW
2. HLM flow rate: 55 kg/s (by gas lift)
3. ΔT along the HS: 100°C
4. average velocity into the HS:1m/s
5. average temperature along the main flow path: 350°C
6. vessel heating system: active
7. HX flow rate: 0.5 kg/s
8. DHR: not active
9. duration of the test: 3-5 hour of steady state

PLOH transient

10. Isolation of the main HX (isolating the feed water)
11. Core “scram” at 40 kW (decay power)
12. start-up of the DHR-system (air flow rate of 0.3 kg/s)
13. main pump active (gas lift)
14. vessel heating system: active
15. duration of the test: 3-5 hour of steady state

5. TEST SECTION UPGRADE

To accomplish the assumed commitments with the CIRCE experiment, as well as to improve the performance of the test section, several modifications have to be implemented on the ICE test section.

In particular, also thanks to the post-test analyses carried out on the DEMETRA experimental data, seems to be mandatory implement the following actions.

- Install a more suitable instrumentations on the main HX, in particular it has been highlighted as a better evaluation of the inlet and outlet average temperature through to HX (LBE side) is necessary to better evaluate the power extracted by the component. Simultaneously, to better address the performance of the HX, it is mandatory to monitor the LBE temperature in some subchannels of the HX, through the bayonet tubes.
- Increase the height of the wall of the separator, to guarantee that the LBE flow rate really flow into the HX's shell during the tests. In fact, due to the strongly gas bubbling into the separator (see figure 3), there is the possibility that part of the LBE flow rate flow directly into the downcomer, compromising the evaluation of the power removed by the main HX.
- Improve the thermal-hydraulic coupling of the main HX with the downcomer adding a suitable flow straightener in the lower part of the shell.
- Achieve the thermal insulation of the riser, in order to reduce the thermal exchange towards the quasi stagnant LBE into the downcomer.
- Install the decay heat removal heat exchanger into the pool.
- Install suitable instrumentations for the mixing and thermal stratification assessment into the pool.
- Instrument the fuel pin bundle aiming to evaluate the heat transfer coefficient in HLM cooled rod bundle, evaluate the hot spot factor due to the installed spacer grid along the bundle, monitoring the pin cladding temperature under the postulated transients.

The main of the listed actions are hereafter depicted.

5.1 Decay heat removal heat exchanger

The decay heat removal heat exchanger has been designed to have a thermal duty of 40 kW, which represents the 5% of the ICE nominal power (800 kW).

As foreseen by the CIRCE experimental commitment it will be placed into the main vessel downcomer, hydrodynamically not coupled with the main flow path, as depicted in figure 66.

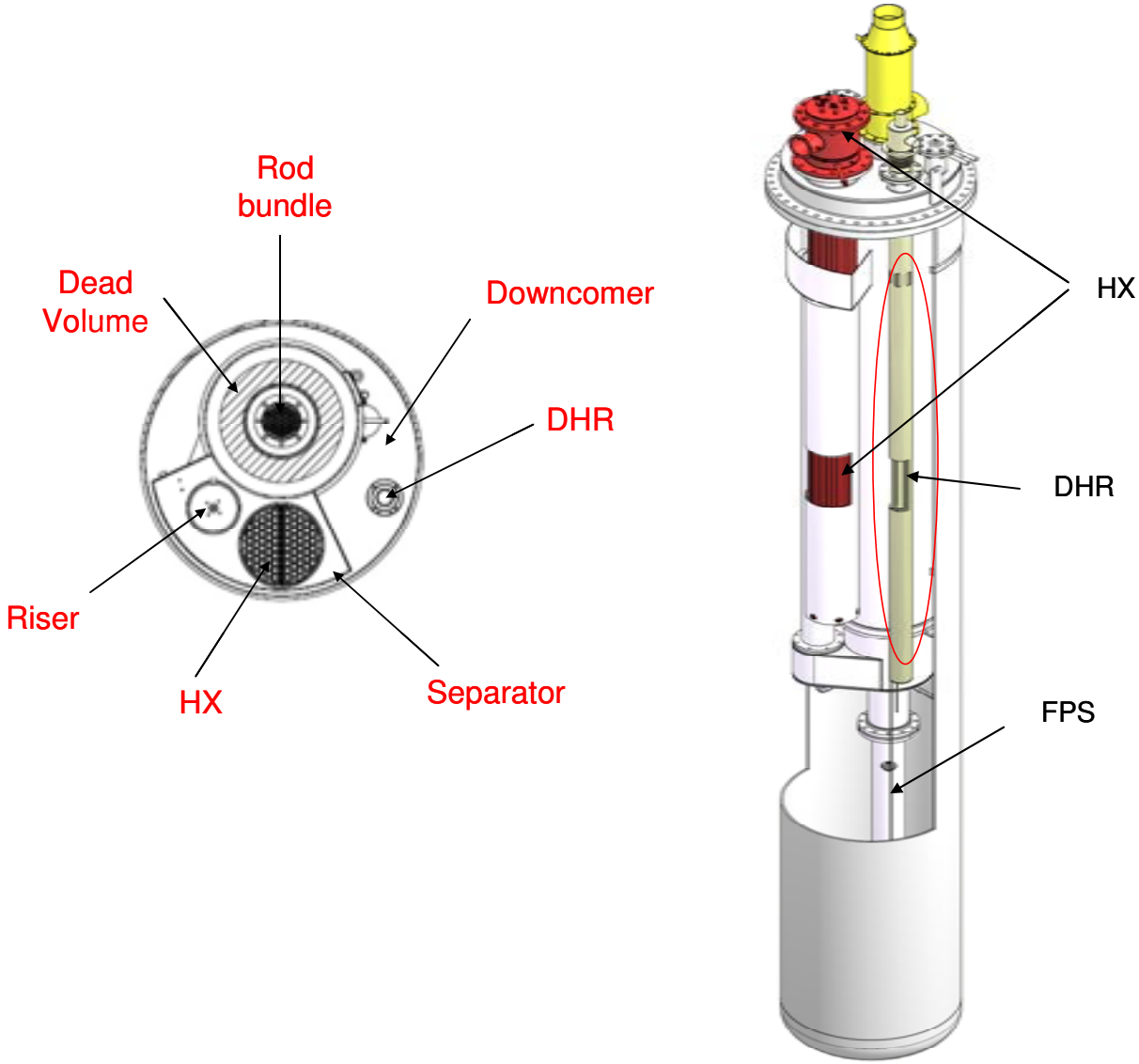

Figure 66. View of the position for the DHR-HX into the CIRCE facility, ICE configuration

The decay heat removal heat exchanger (DHR-HX) consists of a bayonet element made of two concentric tubes. The inner tube is opened at the bottom, while the external tube has a bottom end sealed (see figure 67).

The air is injected from the top, flows downward in the inner tubes, and then flows upward in the annulus between the tubes. In the annulus the thermal exchange takes place.

The bayonet element is placed into a suitable shell. The LBE enters in to the shell from the top (where appropriate holes are realized on the wall of the shell) and flows downward allowing a count current heat exchanger with the air flowing into the annulus.

At the inlet section as well as at the outlet section, 6 TCs will be installed to well monitoring the inlet and outlet temperature of the LBE. (see figure 67)

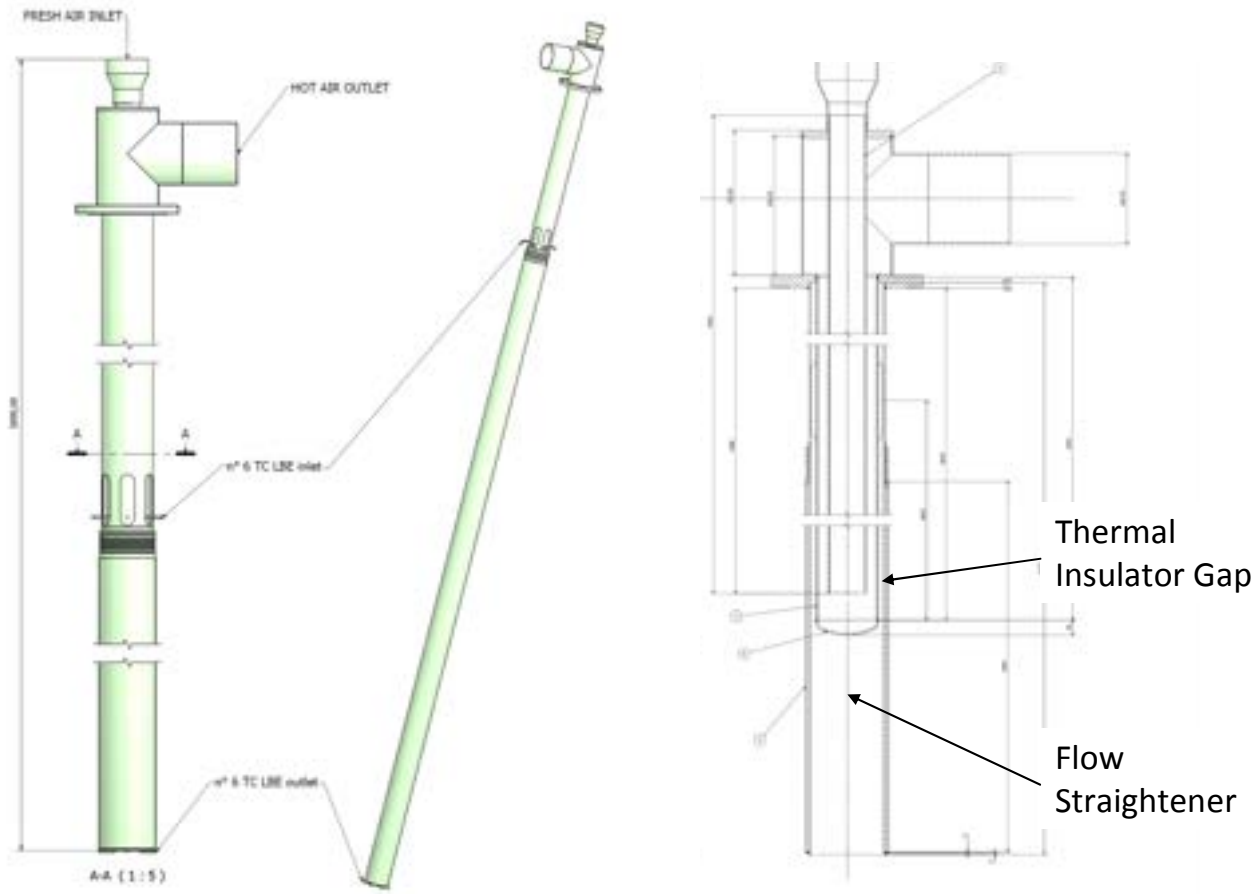

Figure 67. View of the DHR HX, adopted instrumentations, flow straightener, shell thermal insulator

On the lower part of the shell a flow straightener is foreseen allowing to homogenise the LBE flows into the downcomer.

Finally to reduce the thermal exchange between the LBE flowing into the DHR and quasi stagnant LBE into the downcomer, a thermal insulation is foreseen on the shell. The thermal insulation is realized by a double wall shell filled by air, with a gap of 4.6 mm. The gap of stagnant air, filled at room pressure and temperature (before the sealing) allows to drastically reduce the thermal coupling with the downcomer.

In table *10* the main parameter of the decay heat removal system are listed.

Thermal Duty	40 kW
Fluid Shell side	LBE
LBE inlet temperature	340°C
LBE outlet temperature	306°C
Fluid tube side	Low pressure air
Air Inlet temperature	20°C
Air Outlet temperature	152°C
Air flow rate	0.3 kg/s
Air pressure drops	8500 Pa
Shell Length (below the free level)	4435 mm
Active length	4028 mm
Straightener length	407 mm
Shell inner diameter	139.7 mm
Shell insulation gap thickness	4.6 mm
Bayonet inner tube (ID x thick.)	70 x 2.77 mm
Bayonet external tube (ID x thick.)	114.30 x 3 mm

Table 10. Main characteristics of the decay heat removal heat exchanger

In figure 68 the mechanical drawing of the decay heat removal heat exchanger is reported.

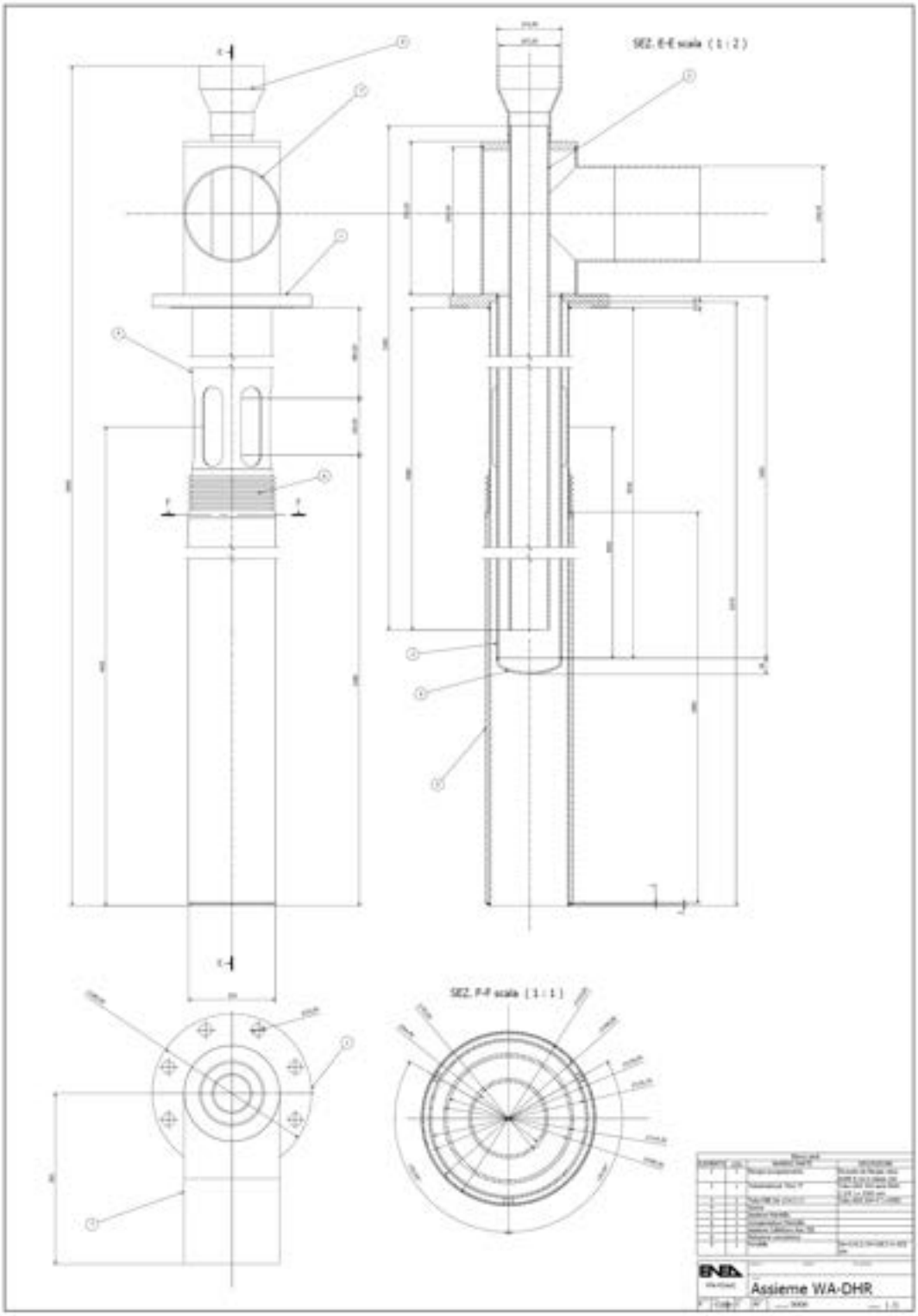

Figure 68. Mechanical Drawing of the decay heat removal heat exchanger

5.2 Test Section Instrumentations upgrade

For what concern the monitoring of the mixing and thermal stratification into the CIRCE pool, a suitable instrumentations has been defined to achieve these goals.

New instrumentations will be also added along the HX as along the main flow path aiming to better investigate the fluid-dynamic behaviour of the pool system during the steady state conditions as well as during the postulated transients.

Moreover the new installed instrumentation on the facility will also provide more reliable and accurate experimental data aiming to validate CFD and system codes when employed on a HLM pool.

In figure 69 is reported a detailed sketch of the upgraded ICE test section where the adopted instrumentation (in particular thermocouples) is reported.

In details the following instrumentations will be installed.

DHR-HX: to monitoring the average inlet and outlet temperature of the LBE in the component the following thermocouples are foreseen (see figure 67):

- 6 TC Inlet DHR-HX
- 6 TC Outlet DHR-HX

HX: to monitoring the average inlet and outlet temperature of the LBE in the component, and to investigate the subchannels behaviour among the bayonet elements, the following thermocouples are foreseen:

- 3 TC Inlet HX
- 9 TC into the subchannels of the HX (on which subchannels and the relative deepness has to be confirmed)
- 6 TC Outlet HX

Riser: to monitoring the average inlet and outlet temperature of the LBE in the riser, allowing to investigate the thermal coupling of the component with the downcomer, the following thermocouples are foreseen:

- 3 TC Inlet the riser
- 3 TC Outlet the riser

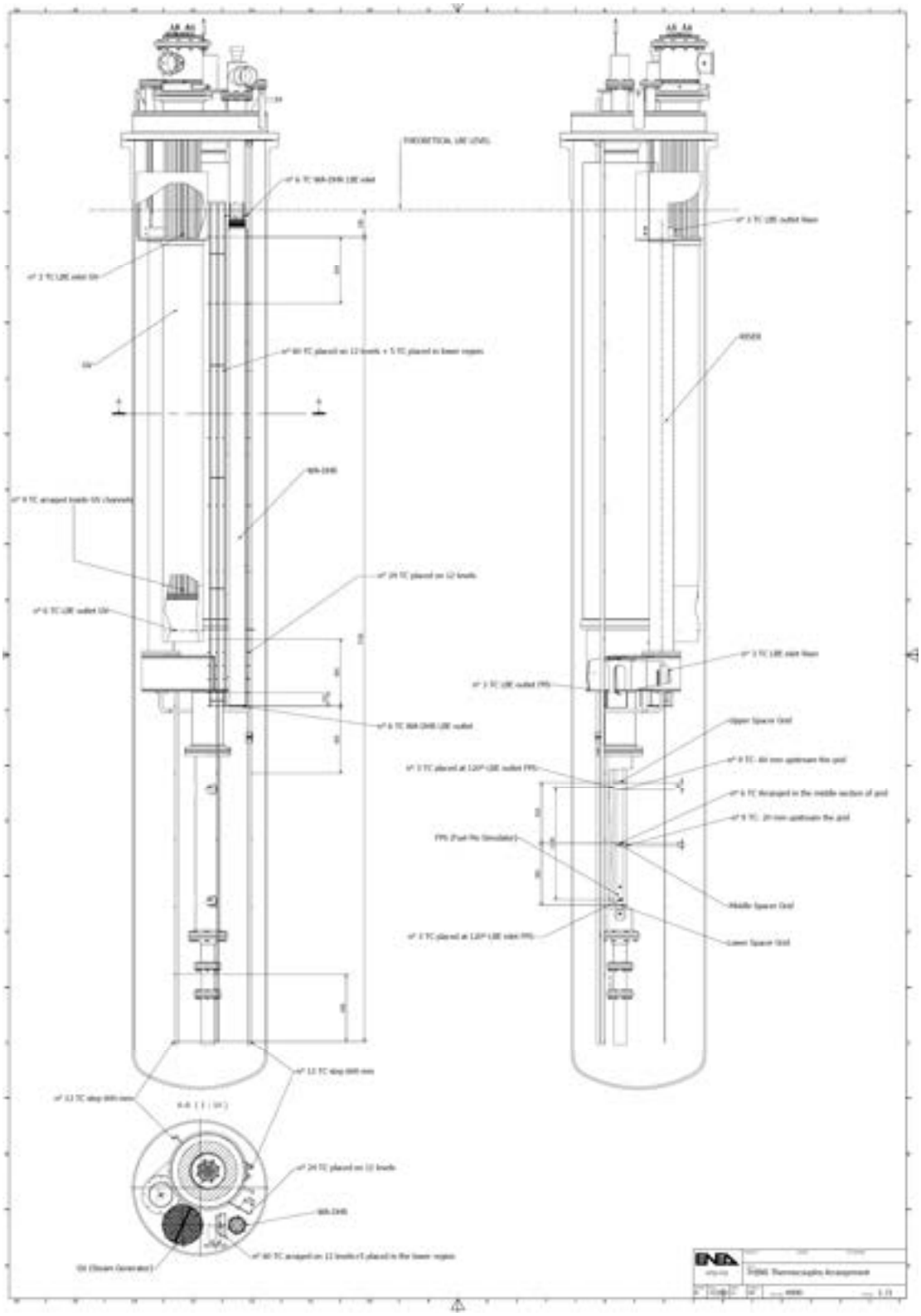

Figure 69. Sketch of the upgrade ICE test section with the installed instrumentations.

Downcomer: to monitoring the mixing and thermal stratification during the postulated transients the following thermocouples are foreseen:

- 65 TC placed on 12 levels between HX and DHR-XH (see figures 70, 71, group C)
- 26 TC placed into the downcomer (see figure 71, group A)
- 24 TC placed on 12 levels into the downcomer (see figure 71, group B)

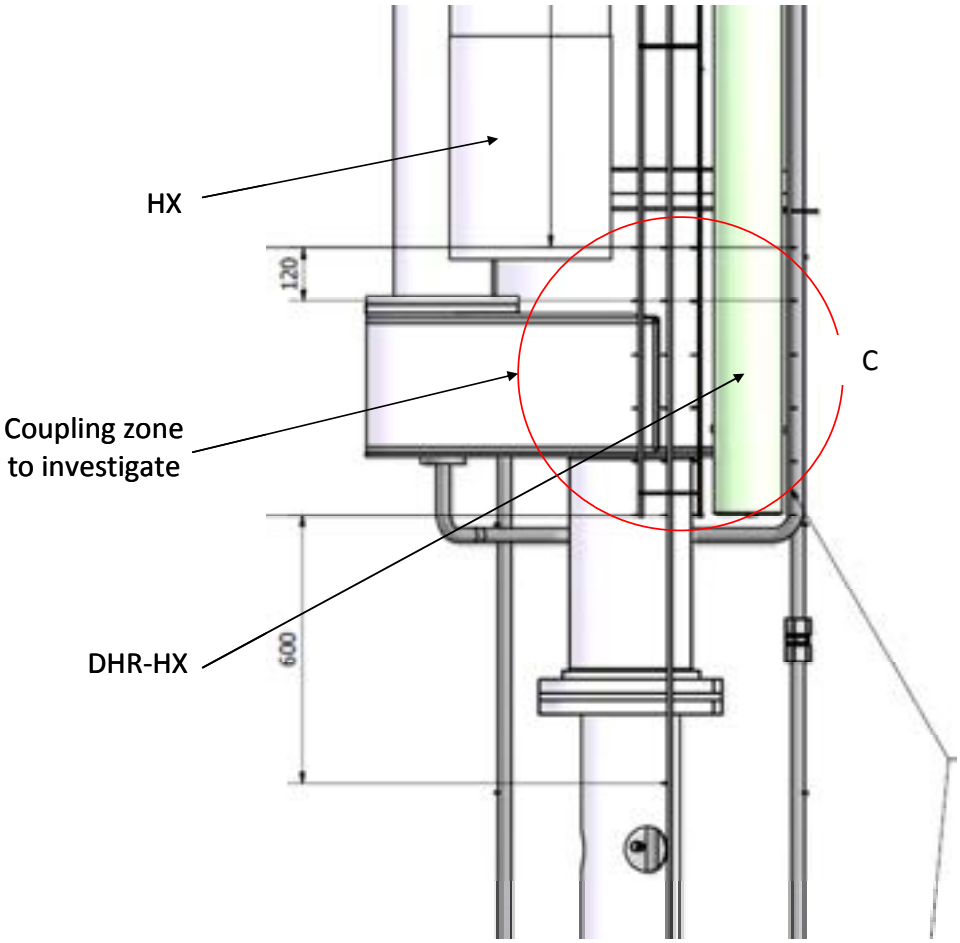

Figure 70. View of the instrumentation foreseen into the downcomer for the monitoring of mixing and thermal stratification. In the red circle the foreseen coupling zone between the HX and DHR-HX

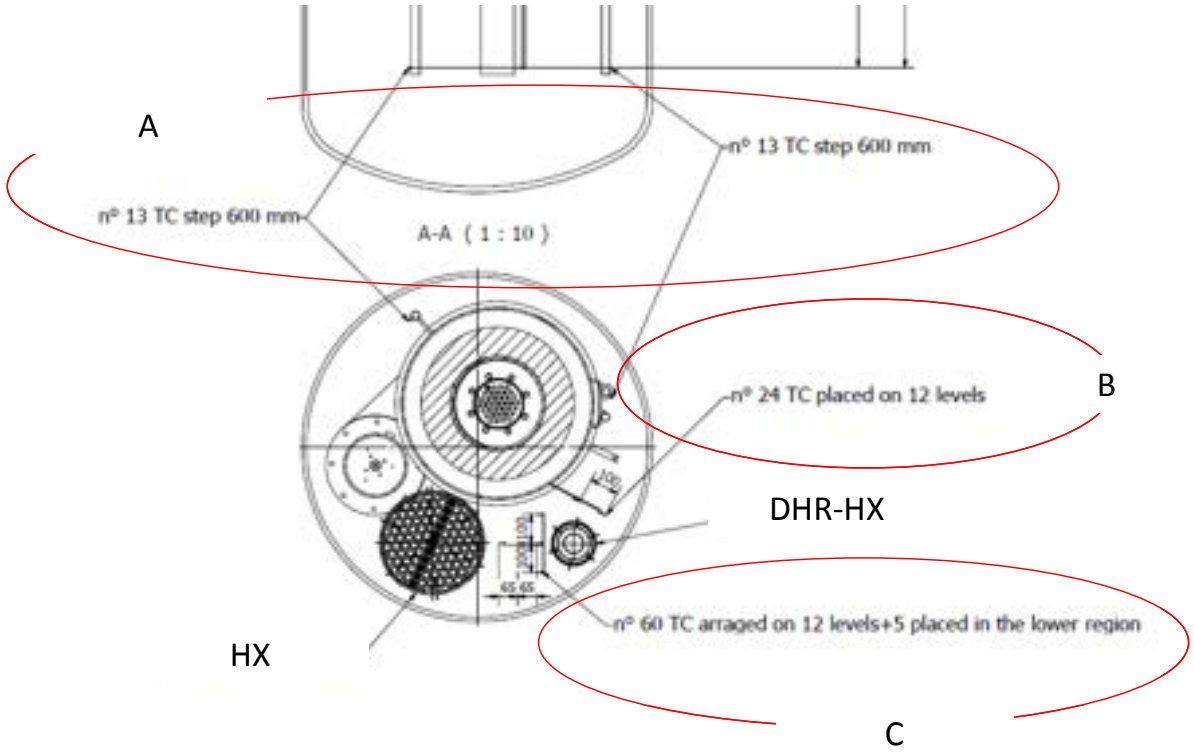

Figure 71. View from the top of the instrumentation foreseen into the downcomer for the monitoring of mixing and thermal stratification. In the red circles the identified groups of thermocouples

Fuel Pin Simulator (FPS): to monitoring the inlet and outlet average temperature of the LBE from the HS the following thermocouples are foreseen:

- 3 TC outlet FPS in the mixing zone (Fitting Volume), see figure 72.
- 3 TC Inlet FPS, at the inlet section of the active zone of the pin bundle (see figures 72, 73).
- 3 TC Outlet FPS, at the outlet section of the active zone of the pin bundle (see figures 72, 73).

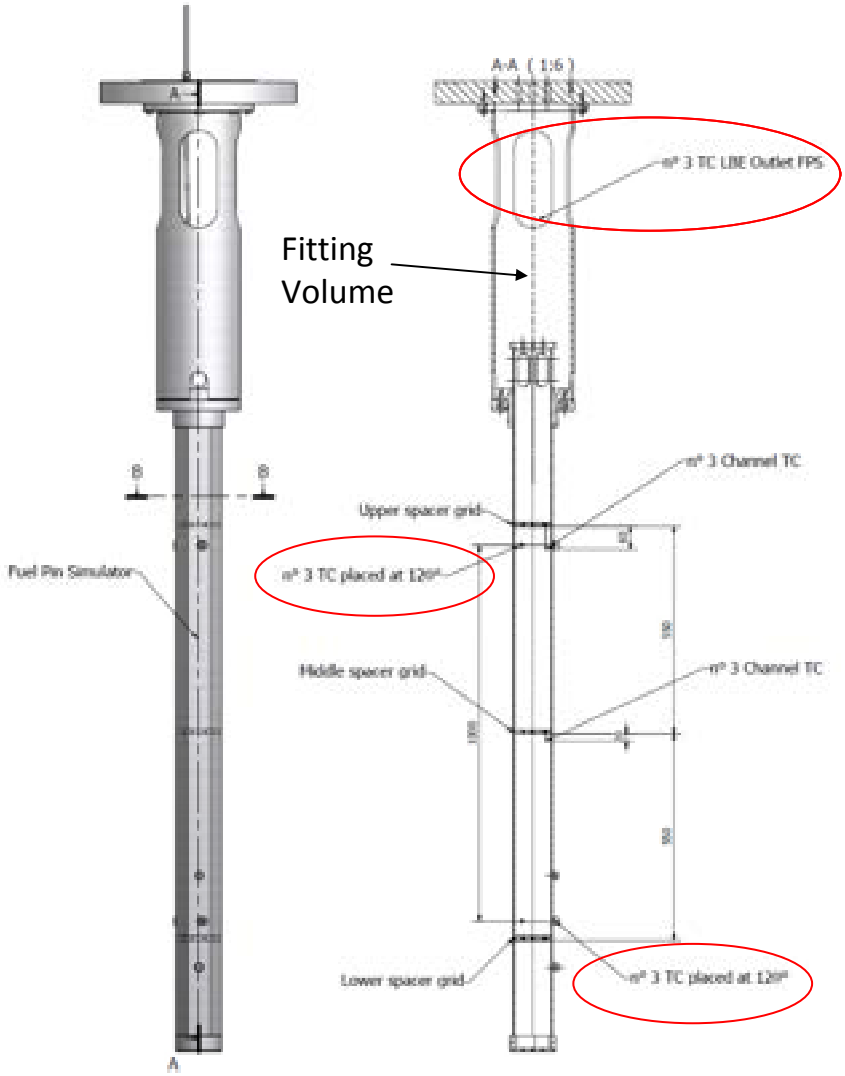

Figure 72. Fuel Pin Simulator overview. In the red circles the TCs adopted for the monitoring of the inlet and outlet temperature of the LBE from the FPS.

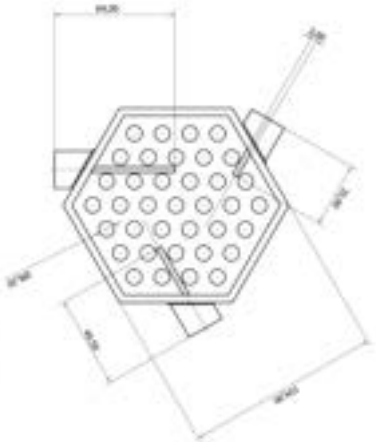

Figure 73. TCs arrangement at the inlet and outlet section of the FPS

5.3 FPS Instrumentation upgrade

As mentioned above, the active zone of the fuel pin simulator will be instrumented by several thermocouples aiming to:

1. measure of the heat transfer coefficient (HTC) in LBE-cooled fuel bundle under forced and natural circulation in a pool system;
2. evaluate the hot spot factor on the fuel bundle due to the installation of a spacer grid;
3. monitoring the pin cladding temperature, which is one of the main parameters to be considered for the safety assessment of nuclear systems, during the steady state condition as well as during the postulated transients.

In figure 74 and figure 75 a view of a fuel bundle cross section and a sketch of the adopted spacer grid respectively.

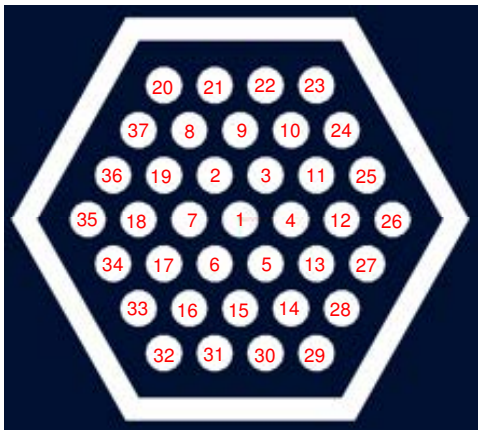

Figure 74. Cross section of the ICE fuel pin bundle

To achieve these goals along the active zone of the fuel pin bundle three different section have been defined.

Section 1: 20 mm upstream the middle spacer grid. In this section three different subchannels have been identified for the HTC measurement at the middle height of the bundle (see figure 76). In each subchannels both pin cladding and LBE bulk temperature are measured by TCs (9) with an OD of 0.5 mm. The distance of 20 mm below the spacer grid will guarantee a HTC measurement unaffected from the

spacer grid itself. The bulk TCs will be driven into the centre of the subchannels by appropriate tubes installed on the spacer grid (see figure 75).

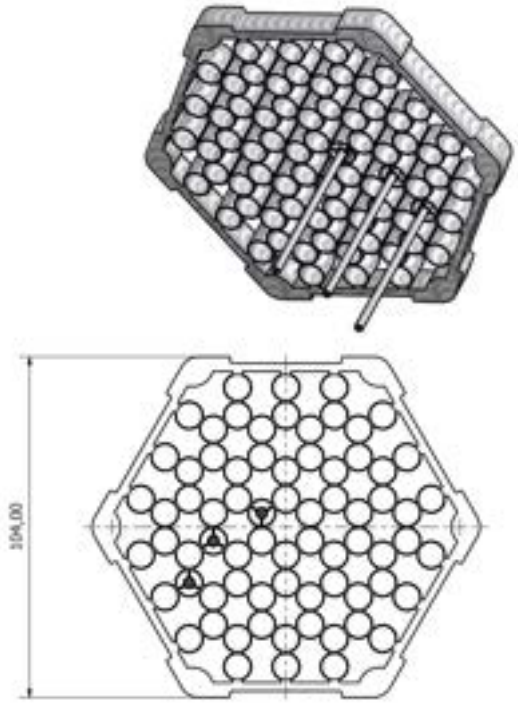

Figure 75. Sketch of the upper spacer grid. Three spacer grids are installed in the ICE fuel bundle, and in the middle and upper ones three small diameter tubes are installed to drive TCs into the subchannels.

Section 2: on the matching surface between the middle spacer grid and the fuel pins. In this section the same subchannels have been identified as in the section 1, aiming for the hot spot factor evaluation due to the installation of the spacer grid itself. In this case only the pin cladding temperature is monitored by TCs (6) with an OD of 0.5 mm (see figure 77).

Section 3: 60 mm upstream the upper spacer grid. In this section the same subchannels have been identified as in the section 1 and 2 for the HTC measurement at the upper height of the bundle (see figure 78). In each subchannels both pin cladding and LBE bulk temperature are measured by TCs (9) with an OD of 0.5 mm. The distance of 60 mm below the spacer grid will guarantee a HTC measurement unaffected from the spacer grid itself. Also in this case the bulk TCs

will be driven into the centre of the subchannels by appropriate tubes installed on the spacer grid (see figure 75).

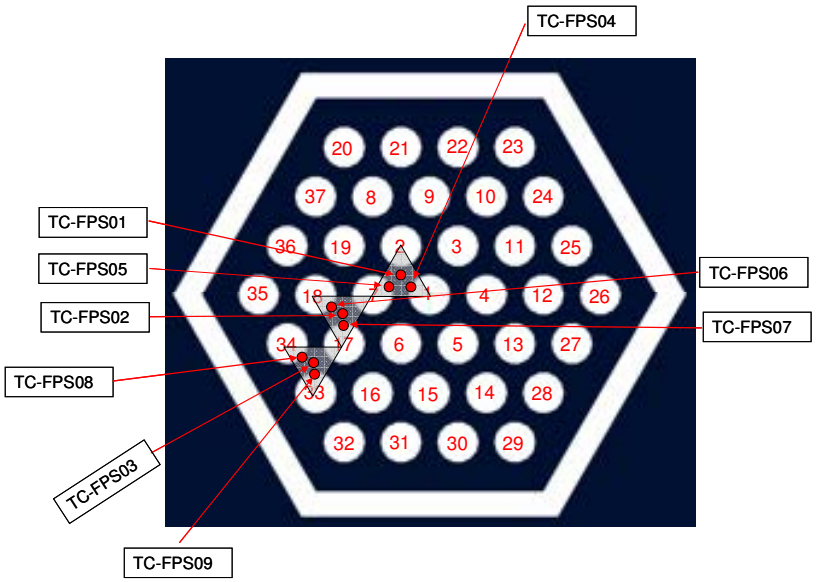

Figure 76. View of the section 1 dedicated to the HTC measurement. In red the TCs installed, 20 mm below the middle spacer grid.

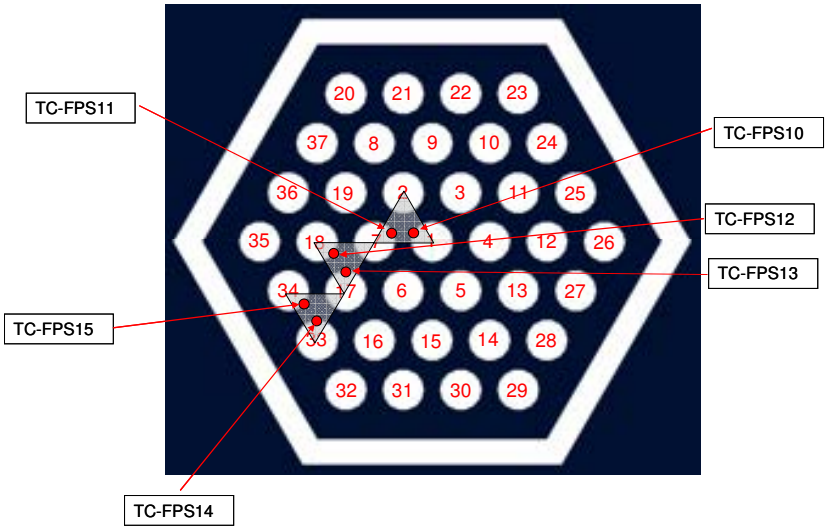

Figure 77. View of the section 2 (on the matching surface between spacer grid and fuel pins) aiming to evaluate the hot spot factor. In red the wall TCs installed.

The hot spot factor will be evaluated considering that the pin cladding temperature has a linear increase along the subchannel, so the “expected temperature” on the matching surface between the cladding and the space grid can

be evaluated by the measurement of the clad temperature on the same pin in the section 1 and 3 respectively.

The ratio between the temperature really measured on the matching surface and the “expected temperature” represent the hot spot factor due to spacer grid installation.

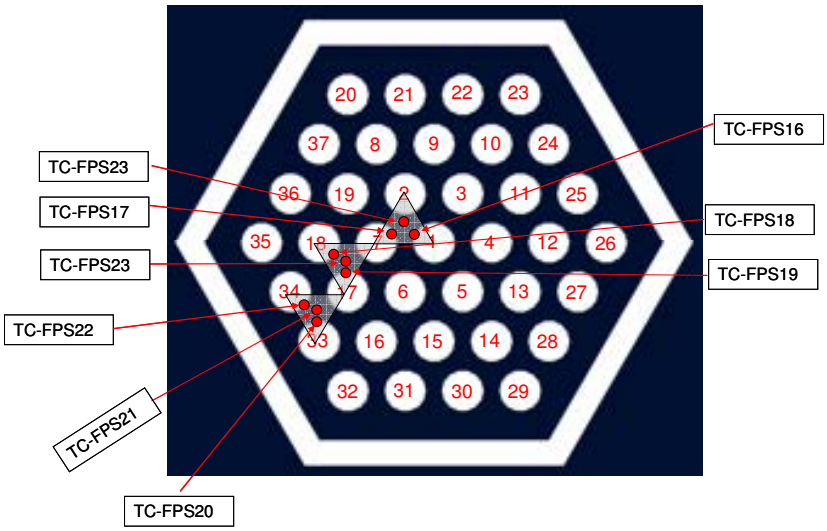

Figure 78. View of the section 3 dedicated to the HTC measurement. In red the TCs installed, 60 mm below the upper grid.

6. REFERENCES

[1] Tarantino M., Scaddozzo G., Report ENEA ET-F-S-001, "*Test specifications of the Integral Circulation Experiments"* Deliverable D. 4.15, DM4 DEMETRA, IP-EUROTRANS, 2006.

[2] Turroni P., Cinotti L. ,Corsini G., Mansani L, "*The CIRCE Facility*", AccApp'01&ADTTA'01, Nuclear Application in the new Millennium, Reno (Nevada- USA), November 11-15, 2001.

[3] Benamati G., Bertacci G., Elmi N., Scaddozzo G., Report ENEA HS-A-R-016, "*Report on Gas Enhanced Circulation Experiments and Final Analysis (TECLA D41)*" 2005.

[4] Barbensi A., Corsini G., *" Specification for the EFIT primary system",* Deliverable D. 1.4, DM1 DESIGN, IP-EUROTRANS, 2006.

[5] Giraud B., "*Review and justification of the main design options of XT-ADS*", Deliverable D. 1.5, DM1 DESIGN, IP-EUROTRANS, 2006.

[6] Artioli C," *Specification for the EFIT Core and Fuel Element Design*", Deliverable D. 1.6, DM1 DESIGN, IP-EUROTRANS, 2006.

[7] Van den Eynde G.," *Specification for the XT-ADS Core and Fuel Element Design*", Deliverable D. 1.7, DM1 DESIGN, IP-EUROTRANS, 2007.

[8] Mansani L.," *Candidates Materials for XT-ADS and EFIT, Operating Conditions and Testing Requirements*", Deliverable D. 4.1, DM4 DEMETRA, IP-EUROTRANS, 2005.

[9] W. Ambrosini, F. Forasassi, N. Forgione, F. Oriolo, M. Tarantino, "*Experimental study on combined natural and gas-injection enhanced circulation*" , Nuclear Engineering and Design, vol. 235, pp. 1179-1188, Iss. 10-12, 2005.

[10] Benamati G., Foletti C., Forgione N., Oriolo F., Scaddozzo G., Tarantino M., "*Experimental study on gas-injection enhanced circulation performed with the CIRCE facility*", Nuclear Engineering and Design, vol. 237, pp. 768-777, Iss. 7, 2007.

[11] Tarantino M., Report ENEA HS-F-R-001 "*Gas Enhanced Circulation Experiments On Heavy Liquid Metal System*", 2007.

[12] FLUENT 6.2 *User's Guide*, January 2005.

[13] G. Grotzbach, "*Turbulence Modelling Issues in ADS Thermal and Hydraulic Analysies"*. IAEA Technical meeting on Theoretical and Experimental Studies of Heavy Liquid Metal Thermal Hydraulics, Karlsruhe, Germany, 2003.

[14] X. Cheng, N.I. Tak, *CFD "Analysis of thermal-hydraulic behaviour of heavy liquid metals in sub-channels"*, Nuclear Engineering and Design 236 (2006), 1874-1885.

[15] X. Cheng, N.I. Tak, "*Investigation on turbulent heat transfer to lead-bismuth eutectic flows in circular tubes for nuclear applications*", Nuclear Engineering and Design 236 (2006), 385-393.

[16] O.E. DWYER, "*Na and NaK Handbook, Liquid-Metal Heat Transfer*", Brookhaven National Laboratory, Upton, New York (1970).

[17] Handbook on Lead-bismuth Eutectic Alloy and Lead Properties, Materials Compatibility, Thermal-hydraulics and Technologies, 2007 Edition, NEA No. 6195

[18] N.E. Todreas, M. S. Kazimi, *Nuclear System I, Thermal Hydraulic Fundamentals*, Taylor&Francis, 1993.

[19] S. Lee, Liquid Metal Heat Transfer in turbulent pipe flow with uniform wall flux, Int. J. Heat Mass Transfer 26(3), 349-356.

[20] H.Graber, M.Rieger, "*Experimentelle Untersuchung des Warmeubergangs an Flussigmetallen in Parallel Durchstromten Rohrbundeln bei Konstanter und Exponentieller Warmeflussdichtverteilung*", Atomkernenergie, Bd. 19, n. 1, S, 23, (1972).

[21] I.E. Idelchick, Handbook of Hydraulic Resistance, 3rd Edition, Begell House.

[22] R. W. Lockart, R. C. Martinelli, "*Proposed correlation of data for isothermal two-phase two-component flow in pipes*", Chem. Eng. Prog. 45:no. 39, 1949.

[23] A. Bejan, A. D. Kraus, "*Heat Transfer Handbook*", John Wiley & Sons, 2003.

[24] ISTC Project No. 3020, "*Development Of Oxygen Sensors, Systems Of Control Of Oxygen Content In Lead Coolants For Test Loops And Facilities"* 2007

[25] Konys J., Musher H., Vob Z., Wedemeyer O., "*Development of Oxygen Meter for the use in Lead-Bismuth*", Journal of Nuclear Material 296 (2001), 289-294

[26] RELAP5/MOD3.2 Code Manual, "NUREG/CR-5535-Vol.I-VII", June 1995

[27] Bianchi F., Meloni P., Mattioda F., Forasassi G., Fruttuoso G., Oriolo F., Bocci S., "*Implementation and preliminary verification of the RELAP5/PARCS code for Pb-Bi cooled subcritical systems*", AccApp'01 & ADTTA'01, Nuclear Application in the new Millennium, RENO (Nevada-USA), November 11-15, 2001.

[28] Pfrang W., Struwe D., "*Assessment of Correlations for the Heat Transfer to the Coolant for Heavy Liquid Metal Cooled Core Designs*" Forschungsentrum Karlsruhe, FZKA 7352, October 2007.

[29] Group of Experts of the NEA Committee on the Safety of Nuclear Installations, *Validation Matrix for the Assessment of Thermal-Hydraulic Codes for VVER LOCA and Transients*, NEA/CSNI/R(2001)4, June 2001.

[30] G. Bandini, P. Meloni, M. Polidori, P. Gaggini, V. Labanti, M. Tarantino, L. Cinotti, L. Presciuttini, "Analysis and Testing of W-DHR System for Decay Heat Removal in the Lead-Cooled ELSY Reactor", Proceedings of ICAPP'09 Conference, Tokyo, Japan, May 10-14, 2009.

[31] C.D. Fletcher, R.R. Scuhltz, "RELAP5/MOD3 Code manual", NUREG/CR–5535, INEL–95/174, Idaho National Engineering Laboratory, June 1995.

[32] P. Agostini, et al., "Natural Circulation of Lead-Bismuth in a One-Dimensional Loop: Experiments and Code Predictions", Proceedings of the 10th International Conference on Nuclear Engineering (ICONE-10), Arlington, Virginia, USA, April 14-18, 2002.

[33] P. Meloni, A.D. Wagner, F: Castiglia, M. Casamirra, P. Agostini, G. Bertacci, "Investigation of RELAP Capability to Simulate the LBE Cooling System Thermal-Hydraulic", 8th Information Exchange Meeting on Actinide and Fission Product Partitioning & Transmutation, Las Vegas, Nevada, USA, November 9-11, 2004.